Viewpoint: Atomic-Scale Design Protocols toward Energy, Electronic, Catalysis, and Sensing Applications

DOI:
10.1021/acs.inorgchem.9b01785

Document Version
Accepted author manuscript

Published in:
Inorganic Chemistry

Viewpoint: Atomic-scale design protocols towards energy, electronic, catalysis and sensing applications

Journal:	*Inorganic Chemistry*
Manuscript ID	ic-2019-01785j.R1
Manuscript Type:	Viewpoint
Date Submitted by the Author:	n/a
Complete List of Authors:	Belviso, Florian; Ceske Vysoke Uceni Technicke Fakulta elektrotechnicka, Department of Control Engineering Claerbout, Victor; Ceske Vysoke Uceni Technicke Fakulta elektrotechnicka, Department of Control Engineering Comas-Vives, Aleix; Autonomous University of Barcelona, Chemistry Dalal, Naresh; Florida State University, Chemistry and Biochemistry Fan, F.; Fudan University, Department of Physics; Fudan University State Key Laboratory of Surface Physics Filippetti, Alessio; Universita degli Studi di Cagliari Fiorentini, Vincenzo; Universita degli Studi di Cagliari Foppa, Lucas; Eidgenossische Technische Hochschule Zurich, Department of Chemistry and Applied Biosciences Franchini, Cesare; Universitat Wien, Computergestützte Materialphysik Geisler, Benjamin; Universitat Duisburg-Essen Ghiringhelli, Luca; Fritz Haber Institut der Max-Planck-Gesellschaft Groβ, Axel; Universitat Ulm, Institute of Theoretical Chemistry Hu, Shunbo; Shanghai University, Department of Physics Íñiguez, Jorge; Luxembourg Institute of Science and Technology; University of Luxembourg Kauwe, Steven; University of Utah, Materials Science and Engineering Musfeldt, J.; University of Tennessee Nicolini, Paolo; Ceske Vysoke Uceni Technicke Fakulta elektrotechnicka, Department of Control Engineering - K335 Pentcheva, Rossitza; Ludwig-Maximilians-Universitat Munchen, Department of Physics Polcar, Tomas; Ceske Vysoke Uceni Technicke Fakulta elektrotechnicka, Department of Control Engineering Ren, Wei; Department of Physics, Ricci, Fabio; Université de Liège Ricci, Francesco; Université catholique de Louvain, IMCN - NAPS Sen, Huseyin; Ceske Vysoke Uceni Technicke Fakulta elektrotechnicka, Department of Control Engineering Skelton, Jonathan; University of Bath Sparks, Taylor; University of Utah Stroppa, Alessandro; CNR-SPIN Urru, Andrea; Universita degli Studi di Cagliari Vandichel, Matthias; Aalto University, Department of Chemistry and Material Science Vavassori, Paolo; CIC nanoGune Consolider, Wu, Hua; Fudan University, Department of Physics Yang, Ke; Fudan University, Department of Physics Zhao, Hong Jian; Luxembourg Institute of Science and Technology,

	Materials Research and Technology Puggioni, Danilo; Northwestern University, Cortese, Remedios; Universita degli Studi di Palermo, Dipartimento di Chimica Cammarata, Antonio; Ceske Vysoke Uceni Technicke Fakulta elektrotechnicka, Department of Control Engineering

Viewpoint: Atomic-scale design protocols towards energy, electronic, catalysis and sensing applications

Florian Belviso,[†] Victor E. P. Claerbout,[†] Aleix Comas-Vives,[‡] N. Dalal,[¶,§] F. Fan,[‖] Alessio Filippetti,[⊥] Vincenzo Fiorentini,[⊥] Lucas Foppa,[#] Cesare Franchini,[@,△] Benjamin Geisler,[▽] Luca M. Ghiringhelli,[††] Axel Groß,[‡‡,¶¶] Shunbo Hu,[§§] Jorge Íñiguez,[‖‖] Steven K. Kauwe,[⊥⊥] J. Musfeldt,[##] Paolo Nicolini,[†] Rossitza Pentcheva,[▽] Tomas Polcar,[@@] W. Ren,[§§] F. Ricci,[△△] Huseyin Sener Sen,[@@] Jonathan M. Skelton,[▽▽▽,†††] Taylor D. Sparks,[⊥⊥] Alessandro Stroppa,[‡‡‡] Andrea Urru,[⊥] Matthias Vandichel,[¶¶¶,§§§] P. Vavassori,[‖‖‖] H. Wu,[‖,⊥⊥⊥] K. Yang,[‖] Hong Jian Zhao,[‖‖] Danilo Puggioni,[*,###] Remedios Cortese,[*,@@@] and Antonio Cammarata[*,†]

[†]*Department of Control Engineering, Czech Technical University in Prague, Technicka 2, 16627 Prague 6, Czech Republic*

[‡]*Department of Chemistry, Universitat Autónoma de Barcelona, 08193 Cerdanyola del Vallès, Catalonia, Spain*

[¶]*Nat. High Magnet Field Lab, Tallahassee, FL 32310 USA*

[§]*Florida State University, Dept. of Chemistry & Biochemistry, Tallahassee, FL 32306 USA*

[‖]*Laboratory for Computational Physical Sciences (MOE), State Key Laboratory of Surface Physics, and Department of Physics, Fudan University, Shanghai 200433, China*

[⊥]*Department of Physics at University of Cagliari, and CNR-IOM, UOS Cagliari, Cittadella Universitaria, I-09042 Monserrato (CA), Italy*

[#]*Department of Chemistry and Applied Biosciences, ETH Zürich, Vladimir-Prelog-Weg 1-5, CH-8093 Zürich, Switzerland.*

[@]*University of Vienna, Faculty of Physics and Center for Computational Materials Science, Sensengasse 8, A-1090 Vienna, Austria*

[△]*Dipartimento di Fisica e Astronomia, Universitá di Bologna, 40127 Bologna, Italy*

[▽]*Department of Physics and Center for Nanointegration (CENIDE), Universität Duisburg-Essen, Lotharstr. 1, 47057 Duisburg, Germany*

[††]*Fritz-Haber-Institut der Max-Planck-Gesellschaft, 14195 Berlin-Dahlem, Germany*

[‡‡]*Helmholtz Institut Ulm (HIU) Electrochemical Energy Storage, 89069, Ulm, Germany*

[¶¶]*Institute of Theoretical Chemistry, Ulm University, 89069, Ulm, Germany*

[§§]*Department of Physics, and International Center of Quantum and Molecular Structures, Shanghai University, Shanghai 200444, China*

[‖‖]*Materials Research and Technology Department, Luxembourg Institute of Science and Technology (LIST), Avenue des Hauts-Fourneaux 5, L-4362 Esch/Alzette, Luxembourg, and Physics and Materials Research Unit, University of Luxembourg, Rue du Brill 41, L-4422 Belvaux, Luxembourg*

[⊥⊥]*Materials Science & Engineering Department, University of Utah, 122 Central Campus Dr., Salt Lake City, UT, 84112, USA*

[##]*Department of Chemistry, University of Tennessee, Knoxville, TN 37996 USA*

[@@]*Department of Control Engineering, Czech Technical University in Prague, Technicka 2, 16627 Prague 6, Czech Republic*

[△△]*Physique Théorique des Matériaux, Université de Liège, B-4000 Sart-Tilman, Belgium*

[▽▽▽]*School of Chemistry, University of Manchester, Oxford Road, Manchester M13 9PL, United Kingdom*

[†††]*Department of Chemistry, University of Bath, Claverton Down, Bath BA2 7AY, United Kingdom*

[‡‡‡]*CNR-SPIN, c/o Dip.to di Scienze Fisiche e Chimiche - Via Vetoio - 67010 - Coppito (AQ), Italy*

[¶¶¶]*Department of Chemical Sciences and Bernal institute, Limerick University, Limerick, Ireland*

[§§§]*Department of chemistry and material science (School of Chemical Engineering) and Department of Applied Physics (School of Science), Aalto University, 02150 Espoo, Finland*

[‖‖‖]*CIC nanoGUNE, Donostia-San Sebastian, E-20018 and IKERBASQUE, Basque Foundation for Science, Bilbao, 48013, Spain*

[⊥⊥⊥]*Collaborative Innovation Center of Advanced Microstructures, Nanjing 210093, China*

[###]*Department of Materials Science and Engineering, Northwestern University, 2220 Campus Drive, 60208, Evanston, Illinois, USA*

[@@@]*Department of Physics and Chemistry, Universitá degli Studi di Palermo, Viale delle Scienze ed. 17, 90128, Palermo, Italy*

E-mail: danilo.puggioni@northwestern.edu; remedios.cortese@unipa.it; cammaant@fel.cvut.cz

Abstract

Nanostructured materials are essential building blocks for the fabrication of new devices for energy harvesting/storage, sensing, catalysis, magnetic and optoelectronic applications. However, due to the increase of technological needs, it is essential to identify new functional materials and improve the properties of existing ones. The objective of this viewpoint is to examine the state of the art of atomic-scale simulative and experimental protocols aimed to the design of novel functional nanostructured materials, and to present new perspectives in the relative fields. This is the result of the debates of Symposium I "Atomic-scale design protocols towards energy, electronic, catalysis and sensing applications", which took place within the 2018 European Materials Research Society fall meeting.

Contents

1 Introduction

The modern technology has a huge impact on our everyday life. For example, nowadays a vast number of tasks can be performed with a couple of clicks. Functional materials, i.e. materials exhibiting adaptive capabilities to external stimuli,[1] form the basis for a wide range of technologies. Their societal impact is tantamount in energy harvesting/storage, sensing, catalysis, magnetic and optoelectronic applications.

During the last years, intensive research activities have been devoted to the synthesis and characterization of nanomaterials. The discovery of novel materials with desirable properties, however, requires that we understand the atomic structural principles governing the functional response. In this perspective, the Symposium I "Atomic-scale design protocols towards energy, electronic, catalysis and sensing applications", which took place within the 2018 European Materials Research Society fall meeting, focused on the recent developments of design strategies for smart materials. Here, the outcomes of the Symposium's debates are reported.

This viewpoint first focuses on general technical aspects of performing first-principles calculations, on creating integrated data infrastructures and extracting useful information from them, and on issues related to machine learning techniques. Materials and processes for energy conversion through catalysis and hazards in energy storage in batteries are then

addressed. A broad range of functional materials are covered in the remaining sections of this viewpoint, from molecular solids and metallic multilayer composites, oxide thermoelectrics and "ferroelectric" metals, to hybrid organic-inorganic perovskites and triboelectric materials. These examples illustrate the challenges in understanding and improving functional materials, but they also demonstrate the progress that has been made on an atomistic level by advanced techniques, both in theoretical and experimental studies. Particular emphasis has been put on synergistic investigations involving experimentals, materials informatics, and computational approaches, which can provide the fundamental understanding of these materials as well as new insights necessary to guide and accelerate the search of materials with targeted functionalities.

2 Predicting the band gap of complex materials: computational methods and procedures

The prediction and interpretation of materials properties requires the combination of advanced theoretical models and accurate numerical schemes. For decades, density functional theory (DFT)[2,3] has been the primary method to estimate the ground-state properties of materials, and still represents a common methodological scheme for studying a wide variety of physical phenomena, including those reviewed in the present viewpoint. Despite its great success, DFT has some limitations arising from the approximation used to construct the exchange and correlation functionals that hinders its performance. An archetypal shortcoming of DFT is the calculation of the band gap, a property of fundamental importance and crucial for all practical applications, including energy, electronic, catalysis and sensing applications, which are the main focus of this work and will be elaborated and discussed more extensively in the following sections. A variety of quantum-mechanical methods has been proposed to cure this problem, including local corrections inspired by the Hubbard-based models[4] (e.g. DFT+U and self-interaction corrected schemes), hybrid functionals (for exam-

ple see 5–7), quasiparticle approaches[8] (GW) and, for what concern the optical excitations, the Bethe-Salpeter equation.[9]

2.1 scPBE0 hybrid functional

A promising compromise between the computational cost and the accuracy of the calculated band gap value is represented by hybrid functionals. Figure 1 shows a selection of hybrid functional band gaps computed for a wide set of insulating and semiconducting materials.[10] Despite the research effort made so far, further investigation is still needed to improve the prediction of the band gap value, which mainly relies on mixing parameters at the basis of the hybrid energy functional formulation. As an example, the procedure to carry one scPBE0[10] calculation is here concisely described, which is one of the last members of the hybrid family.

The scPBE0 hybrid energy functional is based on the self-consistent evaluation of the mixing parameter α, which controls the amount of HF exchange.[10] This is done by means of an iterative calculation of the static dielectric constant using the perturbation expansion after discretization (PEAD) method.[11] Specifically, one starts the self-consistent loop by using the standard mixing α_{in}=0.25. At the end of this iteration the output mixing α_{out} is determined as the inverse of the mean value of the diagonal elements of the dielectric function evaluated by PEAD, i.e., $\alpha_{\text{out}} = 1/\overline{\varepsilon_\infty}$, where ε_∞ is the ion-clamped static dielectric tensor. This new value of α is then used to start a new iteration. The self consistent procedure stops when $\alpha_{\text{out}} - \alpha_{\text{in}}$ is smaller than the desired accuracy (usually $\sim 10^{-2}$).

The results obtained by fixed-α (PBE0 and HSE03) and self-consistent (scPBE0) hybrids (Figure 1) show that scPBE0 performs better for band gaps smaller than $\approx$ 8 eV, whereas for larger gaps PBE0 appears to be a better choice. The non-empirical extension of range-separated hybrids, in which not only the mixing parameters α but also the screening length (typically labeled μ in HSE-like hybrids), represents a possible route for improvement. Following this idea, a new class of non-empirical hybrid functionals based on a model

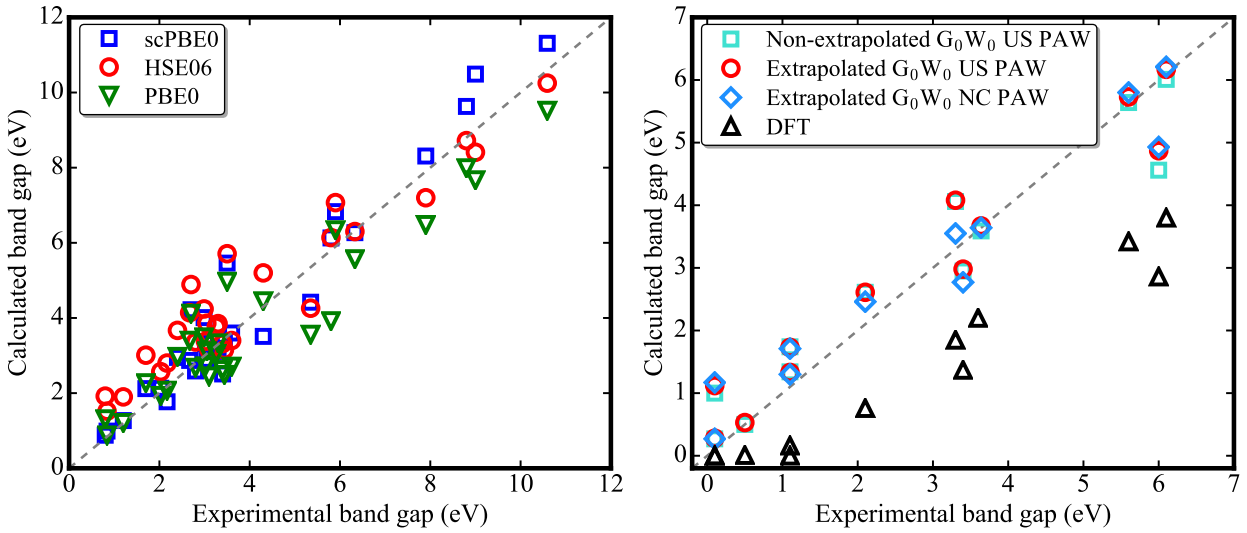

Figure 1: Comparison between calculated and experiment band gaps. (a) hybrid functionals for a dataset including 30 semiconductors and (b) GW applied to a perovskite dataset including $3d$, $4d$, and $5d$ transition metals. Adapted from Refs. 10 and 12.

dielectric function has been recently proposed that indeed predicts accurately band gaps for both narrow- and wide-gap semiconductor.[13] The next level of theory which allows the computation of quasiparticle energies and guarantees an improved prediction of band gaps is the GW method.[8]

2.2 GW method

The GW method is probably the most accurate approach presently available for condensed matter physics calculations. Alternative advanced methodologies have been developed in other sectors, for example quantum chemistry methods, such as Møller-Plesset perturbation and coupled cluster theories,[14] which are however still computationally too demanding when applied to complex extended systems. The essence of the GW scheme is the inclusion of the self energy, defined as $\Sigma = iGW$ (where G is the single particle Green's function and W is the screened Coulomb interaction), in the generalized Kohn-Sham equations. Regrettably enough, despite its success, the proper use of the GW method is not well established from a technical point of view, yielding to non converged solutions. In fact, the convergence criteria

requires a summation over many empty states (N) and a sufficiently dense k-points mesh resulting in large computational cost and memory requirements. However, two different routes can be followed to obtained converged results:[12]

1. *Basis-set extrapolation.* The core aspect of this scheme is to extrapolate the quasi-particle (QP) energies obtained using a finite-basis-set to the infinite-basis-set limit through the formula:

$$E_\infty(N_k, N_\infty) \approx \underbrace{E_\infty(n_k, N_\infty)}_{\Delta_N(n_k)} \overbrace{- E(n_k, N)}^{\Delta_k(N)} + E(N_k, N), \quad (1)$$

   where $E(N_k, N)$ is the calculated QP energies with N_k **k**-points and N bands, $E(N_k, N_\infty)$ is the corresponding extrapolated ($N \to \infty$) QP energies, and the variables n_k and N_k indicate the number of **k**-points in the small and large **k**-point mesh, respectively.

2. *Conventional scheme.* This method attempts to converge the QP energies with respect to a set of three parameters: number of bands, energy cutoff for the plane wave expansion for the orbitals E_{pw} and the number of **k**-points.

An important aspect to consider when performing GW calculations is the choice of the pseudopotential. Even though accurate results can be also obtained with ultrasoft pseudopotentials, it is recommended, when possible, to adopt norm conserving pseudopotentials. Following the above consideration one can achieve remarkably good fundamental band gap for a wide set of transition metal perovskites, as shown in Figure 1.

An additional ambiguity, which is often source of confusion, is the difference between fundamental electronic gap, that is the energy difference between the lowest unoccupied state and the highest occupied one, and the optical gap, which includes electron-hole interaction and is lower than the fundamental electronic gap by an amount which is typically referred to as excitonic energy.[15] Excitonic effects, not included in the GW scheme, can be accounted for by using the Bethe-Salpeter equation (BSE), in which the response function is computed

from the Dyson-like equation.[16]

2.3 BSE calculations

The procedure to conduct BSE calculations consists of four steps:[17]

1. Standard self-consistent DFT calculations. If the DFT ground state turns out to be metallic it is necessary to add a small U or a scissor operator (only in this step),

2. Additional DFT step to compute the one-electron wave functions and eigenenergies of all virtual orbitals evaluated by an exact diagonalization,

3. G_0W_0 runs to compute the QP energies and static screened interaction W, and

4. BSE run (typically in the Tamm-Dancoff approximation[18]) to compute the frequency-dependent macroscopic dielectric function

$$\varepsilon(\omega) = 1 - \lim_{\mathbf{q}\to 0} V(\mathbf{q}) \sum_{\Lambda} \left(\frac{1}{\omega - \Omega_\Lambda + \mathrm{i}\eta} - \frac{1}{\omega + \Omega_\Lambda - \mathrm{i}\eta} \right) \times \left\{ \sum_{\mathbf{k}} w_{\mathbf{k}} \sum_{v,c} \langle \psi_{c\mathbf{k}} | e^{\mathbf{i}\mathbf{q}\cdot\mathbf{r}} | \psi_{v\mathbf{k}} \rangle X^{\Lambda}_{cv\mathbf{k}} \right\} \times \Big\{ c.c. \Big\}, \tag{2}$$

   with the oscillator strengths S_Λ associated with the optical transitions defined by

$$S_\Lambda = \mathbf{Tr} \left[\left\{ \sum_{\mathbf{k}} w_{\mathbf{k}} \sum_{v,c} \langle \psi_{c\mathbf{k}} | e^{\mathbf{i}\mathbf{q}\cdot\mathbf{r}} | \psi_{v\mathbf{k}} \rangle X^{\Lambda}_{cv\mathbf{k}} \right\} \times \Big\{ c.c. \Big\} \right]. \tag{3}$$

   In the last two equations, Ω_Λ and X^Λ are BSE eigenvalues and eigenvectors, respectively, V is the bare interaction, η is a positive infinitesimal, $w_{\mathbf{k}}$ are the k-point weights while $\psi_{v\mathbf{k}}$ and $\psi_{c\mathbf{k}}$ refer to occupied and unoccupied DFT($+U$) wave functions, respectively.

Using these prescriptions, excellent optical properties are obtained for the challenging spin-orbit coupled Dirac-Mott properties of Sr_2IrO_4 and $Sr_3Ir_2O_7$,[17] as shown in Figure 2.

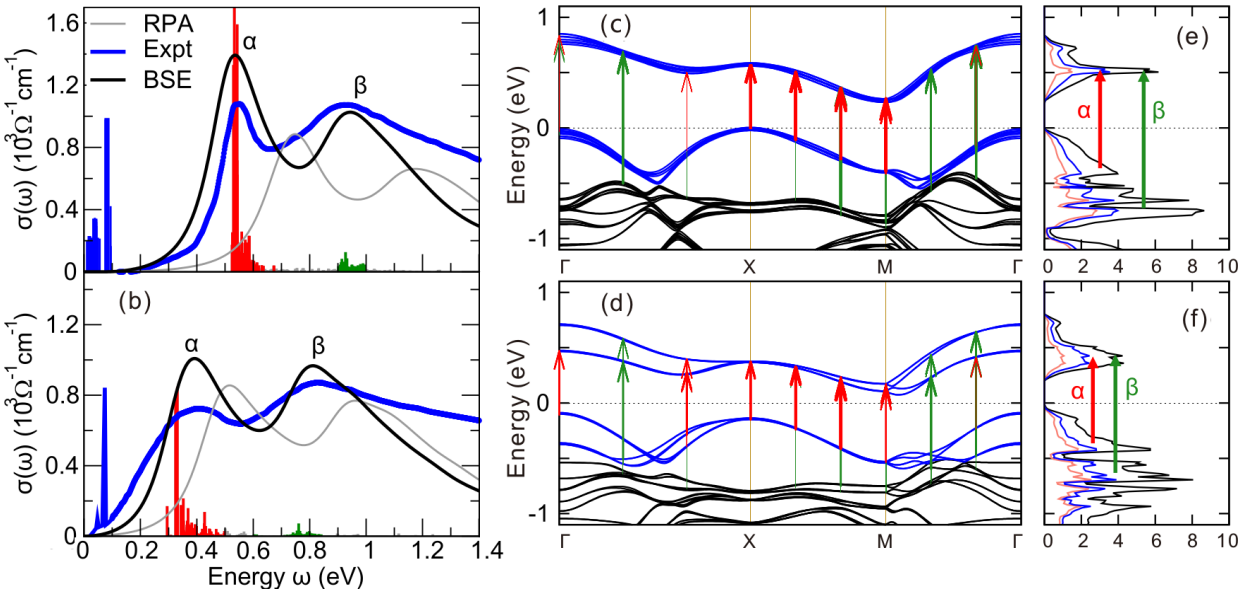

Figure 2: Experimental and calculated optical conductivity spectra $\sigma(\omega)$ of (a) Sr_2IrO_4, (b) $Sr_3Ir_2O_7$. The gray vertical lines represent the oscillator strength whose contributions to α and β peaks are highlighted in red and blue colors, respectively. (c,d) *GW* band structure. (e, f) *GW* total density of states. The red and blue arrows in (c, d) represent the dominant interband transitions for the α and β peaks, respectively. The width of the arrows denotes the normalized amplitude of BSE eigenvectors $|X^{\Lambda}_{cv\mathbf{k}}|$. Adapted from Ref.[17]

Note that, step 3 is rather expensive and do not scale favorably with the number of k points. Considering that the calculation of BSE spectra requires many k points to reach a good level of convergence, it can be useful to adopt an analytical treatment of the screening as input in the BSE run (step 4):

$$\varepsilon^{-1}_{\mathbf{G},\mathbf{G}}(\mathbf{q}) = \varepsilon^{-1}_{\infty} + (1-\varepsilon^{-1}_{\infty})[1-\exp(-\frac{|\mathbf{q}+\mathbf{G}|^2}{4\lambda^2})], \quad (4)$$

where ε_{∞} is the static ion-clamped dielectric function in the long-wave limit and the screening length parameter λ is derived by fitting the screening ε^{-1} at small wave vectors with respect to $|\mathbf{q}+\mathbf{G}|$ with $\mathbf{q}$ and $\mathbf{G}$ being the wave vector and lattice vector of the reciprocal cell, respectively.[17]

2.4 Outlook

In conclusions, a set of state-of-the-art first principles schemes have been briefly scrutinized; these are capable to deliver a good estimation of band gaps, not only for standard semiconductors but also for complex oxides with different electronic configurations, magnetic orderings, structural characteristics and spin-orbit coupling strength. These methods, in particular GW and BSE, are computationally very demanding and much care must be taken in setting up the computational protocol. As future challenges, it would be desirable and useful (*i*) to find common standards for the automation of these complex sequences of simulations (streamline workflows), (*ii*) to build an high-quality beyond-DFT materials database ("Quantum Materials Repository") and, possibly, (*iii*) to envision smart ways to accelerate the calculations without loss of accuracy (machine learning techniques). This would facilitate a paradigmatic shift in the materials modeling community from massively DFT-based calculations to beyond-DFT schemes, which would be beneficial for the quality and accuracy of the results and therefore for the prediction and understanding of material-specific functionalities.

3 Data-driven materials science: building maps of materials properties

3.1 Descriptors in materials science

High-performance computing (HPC) is used for the search and design of novel functional materials with improved functionalities. According to the Springer Materials database,[19] about 250,000 inorganic materials, including stable and metastable phases, are known to exist to date. Unfortunately, even somewhat basic properties — such as elastic constants, electrical and thermal conductivity, and similar — are systematically known only for very few of them. Computational high-throughput initiatives like Materials Project,[20] AFLOW,[21]

and OQMD[22] have collected information on hundreds of thousands of possible materials and made them available in open-access databases. However, while electronic structure calculations provide a wealth of information, the majority of these data are not efficiently used.

Recently, a manifesto[23] on how scientific data should be handled has been proposed: It goes under the acronym FAIR, which stands for findable, accessible, interoperable, and reusable/repurposable. The recently established NOMAD (Novel Materials Discovery) Laboratory[24,25] already complies to the FAIR principles. This is made possible by the NOMAD Repository & Archive, as of end of 2018 containing more than 50000000 open-access single-point calculations of millions of different chemical compositions and atomic structures, mainly bulk materials. These include also calculations from the above mentioned databases, and more. For all the calculations, original input and output files are stored in the Repository and a code-independent representation of all calculations' data is accessible in the Archive, thanks to a remapping of the raw data into a hierarchical metadata framework.[24]

It is easy to realize that the number of possible stable and metastable materials is to all practical purposes infinite. This suggests that novel functional materials with superior properties for any conceivable application, should exist, but are not yet known. High-throughput scanning of the compositional and structural materials space may not be an efficient approach when used with accurate electronic-structure methods, because the latter are computationally demanding in terms of CPU/GPU hours.

A promising alternative approach is to construct models almost as accurate as reliable electronic-structure methods, but running at a fraction of the cost by means of learning algorithms. This is the realm of artificial intelligence or (big-)data analytics that is data mining, machine/statistical learning, deep learning, compressed sensing, and others. In the past ten years, more and more such approaches have been developed and applied to the wealth of materials-science data.[26–37] The first blind-test, crowd-sourced competition for the machine learning of properties from materials-science data — the NOMAD 2018

Kaggle competition[38] — has been a recent turning point towards widespread acceptance of good-practice protocols in data-driven materials science. Besides, it confirmed (Gaussian) kernel methods or, alternatively, the similar Gaussian-process regression, artificial neural networks, and tree-regression methods as the most popular and versatile artificial-intelligence approaches.[38]

In all the cited works, the crucial step is the identification of *descriptors* which capture the underlying mechanism of a given materials property or function and are the numerical input for the machine-learning model. The descriptors are carefully designed by the researcher, by imposing known physical symmetries and constraints. Alternatively, the descriptors can be learned from the data, more precisely the best descriptors can be identified among a possibly immense set of candidates by exploiting a signal-analysis technique known as compressed sensing (CS).[39]

3.2 Compressed sensing

The compressed sensing (CS) approach reconstructs a high quality "signal", starting from a sparse set of "observations".[40,41] Mathematically, given a set of samples measured incoherently ($\boldsymbol{P}$) CS finds the sparse solution ($\boldsymbol{c}$) of an undetermined system of linear equations $\boldsymbol{D}\boldsymbol{c} = \boldsymbol{P}$, where $\boldsymbol{D}$ is the *sensing matrix* with the number of columns much larger than the number of rows. The recasting of CS into materials-science challenges[39,42] starts from a set of materials (m_i) with observable properties listed in vector $\boldsymbol{P}_i$ and a possibly immense list of test features, d_j, which form the features space. The projection of each i-material into the j-feature is the i,j component of the sensing matrix $\boldsymbol{D}$. The sparse solution of $\arg\min_{\boldsymbol{c}} (\|\boldsymbol{P} - \boldsymbol{D}\boldsymbol{c}\|_2^2 + \lambda\|\boldsymbol{c}\|_0)$, where $\|\boldsymbol{c}\|_0$ is the improper norm of $\boldsymbol{c}$ (i.e., its number of nonzero components), gives the optimum ΩD-dimensional descriptor, i.e., the set of features "singled out" by the ΩD non-zero components of the solution vector $\boldsymbol{c}$. The first term in the minimized expression is a familiar mean square error, as in least-square regression; the second term is known as regularization. In this case, a "penalty" is payed for every

non zero component of $\boldsymbol{c}$. Effectively, CS performs a *dimensionality reduction* from the large input features space to the selected low-dimensional descriptor. Differently from most dimensionality-reduction schemes,[43] CS provides an "inspectable" solution, in the sense that the components of the selected descriptor are among the input features.

The sure independence screening and sparsifying operator (SISSO)[44] is a recently developed CS-based method, designed for identifying low-dimensional descriptors for material properties. It is an iterative scheme that combines the sure independence screening scheme (SIS)[45] for dimensionality reduction of huge features space and the sparsifying operators (SO) for finding sparse solutions. SISSO improves the results over the conventional CS methods, such as the Linear Absolute Shrinkage and Selection Operator (LASSO)[39,42,46] and greedy algorithms,[47,48] when features are correlated, and can efficiently manage immense features spaces.

For applying SISSO, a feature space Φ_q is constructed by starting from a set of primary features and a set of unary and binary operators, such as $+, -, \exp, \sqrt{}$, etc. The features are then iteratively combined with the operators, where at each iteration each feature, or pair of features, is exhaustively combined with each unary/binary operator, with the constraint that sums and differences are taken only among homogeneous quantities. The index q in Φ_q counts how many such iterations were performed. The primary features are typically *atomic properties* (e.g., ionization potential, radius of s or p valence orbital, etc.) and *compounds properties* (e.g., formation energy of dimers, volume of the unit cell in a given crystal structure, average coordination, ...).[44] Φ_q contains features in terms of mathematical expressions; when the values of the features are determined for each material m_i, the matrix $\boldsymbol{D}$ is constructed. The *atomic properties* are repurposable and therefore can be used for many descriptor and model learning. For easier reference and reusability, the atomic features used in this work and other related works[39,42,44,49] can be accessed on line at the *NOMAD Analytics Toolkit*: `https://analytics-toolkit.nomad-coe.eu`.[50] A tutorial[51] shows how to access these quantities and use them in a python notebook.

Next, the sketch the SISSO approach for one important class of problems in materials science will follow: constructing materials-properties maps. Then, one application of the method is shown.

3.3 SISSO for building materials-properties maps

A materials-property map (Figure 3) is a low dimensional representation of the materials space where each material is represented by means of a convenient descriptor. The component of the descriptor are the coordinates in the low-dimensional representation such that all materials sharing a certain property (e.g., being metal or topological insulator) are located in the same convex hull. In a useful map, hulls containing materials with exclusive properties (e.g., metals vs insulators) do not overlap.

The mathematical formulation of SISSO for classification[44] substitutes a measure of overlap between convex hulls to the usual mean square error adopted in continuous problems.[44] For a property with M categories, the norm for classification is defined as:

$$\hat{\boldsymbol{c}} = \arg\min_{\boldsymbol{c}} \left(\sum_{I=1}^{M-1} \sum_{J=I+1}^{M} O_{IJ}(\boldsymbol{D}, \boldsymbol{c}) + \lambda \left\| c \right\|_0 \right), \tag{5}$$

where $O_{IJ}(\boldsymbol{D}, \boldsymbol{c})$ is the number of data in the overlap region between the I and J–domain, $\boldsymbol{c}$ is a vector with 0 or 1 elements so that a feature k (the k-th column of $\boldsymbol{D}$) is selected (deselected) when $c_k = 1(0)$, and λ is a parameter controlling the number of nonzero elements in $\boldsymbol{c}$. O_{IJ} depends on $(\boldsymbol{D}, \boldsymbol{c})$ in the sense that the nonzero values of $\boldsymbol{c}$ select features from $\boldsymbol{D}$ that determine the coordinates of the data and the shape of the convex hulls.

The SISSO algorithm provides an efficient solution to Equation 5 also when the number of columns of $\boldsymbol{D}$ (size of the features space) is immense.[44] SISSO has been successfully applied to identify descriptors for relevant materials-science properties.[44,49,52,53] In what follows, as showcase application, a new descriptor found by SISSO for the prediction of stable ABX_3 perovskites is introduced.[49]

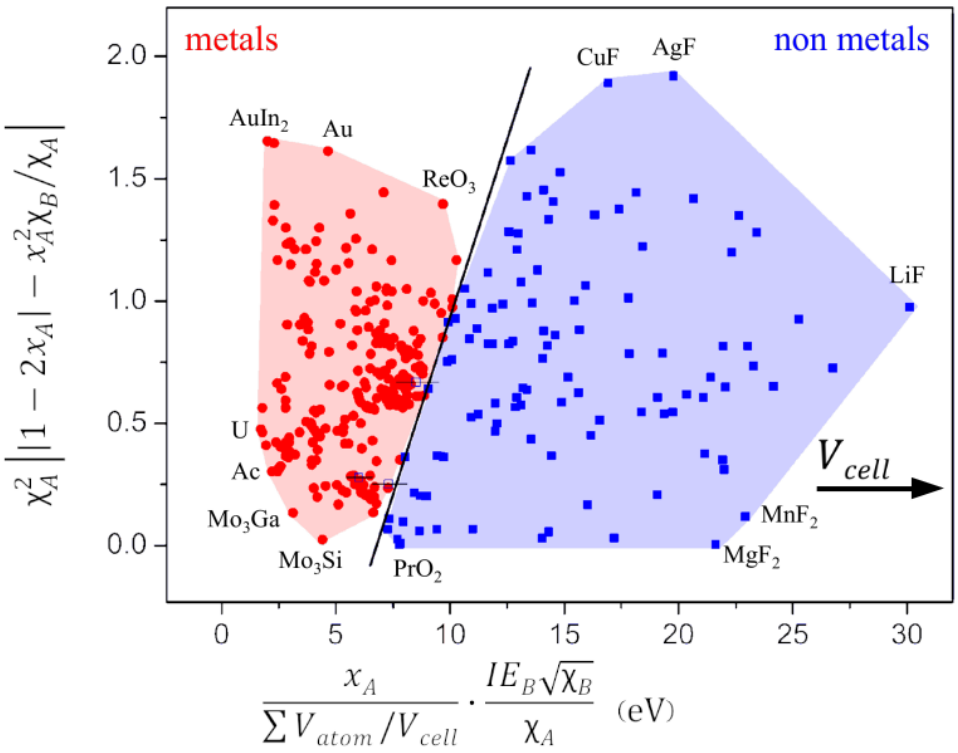

Figure 3: Material-property map for the metal/nonmetal classification (see Ref. 44 for the data and a more detailed discussions). The axes are the components of the descriptor, as found by SISSO, by imposing that materials classified as metal are represented in a (convex) region that does not overlap with the region containing materials classified as nonmetals. In the descriptor, x is the atomic fraction, IE is the ionization energy, χ is the electronegativity, V_{atom} is the volume of a sphere with radius equal to the covalent radius of the element, and V_{cell} is the volume of the unit cell of the considered material.[44] The red circles/blue squares are the training metal/non metal materials.

3.3.1 Stability prediction of ABX_3 perovskites

Perovskite materials possess exceptional properties for a variety of applications such as electrocatalysis, proton conduction, ferroelectrics, battery materials, as well as photovoltaics and optoelectronics.[54–59] ABX_3 perovskite crystal structures are defined as a network of corner-sharing BX_6 octahedra surrounding a larger A-site cation ($r_A > r_B$). While the A and B cations can span the periodic table, the X anion is typically a chalcogen or halogen. Distortions from the cubic structure can arise from size-mismatch of the cations and anion, which results in additional perovskite structures and nonperovskite structures. The B cation can also be replaced by two different ions resulting in a double perovskite with chemical formula $A_2B'B''X_6$.

Predicting the stability of ABX_3 and $A_2B'B''X_6$ compounds remains a longstanding challenge for the discovery of new functional materials. Most of the approaches that address this challenge are computationally demanding, limiting their use to a small set of materials.[60–63] Conversely, descriptor-based approaches enable high-throughput screening applications because they provide rapid estimates of material properties.[64] A notable example of "human learned" descriptor is the Goldschmidt tolerance factor,[65]

$$t = \frac{r_A + r_X}{\sqrt{2}\,(r_B + r_X)}, \tag{6}$$

introduced in 1926 and since then used extensively to predict the stability of ABX_3 perovskites based only on the ionic radii (r_i) of each ion ($i = A, B, X$). The prediction accuracy of t is not very high, especially for compounds containing heavier halides.[66] Considering a dataset of 576 ABX_3 experimentally characterized material compositions,[67–69] the overall prediction accuracy of t is 74%. Using the same 576 ABX_3 materials, Bartel *et al.*[49] set up SISSO by starting from r_i and the oxidation numbers (ν_i). Note that in Equation 6, ν_i are implicitly used to determine r_i. Out of a constructed feature space of 3×10^9 features (up to the third iteration of feature/operator combination), the following 1D descriptor was

identified:

$$\tau = \frac{r_X}{r_B} - \nu_A \left(\nu_A - \frac{r_A/r_B}{\ln r_A/r_B} \right) \tag{7}$$

This new tolerance factor (τ) shows a prediction accuracy of 94% and nearly uniform performance across the five anions evaluated ($X = O^{2-}$, F^-, Cl^-, Br^-, I^-). Like t, τ requires only the chemical composition, allowing the tolerance factor to be agnostic to the many structures that are considered perovskites. In addition, τ provides a monotonic estimate of the probability that a material is stable in the perovskite structure. The accurate and probabilistic nature of τ, as well as its generalizability over a broad range of ABX_3 and $A_2B'B''X_6$ perovskites [with $r_B = (r_{B'} + r_{B''})/2$ in Equation 7] allows for new physical insights into the stability of the perovskite structure. As a direct result, Bartel *et al.* report the prediction of 23,314 new double perovskite oxides and halides.[49]

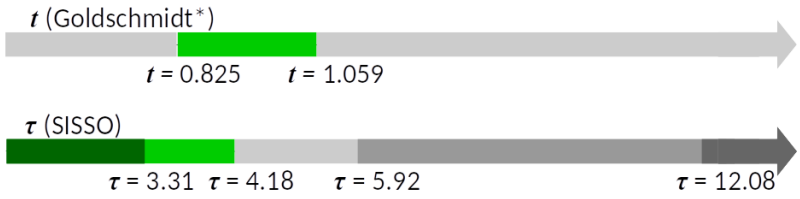

Figure 4: One-dimensional maps for Goldschmidt t vs the newly proposed τ for perovskite-stability prediction. The green (gray) areas are the domains of predicted stability (instability) of perovskites. The boundary of Goldschmidt's t were trained via a decision-tree classifier over the same dataset used for SISSO, hence the asterisk. In the case of τ, the darker green and gray areas are regions of 100% prediction accuracy. So, if for a material τ is smaller than 3.31 or larger than 12.08, its classification is certain. At $\tau = 4.18$, the predicted probability that a material is a perovskite is 50% and the probability to be perovskite smoothly decrease from left to right.

The equations found by SISSO are not then necessarily unique and all components of the descriptors may change at each added dimension. This reflects the approximate nature of the equations and the unavoidable relationships among features. In words, one or more primary features may be accurately described by nonlinear functions of a subset of the remaining features. It is also noted that the mathematical constraints imposed in order to obtain the minimally overlapping convex hulls are very flexible but not complete, i.e., the found descriptor→property relationship is intrinsically approximate.

3.4 The NOMAD Analytics Toolkit

Artificial intelligence approaches like SISSO are promising tools that could become part of the modern materials scientist's set of skills. In this respect, it is fundamental for any researcher adopting such methods to share not only the data used for training the algorithms, but also the (implemented) learning algorithm themselves. This has both educational/tutorial purposes and the merit of improve scientific reproducibility. Besides maintaining a large (and growing) Repository & Archive, the NOMAD Laboratory also provides the infrastructure to share data-analytic tools, in terms of python (or other languages) notebooks. By logging in at `https://analytics-toolkit.nomad-coe.eu`, users can find already tutorial notebooks, for instance, introducing the CS method and allowing for the reproduction of published results such as those presented in Refs. 35,39,42,44,49,52, and more.

3.5 Outlook

Compressed-sensing-based descriptor identification is a promising approach for the artificial-intelligence-assisted determination of maps of materials properties. In particular, SISSO is a powerful tool for the identification of descriptors starting from a huge number of candidates. However, this approach is currently limited to scalar features. This seems to be not a severe limitation in cases where the chemical composition of a material correspond to a well defined structure, including crystal symmetry and atomic arrangement. In this case, suitable descriptors depending on properties of free atoms are readily found. When polymorphism is present, the atomic (local) environment appears to be a necessary input, but currently the approach described in this section lacks of a systematic strategy to construct environment-dependent features of increasing complexity, to be used as candidates in the feature space.

4 Identifying error in machine learning models

The design of new materials has long relied on DFT, molecular dynamics, phase field calculations, and more. While these approaches are very useful, they are also costly in terms of computational resources and time, limiting their utility. In the last decade, we have seen a surge in interest in applying machine learning (ML) techniques to help address these challenges.[70–72] For example, fewer computations need to be carried out if a ML algorithm is able to prescreen compounds of interest.[73,74]

Despite increasingly broad acceptance of ML in the discovery of new materials, there remain common and often valid criticisms[75] which include:

i) Necessity of data. Is there sufficient data in the literature, and how do we organize it in a way that is useful?

ii) ML algorithms are a black box. As such they lack the ability to provide physical insight from a mechanistic perspective.

iii) Suspicions about the ability to extrapolate beyond the training data.

iv) We often do not consider the error, or uncertainty, associated with model predictions.

v) Reported error does not represent the actual ability to predict targets due to overfitting.

vi) Given relatively recent adoption of data science into material science, there remain numerous instances of bad data practices.

The ML community has begun to identify and address these issues in a number of ways.[76,77] Next, a tool to allow materials research practitioners to leverage their chemical knowledge to identify model error is explored.

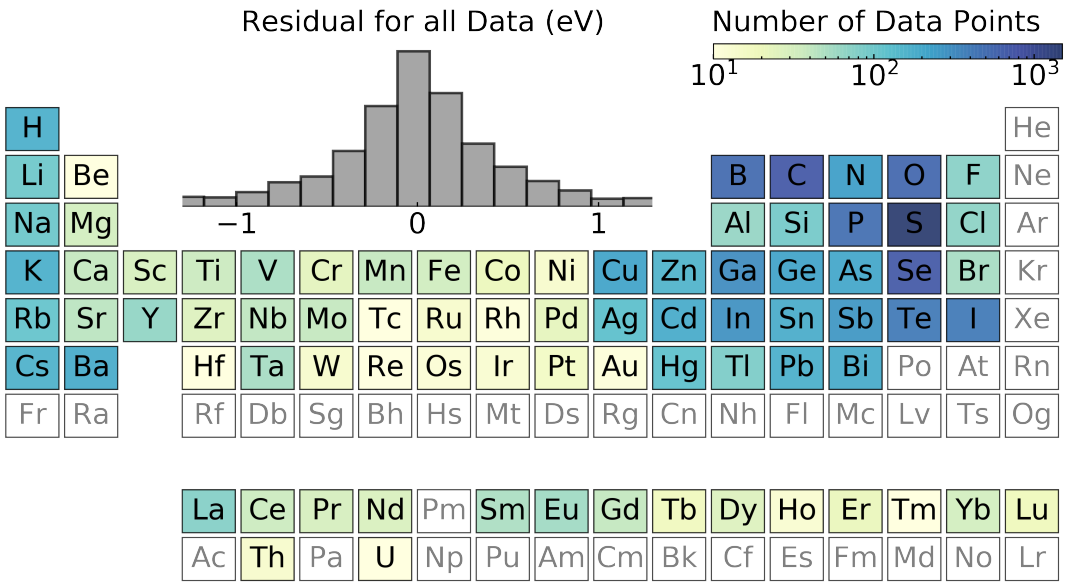

Figure 5: The interactive periodic table allows for quick and efficient exploration of chemical space. The tool is described in detail in Ref. 78. Such tool will also be generalizable for any machine learning model where chemistries are being explored, not just for bandgap.

4.1 An interactive tool to visualize model error and chemistry

The error identification in ML is accomplished by providing an interactive tool to visualize error and chemistry. In our experience, materials researchers want to rely on their own chemical intuition as they address the following questions:

a) Do I have enough data for meaningful learning?

b) Does my data provide the required diversity to predict across a variety of chemistries?

c) Is my data set skewed towards certain types of chemistry?

d) Is my model error artificially low due to overfitting?

At the heart of these questions are two key problems: *i*) understanding the error associated with sparse representation of chemical classes, and *ii*) recognizing the extent of chemical clustering and how clustering may effect performance. As we seek to understand the role of chemistry in model error, it is best described with a model system.

Consider this preliminary tool[78] built using a model that predicts experimental band gap. The model was trained on 2,483 compounds where experimental band gap was known and the details of the model are reported elsewhere.[79] The first thing that this tool provides is a periodic table (Figure 5) where elemental prevalence in the data set is visualized using a heat map. Sorting the data by elements allows us to not only express elemental prevalence, but also demonstrate the error versus number of entries. The overall model may look acceptable, but on closer investigation one can see that certain classes sufferer from systematic error.

Figure 6(a) provides evidence whether the error in these classes could be reduced by obtaining additional entries in this class. In other words, additional data from compounds containing these elements should be gathered to improve accuracy. This same periodic table could be toggled to have the heat map represent the absolute error for compounds containing each element. Moreover, hovering over and clicking on individual elements could then provide element-specific information.

In Figure 6(b) the distribution of residual values for Vanadium is shown. It is also possible to display information regarding the average band gap, the variance in band gap, the percent error, or even things like feature values. Extending this approach to include AND/OR logic (formula contains: O, F and/or Al) is also possible and would allow for a more nuanced analysis. For example, the residual error associated with hydroxides or flourooxides can be considered as opposed to the broader class of oxides. This allows users to visualize if the error is a function of trends from the periodic table— which chemists already know and understand such as: bonding, electronegativity, size, screening, etc.

Interacting with the periodic table to select elements can also allow for a better analysis of residual plots. The current practice of examining outliers which contribute large errors could instead be replaced by examining whole classes of materials at a time and seeing where their error lies compared to the average model residual error. This can be seen in Figure 6(c) where the actual vs predicted band gap of compounds containing vanadium is shown in orange color while the remaining compounds are shown in blue. This visualization allows a

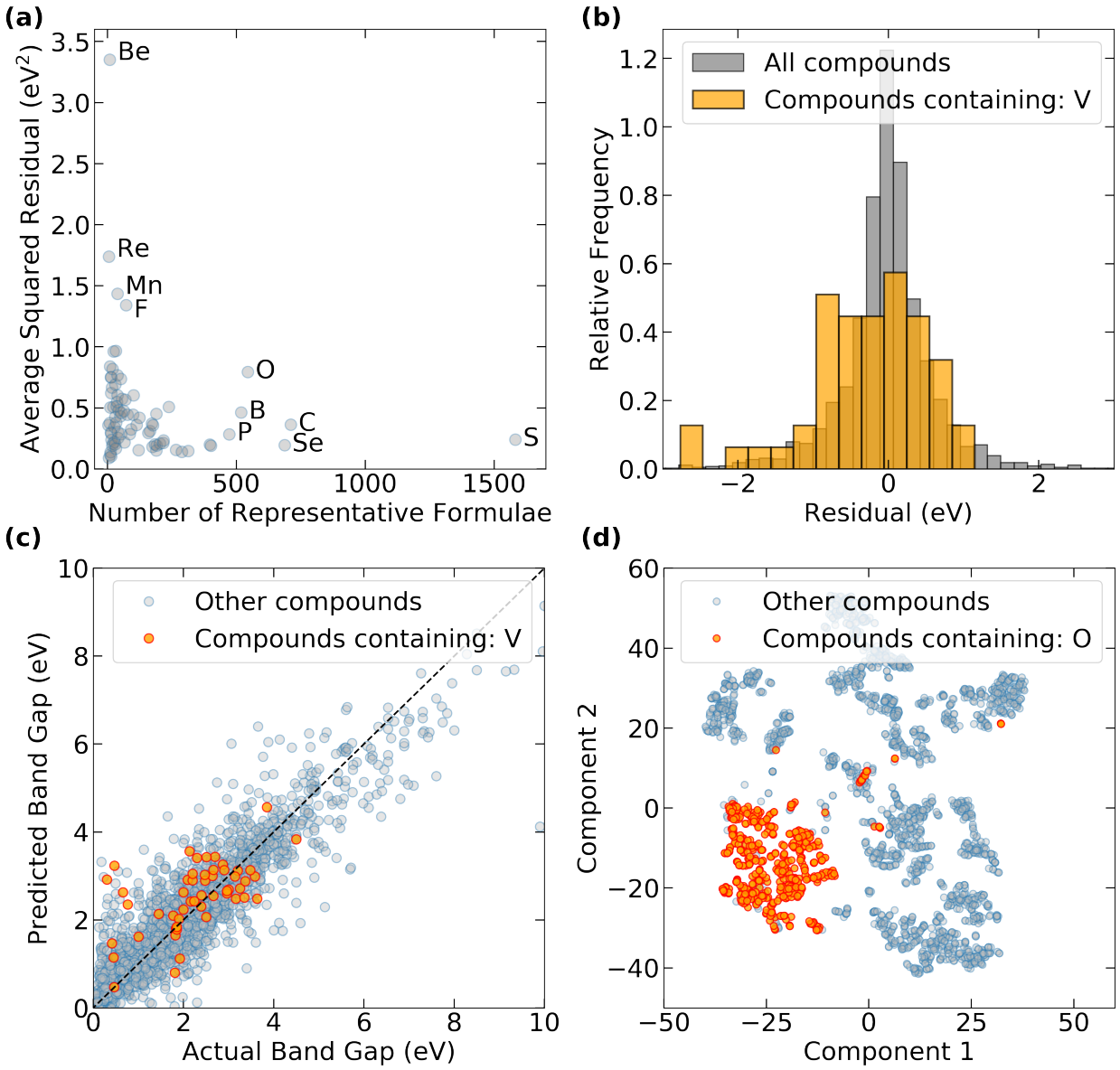

Figure 6: (a) Error decreases as more representative data becomes available. (b) Residual values allow to explore whether there are patterns in the error associated with compounds containing specific elements. (c) The actual versus predicted values for all experimental band gap values. Compounds containing Vanadium highlighted in orange. (d) Extreme example of grouping for compounds containing oxygen on the t-Distributed Stochastic Neighbor Embedding (t-SNE).

user to easily observe an overprediction trend in this class of materials. This observation is confirmed when the residual error histogram for vanadium *vs.* all compounds are compared in Figure 6(b). Furthermore, selecting elements from an interactive periodic table can also provide information about clustering. The dimensionality reduction technique, t-Distributed Stochastic Neighbor Embedding (t-SNE),[80] has been used to cluster data together but determining whether clusters are grouped by chemistry is not straightforward.[81] Users will have to test point-by-point as they seek to establish chemical trends in the clusters.

Visualization of compounds containing specific elements allows for easy identification of which clusters belong to specific chemistries and which chemistries do not cluster. An example is shown in Figure 6(d) where the t-SNE plot clearly shows clustering and one cluster is identified as primarily containing oxides. Is it possible to anticipate that future ML by materials researchers will utilize information from elemental t-SNE diagrams as they select cross-validation training sets in order to prevent overfitting due to interpolation in overly similar data sets.[81]

4.2 Outlook

As researchers embrace the philosophy of data-driven science, we expect great progress to be made in the materials front. In particular, open source projects revolving around sharing of materials data could revolutionize how we think about the field of materials science and engineering. Within this paradigm, the training and sharing of ML-based tools has already become popular for the purpose of predicting materials properties. Although this is an exciting prospect, we should be cautious that the data and modeling efforts give appropriate answers. In particular, the types of materials included in these modeling efforts are often skewed towards specific chemistries. This can lead to a systematic error that is otherwise not accounted for in the reported model accuracies. The increased use of data visualization techniques will allow us to probe these models from a domain driven perspective. Using both materials knowledge and data visualization techniques we can provide researchers with

a strong intuitive feel for how a model performs while also providing a way to visualize and identify common problems that occur in the modeling process.

5 Accelerated ab initio molecular dynamics applied to the simulation of heterogeneous catalysis

The experimental identification of intermediates and surface sites under reaction conditions is challenging. To this purpose, computational approaches based on quantum chemical calculations have become a fundamental tool to understand reaction mechanisms and investigate active surface sites in heterogeneous catalysis.[82,83] The establishment of DFT as an efficient method to solve the electronic structure problem[84] combined with the development of high-performance computing facilities has fostered the investigation of reaction mechanisms occurring on the solids surfaces.

The evaluation of reaction mechanisms on surfaces based on DFT calculations (Figure 7a) generally consists of: *i*) the postulation of possible pathways, i.e., sequences of bond forming and breaking elementary steps that transform reactants into products; *ii*) the geometry optimization of selected initial guesses, locating stationary points of the potential energy surfaces (PESs) and calculating the (electronic) energy of minima and transition states along each postulated reaction pathway (at 0K); and *iii*) the estimation of entropic contributions via partition functions, often assuming that the stationary points of the PES are locally harmonic.[85] These procedures allow to obtain the free energy surfaces (FESs) at the reaction temperature. These FESs are then used to discuss the relevance of the different possible reaction mechanisms. In spite of the popularity of such approach, two severe shortcomings may be associated to it. Firstly, the surface of the catalyst can be highly covered by chemisorbed species under reaction conditions (formation of adlayers); for instance during the industrially relevant Fischer-Tropsch Synthesis and the methanation reactions, among other reactions.[86] For these cases, the energies of reaction intermediates and tran-

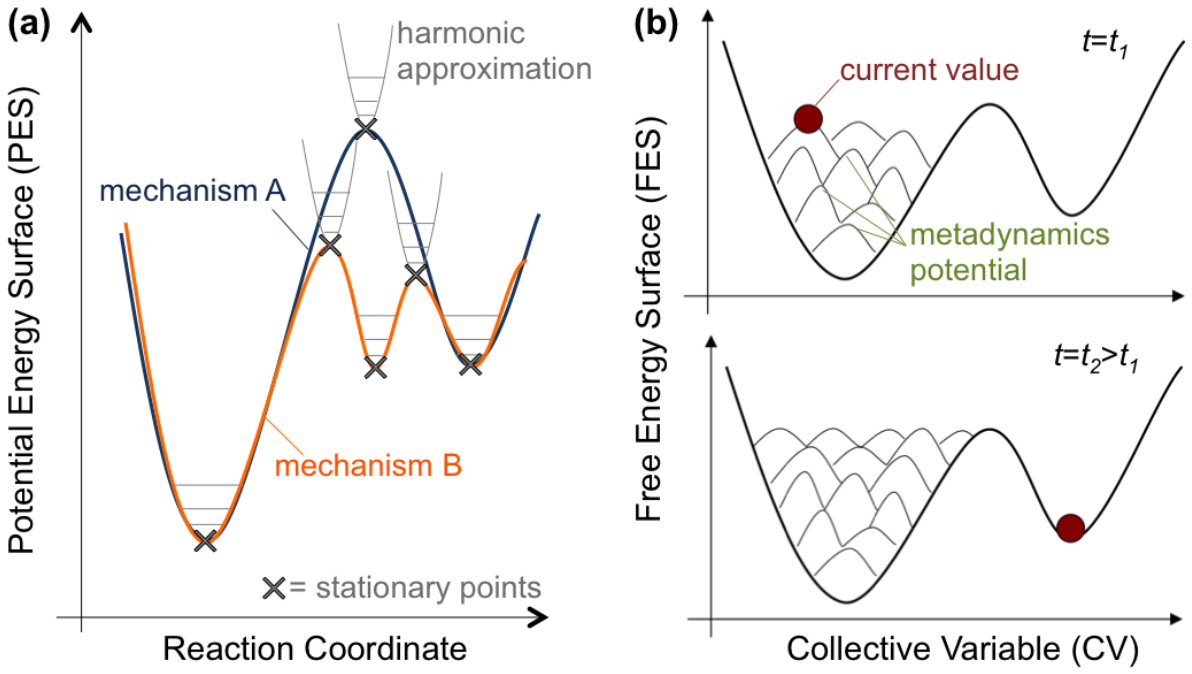

Figure 7: (a) Common approach to evaluate surface reaction mechanisms by DFT calculations: focus on locally harmonic stationary points of PESs corresponding to mechanisms assumed beforehand. (b) AIMD/MetaD approach for reaction mechanism exploration. The history-dependent potential (represented by the Gaussian hills on the FESs in (b)) forces the system to escape from local minima on the FES defined by a set of CVs as the simulation proceeds in time (e.g. t_1 and t_2 shown in (b)).

sition states can be influenced by complex adsorbate-adsorbate interactions. Secondly, the evaluation of adsorbate entropy by the harmonic oscillator model may be over-simplified when anharmonic,[87–89] translational/rotational[90–94] or configurational[95] degrees of freedom are relevant for the evaluation of the free energy of minima and transition states. Aside the above mentioned standard approaches, it is worthy mentioning to mention a recent computational method, namely *Normal-Modes Transition Approximation*, which rephrases the search of transition paths in terms of eigendisplacements of the dynamical matrix of the system.[96] Such method allows to identify possible reaction paths from the only knowledge of the phonon modes of the stable geometry, showing how to control reaction barriers through a fine tuning of the eigenfrequencies of the system.

In this section, modeling approaches to evaluate reaction mechanisms in heterogeneous catalysis based on molecular dynamics. This technique has recently emerged as a promising alternative to overcome the limitations of the PES-based approaches.[97,98]

5.1 Ab initio molecular dynamics

Ab initio molecular dynamics (AIMD)[99,100] is the molecular dynamics (MD) method of choice for the study of reaction mechanisms in catalysis. The electronic structure is explicitly included (*e.g.* at DFT level), allowing the description of bond breaking and forming events. During MD simulations, starting from a given an initial structure, nuclei positions and velocities are evolved in time subjected to determined thermodynamic boundary conditions. The collection of visited states at finite temperatures (trajectory) can then be used for the calculation of free energy differences. Compared to the common evaluation of discrete points of PESs, the free energies obtained from MD simulations include additional contributions that are fundamental to overcome the limitations of modeling surface reactions on adlayers. The calculation is performed on a large number of configurations explored during the simulation at finite temperature — and not only on selected geometry-optimized structures at 0 K — which increases the chances of capturing relevant adsorbate-adsorbate interactions

that affect the energetics of surface reaction mechanisms. Furthermore, the free energy is not calculated using a posteriori correction to the PES, but it is instead obtained on-the-fly during the simulation. This means that the partition functions simultaneously include translational, rotational, and (anharmonic) vibrational degrees of freedom. Despite such benefits, the evaluation of free energy differences by AIMD is computationally demanding. In particular, surface reactions involving energy barriers much higher than thermal energy require relatively long trajectories resulting in prohibitive calculations. This problem can be avoided by coupling the AIMD with the Metadynamics (MetaD) technique[98,101–105]

5.2 Metadynamics

MetaD consists on the exploration of the phase space using a reduced configurational space defined by a set of selected reaction coordinates, called collective variables (CVs) . At regular time intervals during the AIMD simulation, a history-dependent potential (*e.g.* Gaussian functions) is applied forcing the system to escape from (local) already explored minima on the reduced phase space (Figure 7b) For sufficiently large simulation times, the applied MetaD potential approximates the FES and the meta-trajectory follows the minimum free energy pathway. The use of MetaD therefore replaces the need to postulate, beforehand, the detailed sequence of elementary steps. The combination of AIMD with MetaD has been used to unravel the mechanisms of catalytic processes on molecular systems[106] as well as on oxide-supported clusters and metal surfaces.[97,107–109]

5.3 A case study: the Fischer-Tropsch Synthesis

The Fischer-Tropsch Synthesis (see Equation 8) with $n > 1$, which converts syngas (CO/H_2 mixture) to hydrocarbons, is an example of complex reaction taking place at high adsorbate coverage, whose mechanistic understanding has benefited from the use of AIMD (in this case Born-Oppenheimer MD[99,100]) coupled with MetaD simulations at 200 ℃.[97] By using ruthenium flat and stepped surface models covered with co-adsorbed CO and H species

(Figure 8a), the effect of adlayer on the favoured reaction mechanisms and the active sites for CO activation, the highly debated key step of the reaction, was addressed:

$$n\mathrm{CO} + (2n+1)\mathrm{H_2} \leftrightarrows \mathrm{C}_n\mathrm{H}_{(2n+2)} + n\mathrm{H_2O}, \quad \Delta\mathrm{H}^{\circ}_{298} = -167 \text{ kJ/mol}. \tag{8}$$

AIMD/MetaD simulations were performed by using a set of three CVs, namely C-O distance, C-H coordination number and O-H coordination number. The simulations allowed to capture, simultaneously several mechanisms involving zero or several hydrogen transfer steps to both C and O-end of the adsorbed CO molecule, in any order, before the actual elementary step of C-O cleavage. It was found that the CO activation mechanism via the formyl intermediate (HCO) is the most likely one on the flat surfaces (Figure 8b), in line with previous proposals.[110] Conversely, in the case of the stepped surface, hydrogen-assisted routes *via* the COH intermediate are the most favored ones (Figure 8b).[111] This is because adsorbed H preferentially bound to step-edges can be easily transferred to carbon monoxide O-end at high coverages. The comparison of the reaction intermediates stability calculated by the evaluation of discrete points of the PES and the AIMD/MetaD approach reveals that the dynamic effects are hardly captured by the static approach, due to complex adsorbate-adsorbate interactions.

The methanation reaction on ruthenium (Equation 8, with $n = 1$) was also studied, using the same models and methodology at a higher temperature (400 ℃).[98] The simulations revealed that, in the presence of step-edges, an unusual low-energy mechanism, involving four hydrogen transfer steps and the simultaneous C-O cleavage with the formation of CH_2 species and H_2O, is available on the stepped surface (Figure 8c). This mechanism is entropy-driven, since the C-O bond activation step involves the formation of a water molecule, which readily desorbs from the surface. These results reveal how valuable can be the AIMD/MetaD approach in capturing entropy-driven mechanisms at higher temperatures. Despite the use

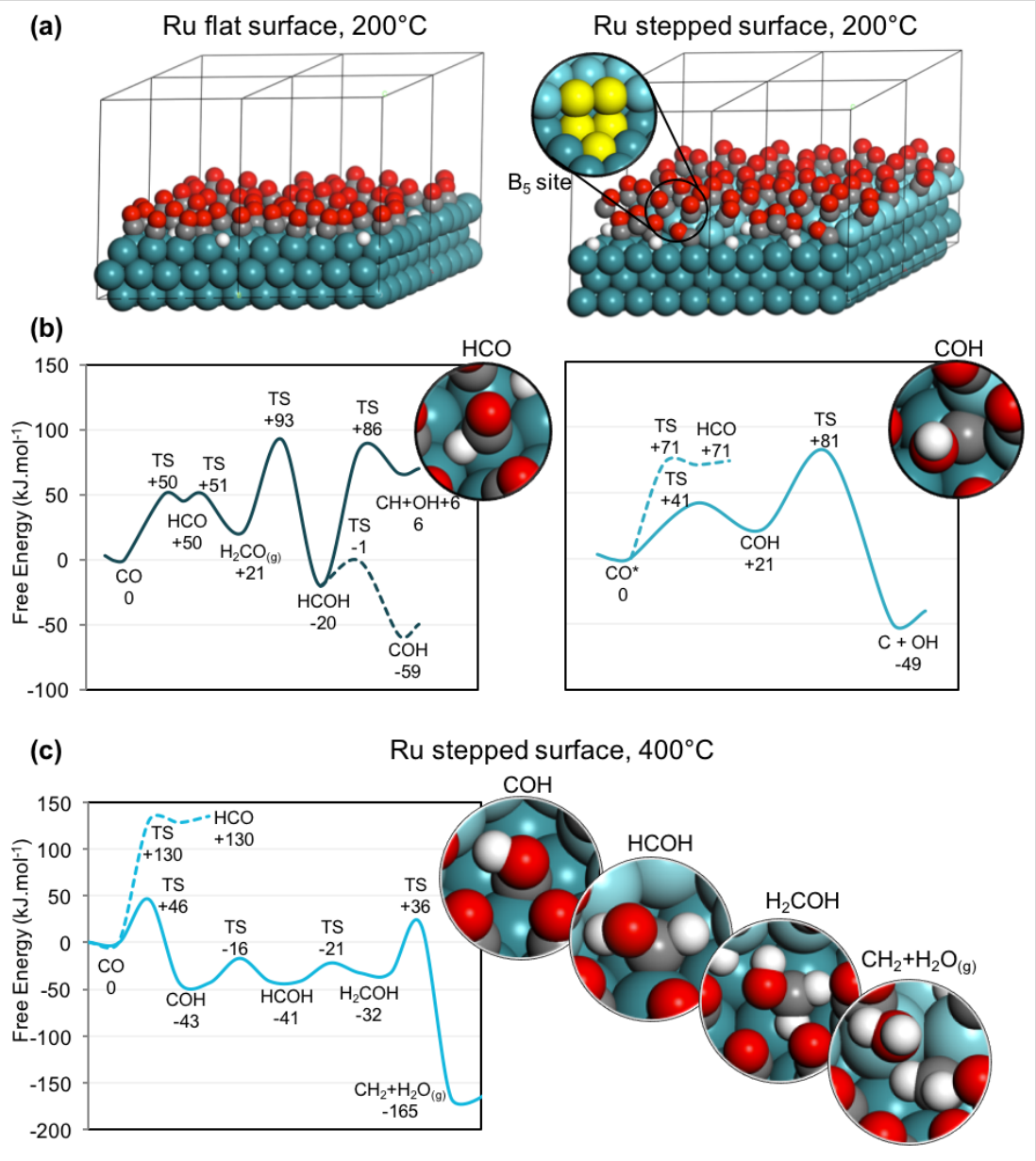

Figure 8: (a) CO activation at Fischer-Tropsch reaction conditions (200 °C) modeled by AIMD/MetaD simulations: Ru flat and stepped model surfaces (containing step-edge sites shown in the inset) covered with CO/H adlayers and (b) FESs for observed mechanisms: HCO vs. COH intermediates on the flat and stepped surfaces, respectively (shown in the insets). (c) CO activation at methanation reaction conditions (400 °C) modeled by AIMD/MetaD simulations: FES for mechanism identified on the stepped Ru surface involving multiple hydrogen-transfers and water elimination (reaction intermediates shown in the insets). Ru, C, O, and H atoms are shown in blue, gray, red and white, respectively. The Ru atoms of the top layer in the Ru stepped surface are shown in lighter blue. The simulation cell is shown in black (a 2×2 supercell is represented). a) and b) adapted from Ref. 97; c) adapted from Ref. 98.

of MetaD to accelerate the AIMD simulation, the computational effort needed for such simulations, which need the evaluation of the electronic structure at each time step of the MD run, is still high and some of the limitations of the approach are associated to it. If on one hand the MetaD potential allows crossing of energy barriers, on the other hand the simulation time scale (in the order of ps) is not long enough to allow equilibrating of gas-phase species with the surface. This means that the coverage is fixed during the simulations and needs to be carefully determined beforehand *via*, for instance, ab initio thermodynamics.[112] The accuracy of FESs calculated by MetaD[102,113] depends on the shape of the biasing potential (Gaussian hill height and width) as well as on the frequency at which it is applied; there is thus a compromise between the accuracy and the length of the simulated time. Larger hill width and height applied more frequently, for instance, will enable quicker exploration of the free energy landscape, but will also smear out the details of the FESs and increase the error of the simulaiton. Another limitation of the MetaD technique is related to the choice of CVs, since mechanisms that are not described by the chosen set cannot be accessed.

5.4 Outlook

The application of the AIMD/MetaD techniques to catalytic processes, occurring on the materials surface, shows its potential to unravel favorable reaction mechanisms in heterogeneous catalysis. Such techniques result to be particularly useful in the case of reactions that occur at high coverages, where adsorbate-adsorbate interactions modulate the preferred pathways. Nevertheless, the high cost of the simulations is still a drawback. The recent development of accurate and less resource-consuming representation of the PES by statistical methods[114] represents a promising alternative to overcome such limitation, which could enable the systematic analysis of reaction networks in heterogeneous catalysis by AIMD simulations.

6 Predictive description of catalytic systems using microkinetic modeling

Ab initio derived free energy landscapes embedded within kinetic and Monte Carlo models,[115–129] are a recent evolution necessary to bridge the gaps between theory and experiment in catalytic systems modeling (Figure 9a). This gap can either be bridged in a top-down fashion, using parameter fitting and regression analysis, or in a bottom up fashion, using *ab initio* data.[119,130]

Within the bottom-up approach, temperature and pressure gaps can be sufficiently bridged by the embedding of a computational reaction network (computational reaction kinetics) within kinetic model and/or Monte Carlo models. However, it remains challenging to make a realistic atomistic model(s), which should be representative enough for the studied catalyst.

Recently, *ab initio* based kinetic and Monte Carlo models have demonstrated their usefulness to get insights into reaction mechanisms onto various catalyst models, such as metal nanoparticles,[131] periodic metal-surfaces,[123,124,128] as well as oxides,[125,126] and even metal-oxide interfaces.[122,127,129] The computational catalyst development has frequently used simplified reaction networks by exploitation of scaling relations. These have been known in various subfields of chemistry for several decades as Brønsted relations, Evans-Polanyi relations,[132,133] and Hammett equations.[134] The computational prediction of qualitative structure-activity relationships or QSARs facilitates the development of more active new catalysts. Within the last two decades, Nørskøv and co-workers have focused on the application of DFT on metal surfaces to identify computational activity descriptors.[135–139] Plotting the logarithm of the turn over frequency in function of one or more descriptors, allows the construction of one- or multidimensional "volcano-plots" (Figure 9b). A famous example of a descriptor is the N_2 dissociation energy (EN-N) in case of the NH_3 synthesis.[137,138] Besides numerous examples of energy descriptors, for example,[137,138,140,141] there are other frequently

used descriptors, such as the *d*-band center.[135,142,143] The *d*-band center can for example be employed to rank metals for their CO dissociation potential.[144,145] By constructing scaling relations and embedding these within *ab initio* Micro-Kinetic Models (MKM), it is possible to map the catalytic activity onto a $1D$ or $2D$ descriptor space and obtain activity and selectivity maps.[139] The resulting activity maps can be viewed as a quantitative implementation of the classical Sabatier principle.[146] This screening approach is applied frequently to metal surfaces,[146,147] and it allows the selection of optimal metal alloys.

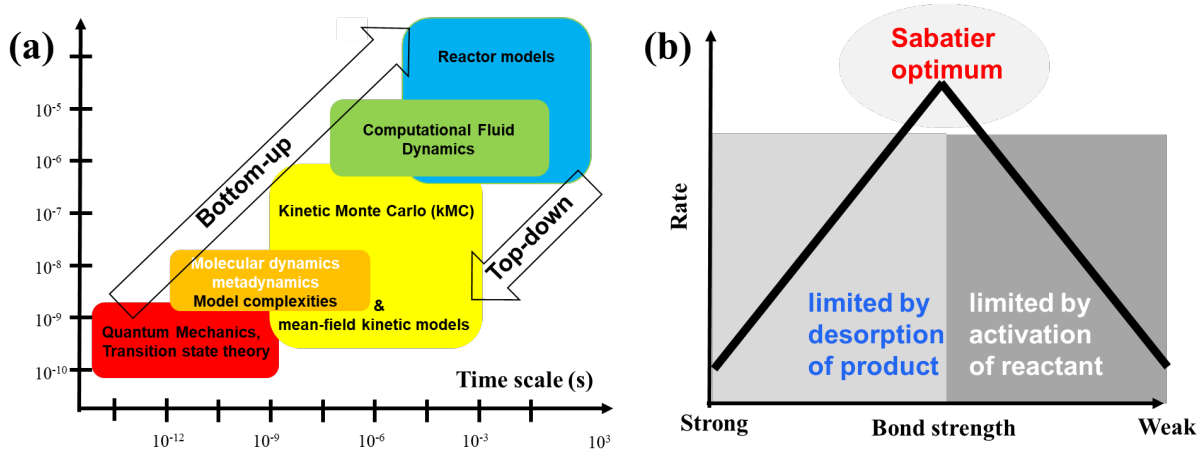

Figure 9: (a) Top down and bottom up catalyst development / length and timescales, (b) Sabatier principle, which states that there is an optimum "bond strength" defining the best catalyst for a given reaction, (partially based on refs. 119 and 146).

The computational screening approaches that exploit scaling relations between activation energies and reaction energies are also dependent on (i) the reaction mechanism and (ii) the atomistic model.[135–138,148] Furthermore, the simplified scaling approach still lacks complexity, and is unable to describe possible catalytic interface effects and support effects, confinement effects, etc. In most cases adsorbate-adsorbate interactions on metallic systems and adsorbate pairing effects on oxides are also neglected when scaling relations are constructed. This explains why most state-of-the-art kinetic models cannot predict catalyst activities and selectivities reliably. It is thus clear that existing microkinetic models can be improved by the addition of more complexities.

6.1 Embedding complexities within the microkinetic modeling on interface catalysts: the case study of CO oxidation on PtSn

Sometimes it happens that the classical reaction route can be circumvented by another reaction route, e.g. a route taking place at a catalytic interface. Then, the computational description of interfaces becomes important since the presence of interfaces creates new reaction mechanisms.

In recent years, a variety of atomistic models and/or computational reaction pathways have been presented describing reactions onto catalytic interfaces, for example for CO_2 conversions,[127,129,149–153] and CO oxidation .[122,154–161] While the reaction networks are studied in detail on these interface catalysts, they are frequently not included within microkinetic models and even for developed existing ab initio kinetic models[122,127,129] there is still room to implement more complexities.

For CO oxidation on PtSn nanoparticles, the low temperature CO oxidation activity arises from the presence of a SnO_X/Pt interface.[122] The idea that SnO_X/Pt interfaces were responsible for the catalytic activity was postulated initially by the renowned Somorjai group in 2014.[162] The likelihood to form such SnO_2/Pt interfaces can be studied via ab initio thermodynamics, by ranking different studied phases according to their most stable surface energy in function of the chemical potential ($\Delta\mu_i$) for CO and O_2 (Figure 10).

As chemical potentials are functions of temperature and pressure, it is possible to plot the corresponding pressure axis for each temperature, for example at 400 K (Figure 10a). At regular operating conditions for CO oxidation, *i.e.* pO_2 and $pCO > 0.01$ bar, the segregated system of a Pt-skin and SnO_2-bulk is thermodynamically more feasible compared to the bare alloy phase. However, a more likely situation is presented in Figure 10b, where a bulk-like SnO_2 rod is formed that is 0.72 eV/SnO_2 higher in energy compared to bulk SnO_2,[122] the dotted line in Figure 10a. Different sites can be present at a SnO_2/Pt-skin interface. Therefore, a representative number of interface sites should be evaluated and included within kinetic and Monte Carlo models.

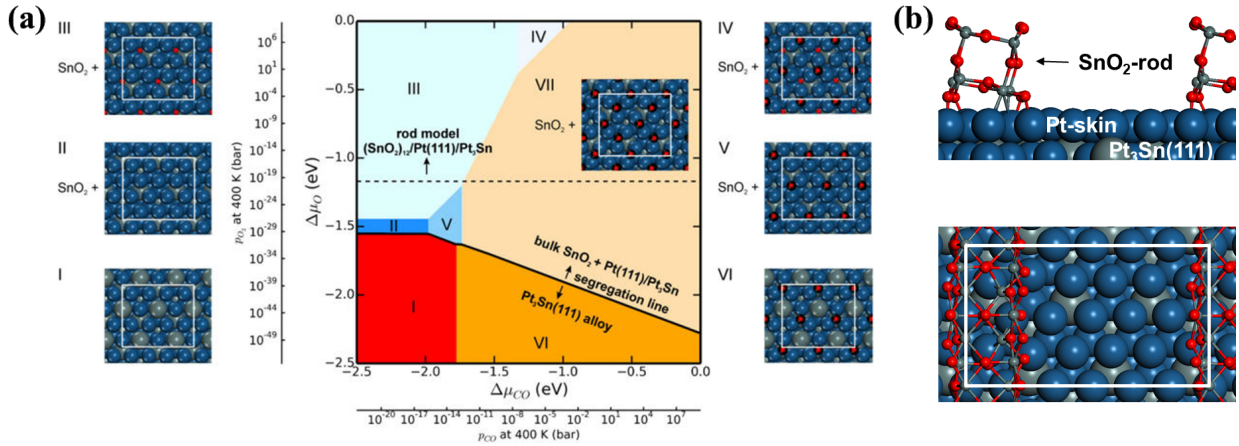

Figure 10: (a) Thermodynamic phase diagram showing the preferred phase [lowest difference in surface energy with respect to $Pt_3Sn(111)$] as a function of differences in chemical potential ($\Delta\mu_i$) for CO and O_2. The solid black line indicates segregation from a $Pt_3Sn(111)$ surface to $Pt/Pt_3Sn(111)$ and bulk SnO_2. Structural models for the phases I-VII are shown. (b) The dotted line shows the conditions, when the formation of the rod model becomes thermodynamically preferred. The surface cells are indicated by white rectangles. Atomic color codes: C in black, O in red, Sn in green and Pt in blue (based on ref. 122).

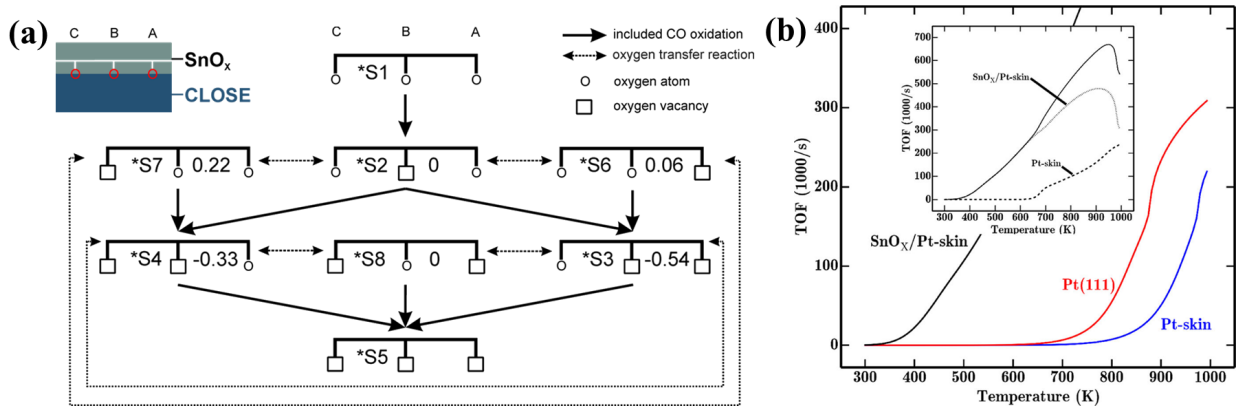

Figure 11: (a) Considered reactions for the SnO_X/metal interface model or $SnO_X/Pt(111)/Pt_3Sn$ model within the mean-field microkinetic model. The energy differences between SnO_X-states with the same number of oxygen atoms are given in eV (displayed green). (b) Comparison of the TOF for Pt(111), $Pt(111)/Pt_3Sn$, and $SnO_X/Pt(111)/Pt_3Sn$ (inset). Different contributions to the total TOF for $SnO_X/Pt(111)/Pt_3Sn$. The partial pressures for CO and O_2 are 11.0 and 21.4 mbar, respectively. (Based on Ref. 122).

For the SnO_2 rod (Figure 10b), a reaction scheme can be constructed based on the three different possibilities into which oxygen can react with CO (A, B and C in Figure 11a). This results in a network containing eight different states of the rod (*Si, where i is the state, Figure 11a), which can be embedded as a microkinetic model with 23 elementary reactions, accounting for regeneration steps as well as transfer steps between states of the rod with the same number of oxygen atoms.[122]

This microkinetic model for CO oxidation at the chosen SnO_2/Pt interface can then be compared with a model for CO oxidation on Pt(111) (Figure 11b). The co-catalytic role of a SnO_2 rim is clearly manifested in an enhanced activity at low temperatures. Furthermore, the interface is even found to solely contribute to the CO oxidation rate below 600 K. To make this kinetical model for CO oxidation work, several complexities need to be included: coverage dependent adsorption energies and CO oxidation barriers. Moreover, for a mean-field microkinetic model, also a realistic determination of a representative site distribution is required (SnO_2: 12.6 %, interface: 15.7 %, metal: 71.7 %) as well as diffusion possibilities for CO from metal to near (SnO_X/Pt interface)-sites.

6.2 Outlook

Within computational catalysis, there is a trend to validate whether the catalytic model systems are representative at operating conditions based on ab initio thermodynamics. The reaction network is closely related to the type of active sites and the coupling of various routes within microkinetic models allows to distinguish which routes are more feasible based on rate control analysis, which is a promising technique to evaluate microkinetic and Monte Carlo methods.[163–166] The technique allows to extract the rate controlling reaction mechanisms, i.e., those that contribute most to the turn over frequency.[122,129]

The computational determination of the apparent activation barrier and reaction orders for a given reaction conditions remains necessary to achieve a good comparison with the experimentally measured activation barriers and reaction orders.[125] Nevertheless, the type

of active sites can vary a lot, especially within model systems describing interfaces, which means that a representative distribution of sites needs to be investigated before a correct activity picture can be constructed.

Catalyst changes during a catalytic run remain hard to describe. No models can yet describe the adsorbate restructuring of metal nanoparticles upon adsorption. Nevertheless, kinetic Monte Carlo methods have been successfully implemented to describe the aggregation of different catalyst particles as a function of temperature.[167] However, it remains a major challenge for the future to describe the restructuring based on adsorbates. For CO oxidation on metal nanoparticles, this restructuring during reaction could include a coordination number and coverage dependent scaling of adsorption energies and barriers, as successfully implemented for nanoparticles of different shapes.[131] Summarizing, bridging the pressure and temperature gaps becomes feasible via using ab initio micro-kinetic models or Monte Carlo models and implementing catalyst dynamics to bridge the materials gaps remains a major challenge for the future.

7 Atomic design principle for safer battery materials

One of the main concerns with respect to high-energy batteries is safety. Li-ion batteries exhibit so-called dendrite growth[168] that can lead to short-circuits and to subsequent battery fires.[169,170] The process of dendrite growth is rather complex,[170] and the reasons for its occurrence are not fully understood yet. Interestingly, while Na-ion batteries also show dendrite growth,[171] Mg-ion batteries do not.[172] Unfortunately, existing models for dendrite growth are typically not element-specific and, therefore, are not able to explain why Li and Na exhibit dendrite growth, but Mg does not.

7.1 The dendrite growth problem

Growth processes require mass transport and recently it was suggested that there might be a correlation between the height of diffusion barriers of Li, Na and Mg and their tendency towards dendrite growth.[173] Indeed, DFT electronic structure calculations found that Mg has a diffusion barrier on its most stable surface termination that is one order of magnitude smaller than the corresponding diffusion barriers of Li and Na.[173] Based on these results, it was argued that low diffusion barriers lead to a high mobility of the deposited metal atoms so that they can easily attach to existing step edges and lead to the growth of smooth surfaces. In contrast, high diffusion barriers lead to immobile surface atoms which are the origin of rough surfaces.

Concerning the growth environment of dendrites, it was found in Li deposition experiments that the formation of needles occurs both in an electrochemical environment as well as under vacuum conditions.[174] This indicates that the growth of Li dendrites is an inherent property of lithium itself. Moreover, it is important to note that for the growth of smooth surfaces also the diffusion barrier across step edges, the so-called Ehrlich-Schwöbel barrier,[175,176] is critical. When metal atoms are deposited on top of an existing island two-dimensional growth will only result if the atoms are easily able to propagate to the lower terrace. Now, the transfer from the upper to the lower terrace across the step is typically hindered by rather large barriers, as the diffusing atom has to propagate through an energetically very unfavorable low-coordinated configuration. This is illustrated in upper right panel of Figure 12 which indicates that the diffusion process across the step in the so-called hopping mode is hindered by a large barrier.

In an recent DFT study, diffusion barriers of Li, Na and Mg across steps, as illustrated in the upper panels of Figure 12, have been considered.[177] Furthermore, the study was extended to the diffusion of zinc and aluminum, which correspond to promising beyond-Li battery systems.[178–180] These calculations confirmed the previous findings, showing that the Li and Na bcc metals also exhibit relatively large barriers for diffusion across steps. On

the other hand, on the hcp metal Mg, propagation across steps is facilitated through the exchange mechanism,[181] that is illustrated in the upper left panel of Figure 12. Instead of hopping from the upper terrace to the lower terrace across the step through a low-coordinated configuration, as shown in the upper right panel of Figure 12, the adatom from the upper terrace pushes an step atom away from the step onto the lower terrace thereby replacing it. Although in this mechanism two atoms have to move, they maintain an high coordination number along the minimum energy path making it energetically favorable. The lower panels of Figure 12 illustrate the consequences of these two different mechanisms. If the barriers to propagate from an upper terrace to a lower terrace are large, then atoms deposited on upper terraces or islands will remain there which will lead to rough surfaces. These could then act as nuclei for the dendrite growth which can cause short-circuits in the batteries and thus battery fires, as indicated in the right panels of Figure 12. If, on the other hand, the diffusion barrier to propagate to the lower terrace are rather small, then atoms deposited on the upper terraces will easily leave these upper terraces, attach to the step edges at the lower terrace and thus lead to the growth of smooth surfaces, as illustrated in the left panels of Figure 12.

Although in this mechanism two atoms have to move, they maintain an high coordination number along the minimum energy path making it energetically favorable.

Diffusion on aluminum and zinc, whose most favorable surface terminations like Mg correspond to densely-packed hexagonal structure, is also only hindered by rather small barriers. However, it is well-known that the growth of dendrites in Zn-based batteries is a serious issue.[182] Thus it seems that there is an inconsistency between Al and Mg on the one side and Zn on the other side, as far as the correlation between the height of the diffusion barriers and the tendency towards dendrite growth is concerned. On the other hand, it has been shown that, in fact, the conversion of Zn to ZnO during battery discharge is critical for the occurrence of dendrites in Zn-air batteries.[179,180] Typical Zn anodes are made of loosely connected Zn powder and polymer binder. Upon discharge, resistive ZnO forms between

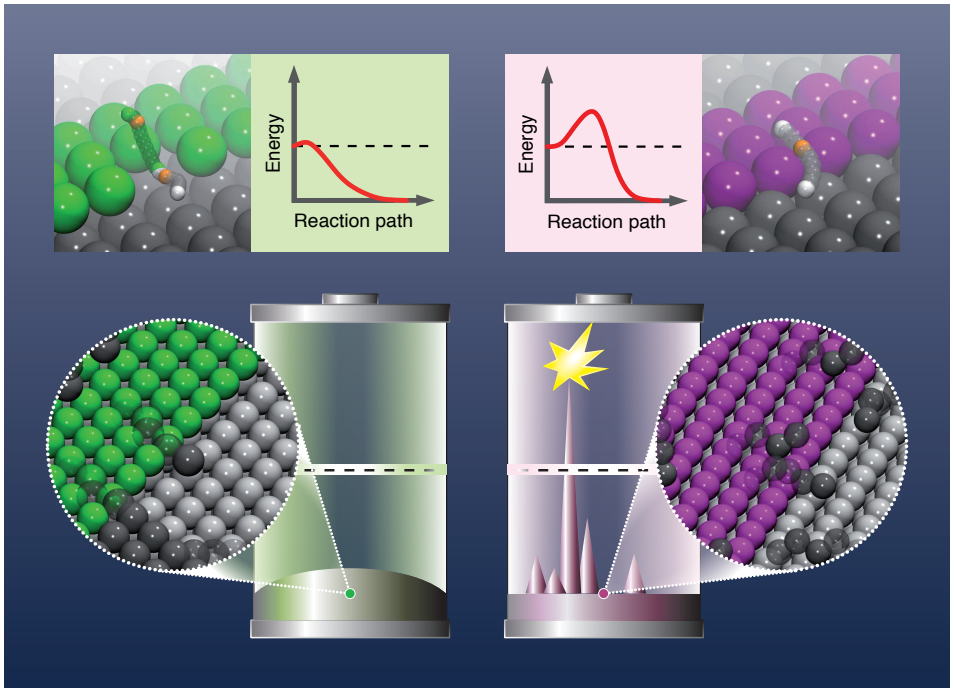

Figure 12: Illustration of the relation between diffusion barriers across step edges and the tendency towards dendrite growth in batteries. The two upper panels depict diffusion paths from the upper to the lower terrace, whereas the two lower panels illustrate the consequences of the diffusion barriers on the growth mode of the deposited metal atoms. Right panels: If diffusion from the upper to the lower terrace occurs in the hopping mode, large barriers results. Thus the deposited metal atoms tend to stay on upper terraces and islands, leading to rough surfaces and eventually dendrite growth. Left panels: Diffusion across the step in the exchange mode is usually associated with small barriers. Thus deposited metal atoms can easily move to the lower terraces leading to the growth of smooth flat surfaces thus prohibiting dendrite growth.

the particles interrupting the interparticle conductivity which has been proposed to lead to dendrite formation.[179] Zn dendrite growth can in fact been suppressed, if the Zn anode is kept metallic by using a sponge-like Zn anode with interconnected continuous Zn domains.[179,180] This indicates that dendrite growth is caused by the formation of ZnO needles, i.e., by the loss of metallic properties. Consequently, it does not correspond to an inherent property of Zn, as also suggested by the calculations presented above. Thus, from the theoretical considerations together with the experimental observations, a design principle for dendrite-free metal anodes can be derived, as illustrated in Figure 12. This will help to select a metal with low self-diffusion barriers, thus preventing the dendrite growth, and to maintain the metallic properties during charging and discharging.[177]

7.2 Outlook

Note that, in the study described above,[177] no full theory of dendrite growth has been presented. Rather a correlation has been found between a property of the considered material, the height of self-diffusion barriers, and an observable related to this material, namely its tendency towards dendrite growth. Hence the height of the diffusion barriers can be used as a descriptor for possible dendrite growth. The concept of descriptors has been discussed in detail in section 3 of this work. There it has been shown how descriptors can be learned from gathered data of materials in a machine learning approach. Here the descriptor has been rather proposed based on physical reasoning. Independent of how the descriptor has been identified, it represents a very powerful tool for improving materials properties. A very first selection of promising materials does not need to be based on a full study of its desired properties but rather on whether the materials value of the descriptor for the desired property falls in the desired range. Furthermore, it also provides a design principle for materials with the desired properties. In the case of dendrite growth in batteries considered here, the results presented above suggest that diffusion of metal atoms deposited on the electrode should be kept facile.

Still it should be kept in mind that here no simulations of dendrite growth have been reported. Note that also for Mg the formation of dendrites during electrodeposition has been observed[183] although it is typically assumed the Mg does not exhibit dendrite growth.[172] Hence further theoretical studies are required in order to clarify the connection between self-diffusion properties and the tendency towards dendrite growth,[184] taking the electrochemical environment at the interface between electrode and electrolyte more realistically into account.[185]

8 Responsive molecular solids

Molecular solids are an attractive prospect for low-to-medium temperature device applications,[186–188] because molecular design can access virtually limitless chemical diversity and can tap into the large body of knowledge on synthetic routes, structure-property relationships, supramolecular assembly and crystal engineering to match the properties to the application. Many molecular materials are amenable to solution processing, providing flexibility for incorporating them into device structures, and can meet increasingly-important practical concerns such as being non-toxic and prepared by environmentally-friendly chemical processes from earth-abundant elements and sustainable chemical feedstocks.

Quantum-chemical modeling has long been instrumental to understanding structure-property relationships in molecules, and advances in techniques for modeling periodic systems and the capabilities of high-performance computing (HPC) have led to an explosion in theoretical screening studies on inorganic solids.[189] The generally larger and lower-symmetry crystal structures formed by molecular solids pose a bigger challenge, but capabilities are rising to meet demand. As we will see, modeling studies play an increasingly valuable role in understanding the link between the molecular species, solid-state structure and physical properties of functional molecular solids, and are particularly powerful when combined with state-of-the-art experimental techniques.

Two example classes of responsive molecular solids are here reviewed, with a particular focus on highlighting the interplay between experiment and theory that has led to a fundamental understanding of their behavior and properties.

8.1 Vapochromism in Pt-"pincer" complexes

Cyclometallated square-planar Pt(II) complexes based around tridentate "pincer" ligands (Figure 13a) are widely studied for their tunable luminescence[190–192] and have applications including as organic light-emitting diode (OLED) emitters and biological imaging agents.[186–193]

Stacking of the planar molecules through supramolecular assembly in solution or in the solid state causes the occupied Pt d_{z^2} orbitals to interact, producing a frontier molecular orbital (MO) above the π MOs on the aromatic ligand (Figure 13b).[188] This results in strong metal-metal ligand charge-transfer (MMLCT) optical absorptions that in the solid state are highly sensitive to the crystal packing.[194] The stacking also produces channels allowing small molecules to diffuse into the crystal and interact with functional groups, either on the pincer scaffold or the ancillary ligand at the fourth Pt coordination site,[195–197] which modulates the energies of the frontier orbitals, widens or narrows the energy gap, and shifts the onset of absorption.[195]

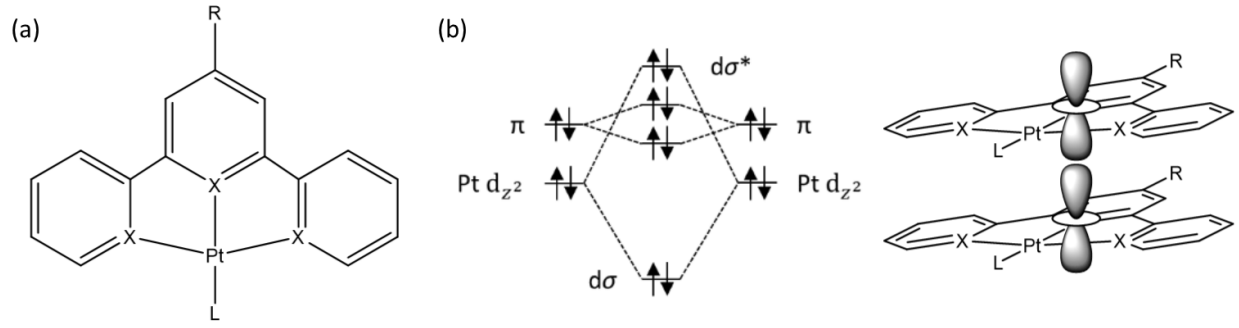

Figure 13: (a) Structure of a general Pt(II)-"pincer" complex, where the symbol X may represent N^C^N, N^N^C or C^N^C depending on the chosen ligand skeleton. (b) Vertical stacking through supramolecular assembly or in the solid state leads to overlap of the Pt d_{z^2} orbitals, producing a new metal-metal d$\sigma*$ orbital higher in energy than the pincer-based π orbitals.

There are several of examples in the literature of pincer complexes exhibiting vapochromic responses to small-molecule analytes. [PtCl{$C_6H_2(CH_2NMe_2)_2$-2,6-OH-4}] undergoes a reversible solid-state reaction with SO_2 gas on the timescale of minutes which is accompanied by a change from colorless to orange.[198] [Pt(Me_2bzimpy)Cl]Cl·$2H_2O$ (Me_2bzimpy = 2,6-bis(1-methylbenzimidazol-2-yl)pyridine) changes from yellow to red on exposure to methanol, chloroform, ethanol and acetonitrile, while the corresponding PF_6^- salt shows a selective color change from yellow to violet when exposed to acetonitrile.[194] A similar response is also shown by the dimethylformamide (DMF) solvate [Pt(Me_2bzimpy)Cl](PF_6)·DMF.[199]

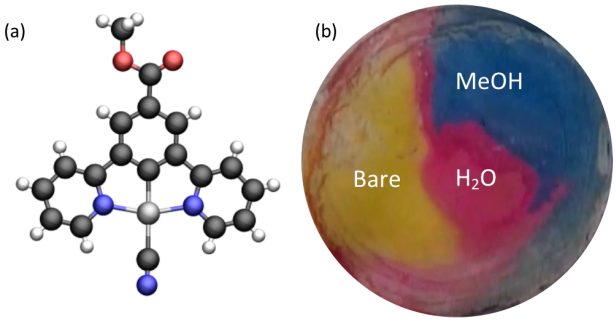

Figure 14: (a) Molecular structure of the Pt complex reported in Ref. 195, taken from the X-ray structure without guest molecules (CCDC: GEJTOH). (b) Image of a microcrystalline thin film of the compound showing the desolvated ("bare") yellow form and the vapochromic responses to H_2O (red) and MeOH (blue).

Recently, a new vapochromic system was identified based on the 1,3-di(2-pyridyl)benzene (N^C^N) pincer skeleton with R = C(O)OMe and L = CN.[195] Quantum-chemical calculations were used to screen potential ancillary ligands, from which the cyanide complex (Figure 14a) was selected based on (1) a high-energy Pt d_{z^2} orbital, placing the solid-state MMLCT band within the visible spectrum (Figure 13b), and (2) the high polarity and potential to form strong hydrogen bonds to guest molecules in the crystal structure. Microcrystalline thin films coated on glass or impregnated flexible polymer films showed selective subsecond responses to dry gases, water and methanol, changing between a yellow empty structure, a red hydrate and a blue methanolic form (Figure 14b).

Using synchrotron radiation, high-quality single-crystal X-ray structures of the dry (yel-

low) form and the hydrate and methanol solvate (red/blue) were obtained, allowing the electronic structures to be modeled. The calculations confirmed the conceptual picture in Figure 13b, with the highest-occupied crystal orbitals (HOCOs) being degenerate chains of antiphase Pt d_{z^2} MOs and the lowest-unoccupied crystal orbitals (LUCOs) being pincer-based π MOs supporting strong MMLCT absorptions. By comparing the empty and solvated crystal structures, it was shown that the different patterns of H-bonding between the solvents and ancillary CN ligand changed the Pt-Pt distances and the offset between the Pt centers, modulating the degree of orbital overlap and the resulting HOCO energy. The calculations also revealed secondary interactions between LUCOs which led to a further cooperative reduction in the gap and red shifted absorption with increasing overlap.

This study highlights the role of modeling both at the molecular-design phase and in understanding the links between solid-state structure and properties, and also illustrates the strong synergy between experiment and theory.

8.2 Photoactivated linkage isomerisation

Linkage isomers are coordination complexes where one or more ligands display several distinct binding modes to the metal centers.

Reports of linkage isomerism date at least as far back as the 1900s when the color difference between the yellow and red forms of the Co complex $[Co(NH_3)_5(NO_2)]Cl_2$ was explained by the nitrite (NO_2^-) ligand coordinating to the metal through either N or O (Figure 15a). ^{18}O-labeling experiments showed that the ONO-coordinated isomer was a kinetic product and converted to the more stable NO_2 isomer *via* an intramolecular rearrangement.[200] By using spectroscopic techniques, it was also shown that the isomerisation occurs both in solution and in the solid state.[201] The isomerisation between both forms can also be effected photochemically by irradiating at an appropriate wavelength.[202]

Photoswitchable materials are of interest for a number of applications. The photoexcitation in $[Nd(dmf)_4(H_2O)_3(\mu\text{-}CN)Fe(CN)_5]\cdot H_2O$ is accompanied by a change in magnetic

susceptibility, raising the possibility of optically-switched and magnetically-read molecular data storage.[203] Photochromic materials have also been investigated for data storage and have a wide range of other potential uses including as optical switches and photo-controlled catalysts.[204] More recently, a linkage-isomer system was identified where the photoactivated isomerisation induces rotation of a neighboring benzene ring, thus acting as a transducer between solar energy and mechanical motion.[205]

In the solid state, linkage isomerism results in the movement of whole atoms and typically proceeds without loss of crystallinity, allowing the process to be followed with single-crystal X-ray diffraction. Pioneering "photocrystallography" experiments conducted by Coppens *et al.*,[206] in which single crystals were irradiated *in situ* on the diffractometer and the fractional occupations of the ground and metastable isomer(s) refined from the data, conclusively identified three NO binding modes in sodium nitroprusside $Na_2[Fe(CN)_5(NO)]{\cdot}2H_2O$ (SNP; Figure 15b), and the technique has remained of huge importance to the field since then.[207]

Following the seminal work on SNP, several families of organometallic linkage isomers have been identified and characterized, including systems based on nitrite (NO_2^-),[208–210] sulphur dioxide (SO_2; Figure 15c)[205,211,212] and (di)nitrogen (N_2) ligands.[213] Key material parameters are the speed and extent of the photo-conversion and the thermal stability of the metastable state. Earlier studies focused on maximizing photo-conversion, and in 2009 Warren *et al.* demonstrated 100% conversion in [Ni(dppe)(NO_2)Cl)] (dppe = 1,2-bis(diphenylphosphino)ethane) by using the bulky dppe ligand to engineer a large "reaction cavity" to facilitate the isomerisation.[214] More recently, attention has turned to increasing the so-called metastable limit — the temperature above which spontaneous decay of the metastable state can be observed — towards room temperature, with a view to eventual device applications, and a limit of 240 K was recently achieved with [Pd(Bu_4dien)(NO_2)]BPh_4 (Bu_4dien = N,N,N′,N′-tetrabutyldiethylenetriamine, BPh_4 = tetraphenylborate).[215]

Computational modeling is regularly employed alongside experimental measurements on linkage isomers to study the energetics of the isomerisation and to identify possible conversion

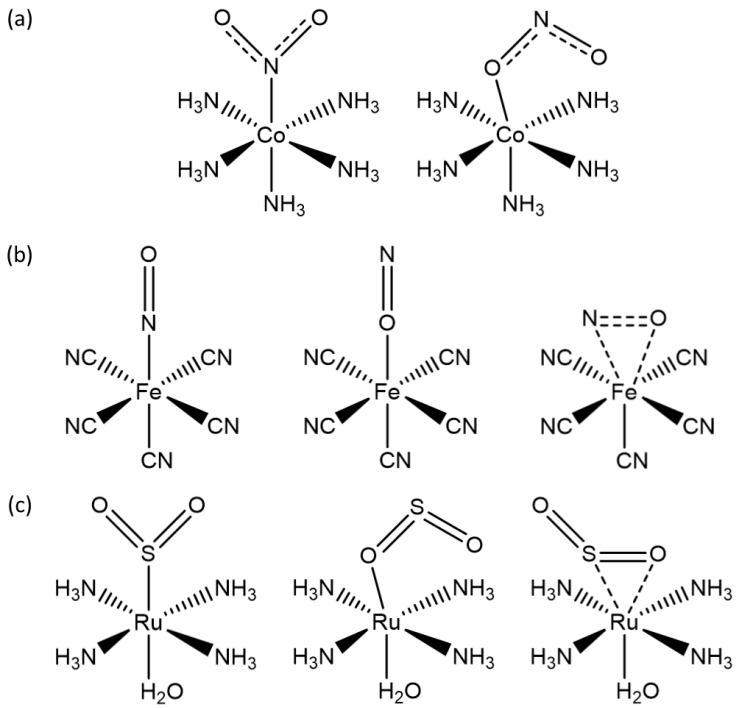

Figure 15: Examples of linkage-isomer complexes: (a) NO_2 binding modes in $[Co(NH_3)5(NO_2)]^{2+}$; (b) NO binding modes in $[Fe(CN)_5(NO)]^{2-}$ (nitroprusside); and (c) SO_2 binding modes in $[Ru(NH_3)_4(H_2O)(SO_2)]^{2+}$.

pathways and the associated activation energies.[216,217] A recent study on the [Ni(Et_4dien)(η^2-O,ON)(η^1-NO_2)] linkage-isomer complex used time-dependent density-functional theory (TD-DFT) to examine the photochemical conversion between the ground-state NO_2 and metastable-state ONO binding modes.[216] Redistribution of electron density, due to low-lying metal-to-ligand charge-transfer (MLCT) absorption bands, was found to populate antibonding states and reduce the activation barrier to isomerisation. However, as this particular system also shows thermal isomerisation, which was studied using molecular-dynamics simulations,[216] it is also possible that strong vibronic coupling could promote isomerisation by leaving the system in a vibrational "hot" ground state after de-excitation.

Another area where modeling plays an important role is in studying the isomerisation kinetics. Improvements in X-ray sources and detector technology, particularly at synchrotron facilities, have made it feasible to probe the kinetics of the forward (excitation) and reverse (decay) isomerisation processes with time-resolved X-ray diffraction experiments.[207,218] At low temperatures, the metastable isomer is sufficiently long lived that the sample can be cooled down, photo-excited, warmed up and the decay monitored by collecting sequential single-crystal datasets. A similar procedure can be followed for the ground $\rightarrow$ metastable excitation by interspersing light pulses with data collections at temperatures below the metastable limit. At higher temperatures, the balance of excitation and decay leads to a temperature-dependent steady-state population of the metastable isomer, which can be probed by collecting structures while the sample is under continuous illumination. One could also envisage using synchrotron radiation and fast detectors to perform pump-probe X-ray diffraction experiments, although such experiments have so far been confined to measurements of carefully-chosen Bragg reflections rather than complete datasets.[219]

It is typically found that the population of the metastable state $\alpha_{MS}(t)$ during excitation and decay follows Johnson-Mehl-Avrami-Kolmogorov (JMAK) kinetics:

$$\alpha_{MS} = \alpha_{MS}^{\infty} + \left(\alpha_{MS}^{0} - \alpha_{MS}^{\infty}\right) e^{-kt^n} \tag{9}$$

where α_{MS}^{0} and α_{MS}^{∞} are the initial and final MS populations, respectively, k is the rate constant, and n is the Avrami exponent, which is usually close to integer and related to the dimensionality of the growth of the incipient phase by $D = 1-n$ (i.e., $n = 4$ implies 3D growth and $n = 1$ implies homogeneous conversion throughout the bulk with no cooperativity). It is further found that the decay rate is strongly temperature dependent and follows an Arrhenius law with an activation energy E_A, i.e.:

$$k(T) = Ae^{-\frac{E_A}{RT}} \tag{10}$$

where R is the gas constant and the prefactor A relates to the attempt frequency and is assumed to be temperature independent. By combining the JMAK and Arrhenius equations and assuming a 100% initial population of the metastable isomer (i.e., $\alpha_{MS}^{0} = 1$), an analytical expression for the half-life of the decay can be derived as:[218]

$$t_{0.5}(T) = \left[-\frac{1}{A}\ln(\frac{1}{2})e^{\frac{E_A}{RT}}\right]^{\frac{1}{n}} \tag{11}$$

Taking the $[Pd(Bu_4dien)NO_2]BPh_4$ linkage isomer studied in Ref. 218 as an example, the measured activation energy of 60 kJ mol^{-1}, corresponds to half lives from 10^5 s ($>$ 24 hrs) to 1 s over a temperature range of 200 to 300 K. The predictable variation of the metastable-state lifetime with temperature makes these systems very well suited to the fundamental development of time-resolved spectroscopic methods that could then be adapted to other photoactive systems of interest such as photocatalysts.

8.3 Outlook

In this section, two classes of responsive materials have been discussed. Pt-pincer complexes show solid-state vapochromic responses to small-molecule analytes, and the solvent selectivity and color change can be controlled directly through the chemistry of the molecule and indirectly through the crystal packing in the solid state. Photoactivated linkage isomerism

is a canonical example of a single-crystal-to-single-crystal phase transition, and the ability to study the isomerisation using single-crystal X-ray diffraction and to control the lifetime of the metastable state with temperature provides the scope to develop novel time-resolved techniques for studying photochemical reactions in molecular solids.

Both examples demonstrate the utility of modeling at all stages of the material "lifecycle", from selecting an initial synthetic target to providing complementary insight to spectroscopic measurements and suggesting material modifications to optimize physical properties towards the intended application. Atomistic simulations using, e.g., electronic-structure methods such as DFT are particularly powerful and are becoming increasingly commonplace, but more "phenomenological" modeling, such as using empirical rate laws fitted to experimental data to predict kinetics, remains an important complementary technique. As first-principles modeling and advanced spectroscopic techniques continue to become more widely available, tighter integration between theory and experiment will be a key factor in establishing new insights that will ultimately yield novel functional molecular materials with tunable properties to meet contemporary challenges.

9 Materials for nuclear reactors

The first electricity-generating nuclear power plant, with an experimental breeder reactor, began operation in 1951 in USA; since then, a lot of effort have been spent towards improved efficiency and safety.[220–223] Most common challenges are the effects of radiation and temperature on the structural materials which are key elements for containment of nuclear fuel and the fission products. During fission, α particles are emitted becoming helium particles by capturing electrons from the surrounding structural materials. Initially He radiation damage appears in the form of local defects; however, these defects quickly agglomerate and interact with the underlying structure causing undesired effects such as blistering.[224–226] Helium atoms can rapidly diffuse through interstitial sites even below the room tempera-

ture.[227] Usually, they form bubbles which cause embrittlement within the material, resulting in degradation of its mechanical, thermal and electronic properties. Several classes of structural materials have been proposed[228] to guarantee the successful operation, maintenance and long life span of the reactor; nonetheless, defect induced blistering and helium embrittlement are still issues to be handled.

9.1 Nanoscale Metallic Multilayer Composites

It has been known for decades that surfaces, grain boundaries and interphase boundaries act as sinks for radiation-induced point defects and traps for He.[229] However, the detailed mechanisms at the level of the atomic structure of an interface, that enable a nanocomposite to be stable under high irradiation flux or high concentration of He, are only just started to be clarified through studies of model systems where ion irradiation is integrated with atomistic modeling.[230] The emergence of new concepts using nanoscience in the design of bulk structural materials shows promise to provide the breakthroughs needed for future nuclear energy systems. In particular, the design and control of interfaces and complex defect structures could lead to self-healing materials with extremely low sensitivity to radiation damage. Such concept has the potential to make radiation damage a much less critical factor in technical design and opens new horizons for nuclear energy sector.

Nanoscale metallic multilayer composites (NMMC), which contain many interfaces between different type of metals, represent a step-change in the design of nuclear materials, with the potential to overcome limitations of existing technologies. Recently, a promising heterophase interface design approach was proposed, where interfaces could be produced to act as efficient sinks for irradiation-induced vacancy-interstitial (Frenkel) pairs, leading to their enhanced recombination and thus restoring part of the material to its undamaged state.[231] Such concept has been illustrated using a Cu/Nb nanolayered system.[230,232–240]

A Cu/Nb multilayer composite is produced using magnetron sputtering technique and is shown in Figure 16a and Figure 16b as an example. The combination of such interface

with a multilaminate material design concept[230,231] has been shown to produce nanostructured materials exhibiting ultra-high strengths (hardness around 5-7 GPa for Cu/Nb) and enhanced radiation damage tolerance.[231,241–243] The unique ability of Cu/Nb interfaces to trap and recombine Frenkel pairs created during irradiation-induced collision cascades can be traced back to the unusual properties of interfacial point defects in Cu/Nb multilayer composites. One of the most noticeable differences between the behavior of such defects and the ones present in perfect crystalline environments of the corresponding element is the greatly reduced formation energy of interfacial point defects compared to the latter. For example, in Cu/Nb system, vacancy formation energy drops from 1.3 eV to 0.3 eV for Cu and from 2.8 eV to 1.1 eV for Nb,[236,237] while in Zr/Nb system, the same energy drops from 2.0 eV to 0.8 eV for Zr[244] as the vacancy migrates to the interface. Vacancies and interstitials that migrate to the Cu/Nb interfaces are effectively trapped there and undergo accelerated recombination due to the enhanced diffusivity and effective size of interfacial point defects.[231,232,239,240,245,246]

Unlike vacancies and interstitials, helium atoms cannot be annihilated via recombination, thus remaining as impurities within the material. Two prospective interfaces are mostly studied including irradiation testing: Cu/Nb[246–252] and Cu/W[253–256] both experimentally and computationally. In copper-based systems, relevant mechanisms governing the He dynamics seem to be identified,[229] and the total amount of He atoms that can be trapped at the interface is obtainable by considering two key quantities: the misfit dislocation intersections (MDIs) density, which depends on geometrical and chemical parameters and finally identify the availability of nucleation sites, and the maximum number of He atoms that can be accommodated into a cavity preventing a "platelet-to-bubble" transition to occur. Furthermore, these systems also show promising properties in the sequestration and arrest of He bubble growth.[247,252] Structural analyses on implanted samples showed interfaces decorated by He bubbles thus underlying the key role also played by Cu/X interfaces. However, Cu exhibits significantly lower energy barrier with respect to X for vacancy formation (0.5 eV

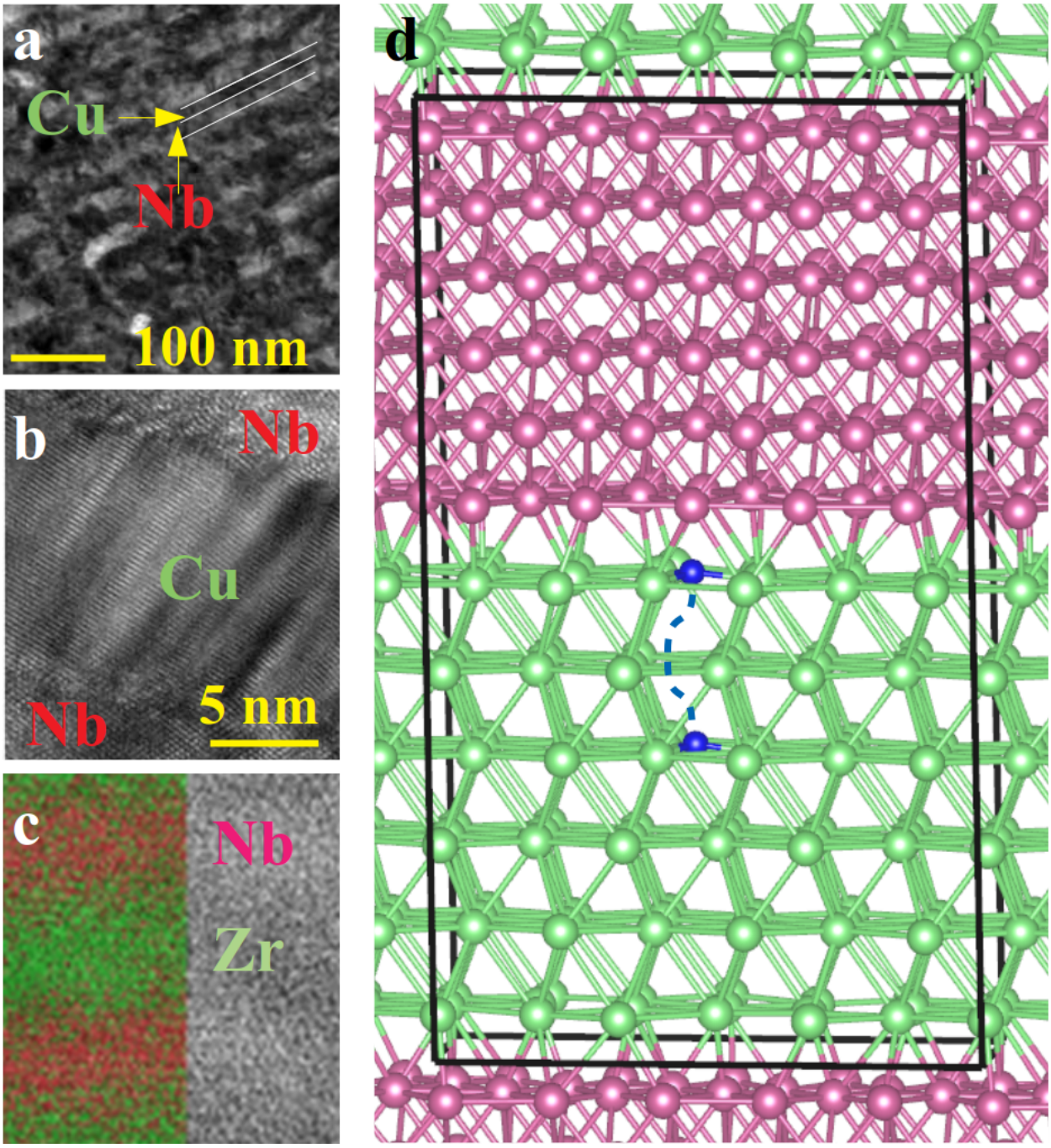

Figure 16: Various NMMCs produced using magnetron sputtering method (a) Cu/Nb, (b) Cu/Nb zoomed, (c) Zr/Nb systems. (d) The unit cell used in DFT calculations to model the system in (c): pink, green and blue spheres represent Nb, Zr and He atoms respectively. The blue line represents the migration path of He atom (from right to left) towards the interface.

for Cu and 2.18 eV for W at the interface) and migration (vacancy migration barrier of 1.07 eV inside Cu and 1.79 eV inside W) in Cu/W multilayer system, and self-diffusion barrier (0.7 eV/atom for Cu and 1.2 eV/atom for Nb) in Cu/Nb multilayer system.[253,257] In combination with lower Cu homologous temperature, He bubbles formation occurs exclusively in Cu layers.[254] The unbalanced He bubbles distribution between constituent elements is accompanied by development of complex residual stress distributions in W layers and leads to the degradation of mechanical and functional properties already at ambient temperature. Moreover, in generation IV reactors, temperatures greater that 500 ℃ are expected; unfortunately, this strongly limits the use of copper, since temperature-driven recrystallization and crystal growth already occur at about 300 ℃.[258–260] On top of that, at high temperatures, functional properties (hardness, toughness) of Cu/Nb[261] and Cu/W[262] films drop significantly. Due to the issues mentioned above, although Cu/X is profoundly studied as a model material to understand the role of interfaces in radiation environments, its employment in nuclear industry would be rather limited. This appealed for the selection of other materials with suitable thermal and structural stability. It was evident that Cu is a weak point in the interface design; substitution of Cu by Zr could indeed represent the key solution allowing for a prompt introduction of this class of materials in the future of nuclear industry. Among various systems, the Zr/Nb one has been identified[244,254,263–266] as appropriate from mechanical and thermal stability point of view. Zr/Nb system outperforms mechanical properties of Cu/Nb and W/Cu above 300 ℃; indeed Zr-Nb alloys are currently used in CANDU-type reactor.[267] Zr/Nb interfaces have recently been prepared[254,263–266] in a multilayer architecture using magnetron sputtering method (Figure 16c). The results indicate that Zr/Nb system retains high hardness (reaching as high as 13 GPa) even at 400 ℃[263,264] and show remarkable resistance to γ[265] and heavy Si ion[266] radiation. High interface-to-volume ratio due to small crystallites is expected to have exceptional positive effects on the self-healing properties of the materials subjected to radiation damage.

DFT calculations[244] indicate Zr/Nb multilayer systems retain most of the mechanical

properties of their bulk forms, thus becoming promising candidates for nuclear applications. The electronic structure calculations further reveal that He atom prefers to sit at the low electron density region within the material. He atom is either trapped by a vacancy or is drawn to the Zr side of the interface, due to the charge transfer at the interface which makes Zr side positively charged. The unit cell for this calculation and the migration path for He towards the interface is shown in Figure 16d. Similarly, it is energetically favorable when the vacancy within the material is in the Zr side of the interface, so as to minimize the stress that is generated by the presence of the vacancy in the first place. Therefore, both He atom and the vacancy are drawn to the Zr side of the interface although due to different reasons. To sum up, evolution of nuclear technology allows us today to harvest energy from nuclear reactions by means of nuclear power stations in a controlled and safe way. However, there are still problems related to the structural components of the reactors limiting the harvested energy and life span of the reactors themselves. Although many of these issues can be resolved through the use of proper materials, defect induced blistering and He embrittlement have yet to be worked out. Recently proposed NMMCs can be a solution to these final problems.[230] So far, Zr/Nb multilayer composites appear to be a great candidate but still further research is required.

9.2 Outlook

Several possible NMMCs can be designed. For example, Mg/Ti (hcp/hcp) interface, similar to Zr/Nb, could be an interesting candidate owing to the mutual immiscibility of the constituent elements, which may lead to high thermal and compositional stability.[268] The lattice mismatch and consequently misfit strain ($\tilde{8}.6\%$) between Mg and Ti would give birth to a misfit dislocation network well acting as a sink for helium atoms. Moreover, the high mechanical stiffness-to-weight ratio makes this combination also particularly suitable where high specific strength is required.[269] Even if the He atoms are attracted to the interface, a way to prevent their accumulation hence bubble formation must be identified.

It has been shown[244] that He atoms follow the lower electron density regions inside the material. Therefore, by manipulating the charge density within the material, it might be possible to lead He atoms out of the system, thus taking He embrittlement part of the problem totally out of the picture.

10 Novel mechanisms for improved oxide thermoelectrics explored from first principles

Transition metal oxides where electronic correlations play an important role[270,271] are an attractive materials class for thermoelectric applications. They exhibit a substantial chemical and thermal stability and are generally environmentally friendly. Considerable experimental and computational[272,273] effort aims at finding oxide thermoelectrics with improved performance, usually by maximizing the electronic contribution to the thermoelectric figure of merit $ZT = \sigma S^2 T/(\kappa_{\rm el} + \kappa_{\rm ph})$, namely, the electrical conductivity σ and the Seebeck coefficient S at temperature T. At the same time, electronic and lattice contributions to the thermal conductivity, $\kappa_{\rm el}$ and $\kappa_{\rm ph}$, need to be as small as possible.

In bulk materials, n- and p-type thermoelectric response is commonly attained by doping,[274–276] a prominent example being La-doped $SrTiO_3$ (STO) single crystals,[277] or epitaxial films.[278,279] A different route is to utilize the impact of epitaxial strain on the electronic structure. Specifically, the delafossite $PtCoO_2$ exhibits a remarkable change in thermopower when varying from tensile to compressive strain.[280] This is related to a reconstruction of the Fermi surface topology, i.e., a strain-induced shift of additional bands through the Fermi energy. An alternative strategy is to exploit heterostructuring and dimensional confinement,[281,282] a concept that is not only applied to oxides,[283–291] but also used in Heusler/oxide magnetic tunnel junctions[292] or Heusler/metal hybrid systems.[293–295] This is based on the recent ability to grow transition metal oxide superlattices (SLs) with atomic precision.[296–298]

Next, three different approaches to design thermoelectric properties are described, which

go beyond the initial proposal by Hicks and Dresselhaus.[281] Such approaches rely on the insight that can be obtained from atomistic simulations within the framework of DFT combined with Boltzmann transport theory. The focus is on the correlated metal $LaNiO_3$ (LNO) heterostructured with the band insulators STO[289] or $LaAlO_3$ (LAO)[290,291] materials, that can be grown epitaxially "cube-on-cube" in their natural perovskite ABO_3 structure,[299–303] as well as in the form of Ruddlesden-Popper/perovskite hybrid structures.[298,304,305] While LNO and STO result in polar interfaces, the LNO/LAO materials combination is nonpolar but, nonetheless, shows intriguing properties concerning confinement and strain. A discussion and an outlook on the influence of the phonon system close this section.

10.1 Impact of the interface polarity on the thermoelectric response

An efficient thermoelectric energy conversion requires both n- and p-type materials that are structurally and electronically compatible. It has been recently shown that this can be realized in oxide SLs by exploiting the interface polarity.[289] In particular, the mechanisms of electronic reconstruction at polar oxide interfaces[306,307] have attracted significant interest in the past decade.

In LNO/STO(001) SLs, variation of the stacking sequence at the interface generates different types of SLs, particularly an electron-doped one with n-type $(LaO)^+/(TiO_2)^0$ interfaces (IF-n), or a hole-doped one with $(NiO_2)^-/(SrO)^0$ interfaces (IF-p). The resulting stoichiometries for SLs with 3 layers of each material are $(LNO)_{3.5}/(STO)_{2.5}$ for the n-type SL and $(LNO)_{2.5}/(STO)_{3.5}$ for the p-type SL. Both structures are displayed in Figure 17a. DFT+U calculations show that the charge mismatch at the interfaces is exclusively accommodated in the nickelate region by shifting upward/downward the Fermi level for the SL with n-/p-type interfaces, while STO is rather a spectator. This is in sharp contrast to the much studied LAO/STO(001) system, where the Ti 3d states are involved.[307,308] Transport calculations within Boltzmann theory show that the distinct band alignment between LNO and STO in the two stacking sequences leads to either n- or p-type thermoelectric response of

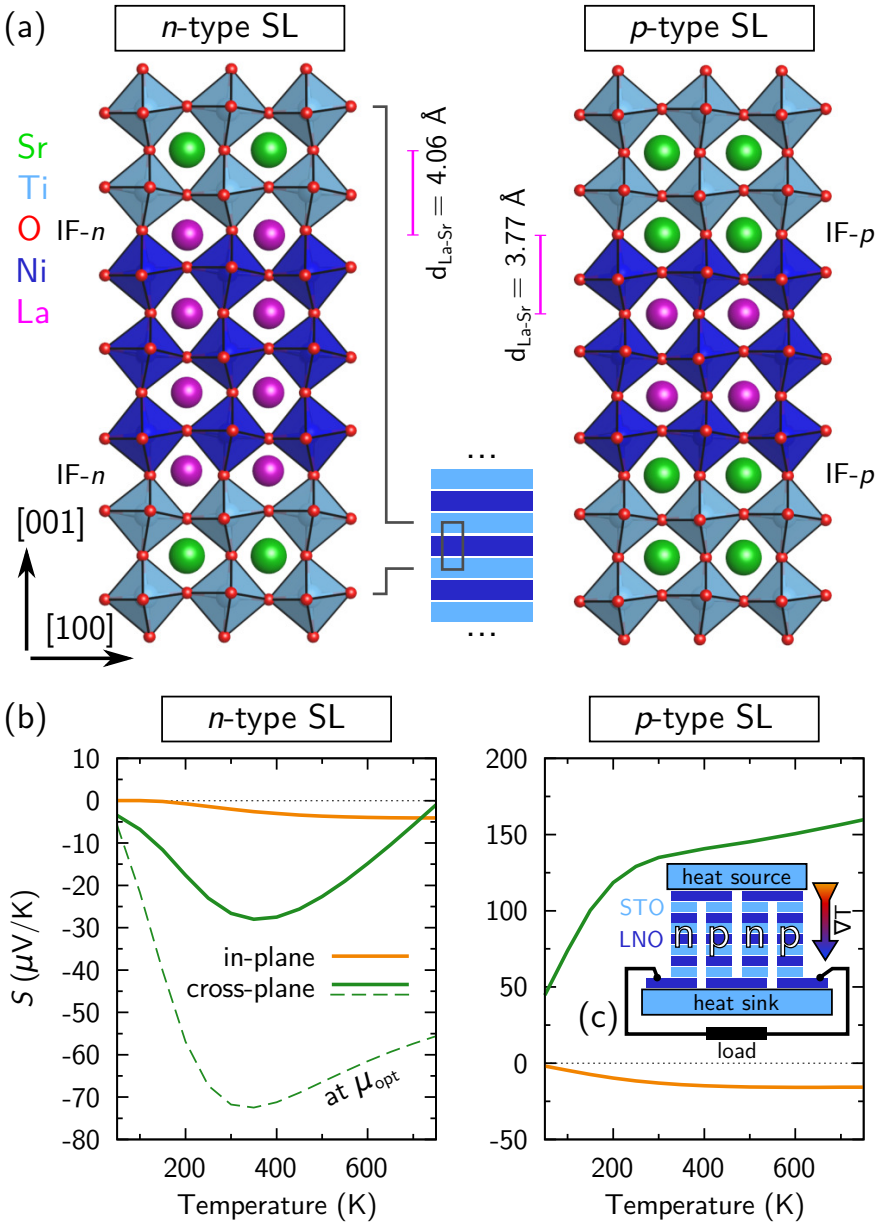

Figure 17: (a) Side views of the optimized geometry of LNO/STO(001) SLs with interfaces of opposite polarity (IF-n or IF-p) grown on STO. The La-Sr distance $d_{\text{La-Sr}}$ across the interface acts as a fingerprint of the interface type, being elongated for an electron-doped SL and compressed for a hole-doped SL. In both cases, significant octahedral tilts are induced in the STO part. (b) Thermoelectric response of the SLs. The sign of the cross-plane Seebeck coefficient S is consistent with the polarity of the interfaces (negative/positive for n-/p-type). Additional doping (μ_{opt}, see Ref. 289) enhances the performance. (c) Illustration of a thermoelectric generator based on n- and p-type SL legs composed of the same materials combination. (Adapted from Ref. 289.)

the SL in cross-plane direction (Figure 17b). While in the n-type case the electronic transport involves tunneling through the insulating STO region, the particular position of the STO valence band maximum directly below the Fermi level in the p-type SL strongly boosts the thermoelectric response with a Seebeck coefficient of +135 μV/K at room temperature.

We note that a related concept was proposed by Botana *et al.*[309] for CrN/MgO(111) SLs, which however differs in the strong charge mismatch at the interface (formal charge of the layers at the interface: $2^-/3^+$) that may drive the formation of compensating defects, and the fact that the voltage builds up perpendicular to the thermal gradient. Since polar interfaces occur also in many other systems, for instance in group IV/III-V semiconductor heterostructures such as Ge/GaAs,[310] the outlined concept is not restricted to oxides, but may be relevant for other classes of materials.

10.2 Epitaxial strain as control parameter in a system with confinement-induced metal-to-insulator transition

In doped bulk materials or epitaxial films,[277–279] the carrier concentration is used as control parameter to maximize the power factor $\mathrm{PF} = \sigma S^2$. The highest power factor is usually found in the intermediate regime between semiconducting and metallic behavior, which provides the best tradeoff between Seebeck coefficient (which reflects the transmission asymmetry near the chemical potential μ and thus benefits from the band gap in a semiconductor) and electrical conductivity (which is largest in a metal). In the following, it is shown that epitaxial strain can take on a similar role in artificial transition metal oxides.

Nonpolar LNO/LAO(001) SLs are an intensely studied system.[299,303,311,312] In the ultrathin limit, epitaxial strain together with quantum confinement drive a metal-to-insulator transition in $(\mathrm{LNO})_1/(\mathrm{LAO})_1(001)$ SLs (Figure 18a).[290,311] The emerging band gap for tensile strain (~ 0.3 eV for a_{STO}) leads to a strong enhancement of the thermoelectric response, as one can infer from Figure 18b. A particularly interesting aspect of this system is that the short-period SL design in the [001] direction (cross-plane) considerably improves the

in-plane thermoelectric performance. Consequently, the in-plane power factor outperforms the cross-plane one due to the much higher in-plane conductivity. Comparing the conductivity obtained from DFT+U for $(LNO)_3/(LAO)_3(001)$ SLs with experiment,[303] the relaxation time at room temperature was estimated to be $\tau \approx 4$ fs. This results in in- and cross-plane Seebeck coefficients of ± 600 μV/K and an in-plane power factor of 11 $\mu W/K^2cm$ around room temperature, making the system comparable to some of the best performing oxide systems such as La-doped STO[277–279] or layered cobaltates.[313] Further increase of the epitaxial strain (e.g., as induced by a $DyScO_3$ substrate) does not lead to an additional enhancement, but on the contrary reduces the power factor again due to a decrease of the in-plane conductivity at the edges of the further increased band gap.[290]

Increasing the thickness of both constituents to 3 layers each in $(LNO)_3/(LAO)_3(001)$ SLs deteriorates the thermoelectric performance due to the two-dimensional metallic nature of the LNO region and the too thick large-band-gap LAO spacer layer, irrespective of the epitaxial strain. This underlines the key role of quantum confinement.

It is then concluded that a significant enhancement of the thermoelectric properties can be obtained in oxide SLs such as $(LNO)_1/(LAO)_1(001)$ at the verge of a metal-to-insulator transition.

10.3 Transport resonances tuned by strain engineering of the orbital polarization

Above it has been discussed that n- and p-type thermoelectric response can be induced in polar oxide SLs by a selective design of the stacking sequence at the polar interfaces.[289] In the following, it is shown that the same goal can be achieved in nonpolar SLs by strain engineering of the orbital polarization.[291]

Designing the thermoelectric response of a system necessitates quantum control over the asymmetry of its spectral transmission function $\mathcal{T}$ around the Fermi energy.[292,314] Mathematically, it has been shown decades ago that transport resonances are attractive for ther-

moelectric applications.[315] Nevertheless, the explicit use of these resonances has been limited to model studies.[316,317] In order to pursue this route, *i*) a transmission function $\mathcal{T}$ exhibiting sharp resonances has to be designed, and *ii*) a mechanism that allows for a precise tuning of the transport resonances with respect to the Fermi energy is required.

This concept has been demonstrated on the basis of first-principles calculations in $(LNO)_3/(LAO)_1(001)$ SLs,[291] which are displayed in Figure 19a. The confinement of three layers of LNO separated by a single LAO spacer layer induces the formation of distinct Ni $3d_{x^2-y^2}$- and $3d_{z^2}$-derived quantum well (QW) states, while at the same time permitting cross-plane electronic transport through the single LAO spacer layer. This leads to the emergence of sharp cross-plane $3d_{z^2}$-derived transport resonances (Figure 19b). Epitaxial strain strongly impacts the orbital polarization in this system and thus the relative energy and occupation of the $3d_{x^2-y^2}$- and $3d_{z^2}$-derived QW states (Figure 19a). Due to this charge redistribution mechanism, the $3d_{z^2}$-derived transport resonances can be shifted with high precision relative to the Fermi energy. Thereby, considerable *n*- and *p*-type thermoelectric response (~ -60 to $+100$ μV/K around room temperature) can be obtained in one and the same materials combination by moderately varying the control parameter epitaxial strain between -1.5 and -2.8 % (Figure 19c). It has been shown that this concept is robust with respect to the formation of oxygen vacancies.[291]

This work exemplifies how the thermoelectric properties of oxide heterostructures can be controlled and optimized by varying layer thickness, quantum confinement, and epitaxial strain. Moreover, it manifests an application for the control of orbital polarization, which is intensively pursued in artificial transition metal oxides.[311,318–321]

10.4 Outlook: The role of phonons

The focus of most theoretical studies lies on improving the electronic contribution to the thermoelectric figure of merit ZT, i.e., optimizing conductivity σ and Seebeck coefficient S. On the other hand, the impact of phonons, which affect *i*) the relaxation time τ and *ii*) the

lattice contribution to the thermal conductivity κ_{ph}, is often neglected. Both quantities can be obtained from first principles: The relaxation times have been calculated very recently for bulk Si[322] and for elemental noble metals,[323] employing a combination of DFT and many-body perturbation theory. Due to the high numerical demand, this approach has not been applied so far to more complex systems such as the oxide SLs discussed here. The thermal transport, on the other hand, has been calculated recently for bulk MgO by a complete solution of the linearized Boltzmann transport equation.[324] Larger systems such as Fe/MgO/Fe(001) magnetic tunnel junctions have been treated within a Green's function framework.[325]

Exploiting interface scattering of phonons by heterostructuring is a viable strategy to reduce the lattice thermal conductivity.[282,326–328] In SLs, the periodicity has a strong impact, and it has been demonstrated experimentally that at the crossover point between incoherent to coherent phonon scattering in oxide SLs the lattice thermal conductivity exhibits a minimum.[329] However, the parameters corresponding to this optimal point have to be determined in each specific case. High crystalline quality is beneficial for electronic properties, but simultaneously can lead to coherent phonon heat conduction, and it has been shown for GaAs/AlAs(001) SLs that the thermal conductivity can even increase with the number of layer repeats.[330] In short-period SLs the thermal conductivity can exceed that of the constituent materials, as has been demonstrated for Si/Ge(001) SLs.[331] This highlights that further effort is required to explore the influence of heterostructuring on the phonon system from first principles.

11 Polar, ferroelectric and multiferroic metals: three case studies

Here, case studies of polar,[332] ferroelectric,[333] and multiferroic[334] metals are discussed, where polar symmetry — and in some cases, polarization itself, are actually realized in metals.

The idea of ferroelectric metals harkens back to a suggestion by Anderson and Blount[335] that some metals may possess, or acquire, polar symmetry, i.e., one compatible with the existence of electric polarization. Whether a polarization, and attendant phenomena, would actually materialize as a consequence was left unspecified, and this is one of the issues being investigated, mostly theoretically so far.

It is appropriate to have a checklist for the definition of a ferroelectric metal: it should

i) be a metal

ii) have polar symmetry

i) have a measurable or computable zero-field polarization P

iv) optionally support a polarization-induced depolarizing electric field when cast in finite form (e.g. thin film), which would imply the actual switchability of P

The last requirement is optional because, even bona-fide, ferroelectrics often do not satisfy it: a large polarization in a film causes a large depolarizing field, whose destroys the polar distortion and, ultimately, the polarization itself.

11.1 Metascreening in metalized ferroelectrics

Polar metals should satisfy the *i*) and *ii*) requirements. A further distinction can be made between metals, that are or can be rendered polar, and polar insulators which are made robustly metallic. Among the former, let us briefly mention $LiOsO_3$ and related composite systems, which stands out in both experiment and theory,[336–338] and the general guidelines laid out for their search.[339]

In this section, the mechanism that causes metalized ferroelectrics to conserve polar distortions, i.e., to become polar metals, is discussed. Figure 20 shows the amplitude of the polar distortion as function of free charge density of either sign, normalized to the value at zero added charge, for a limited selection of the materials discussed in Ref. 332. Evidently,

all materials exhibit stable polar distortions as a function of charge density of both signs, except three of them whose distortion dies out at high n-type density.

$BaTiO_3$ (BTO) is an interesting case as it allows to monitor the transition from polar to non-polar phase. As detailed in Ref. 332, in an 80 Å-long supercell of cubic BTO perturbed by a dipolar displacement of a plane of Ti atoms, it is found that free charge screens out long-range interactions over a typical length scale of less than 10 Å from the perturbation. Doping produces a concurrent short-range effect (referred as *metascreening*) that enhances the distorting forces on the atoms in the immediate vicinity of the perturbation; specifically, a lattice distortion near the perturbation accommodates the screening electrons or holes, and it is essentially indistinguishable from the original polar distortion in the undoped case.

To prove that this effect is not a consequence of incomplete screening, but indeed due to short-range effects, one can calculate the stiffness constant for the soft ferroelectric mode $\mathcal{S} = \mathbf{s}^T \cdot \mathbf{F} \cdot \mathbf{s}$, with $\mathbf{F}$ the force constant matrix calculated at the Γ point and $\mathbf{s}$ the soft-mode eigenvector. Another stiffness $\mathcal{S}_{sr}$ is calculated, just the same way as $\mathcal{S}$, except that the force constants between neighboring Ti atoms are always those of the undoped case, independently of the doping level: the shortest-range interactions are thus frozen into the undoped configuration. As Figure 21 reports, $\mathcal{S}$ is negative for all free carrier densities up to about $+0.05$ $|e|$/formula unit, predicting a polar distortion in accordance with Figure 20; on the other hand, $\mathcal{S}_{sr}$ is always positive, corresponding to stability against polar distortion, except in the undoped case. This shows directly that the metascreening short-range forces are the key enabler of the survival of the distortion in the doped system.

11.2 A ferroelectric metal

A proper ferroelectric metal obeying all the requirements in the checklist has been found[333] in a different, and so far unique in this respect, class of materials: the layered perovskites of the $A_nX_nO_{3n+2}$ class, which features prominently $n = 4$ ferroelectrics and multiferroics such as $La_2Ti_2O_7$ and $La_2Mn_2O_7$.[340] The $n = 5$ class is trivially metallic from electron counting with

a density of around 3×10^{21} cm^{-3}, but the ferroelectric mechanism active in $n = 4$ materials[341] does not apply. Luckily, it turns out that $Bi_5Ti_5O_{17}$ (BTO-5517 below) has polar symmetry $Pm2_1n$, with polar axis equal to the stacking direction b, due to local chemical Bi-O dipoles (analogous to $BiFeO_3$) and, thus, BTO-5517 is a polar metal in agreement with points *i*) and *ii*).

The computability of zero-field polarization P, point *iii*), is potentially contentious because the Berry phase polarization[342] is ill-defined in its original form if the number of occupied bands change along the k integration direction (parallel to P itself), as expected in metallic conduction bands. The conduction bands in BTO-5517, however, are very flat along P (i.e., $k_\parallel$) direction: thus, for all numerical intents and purposes, the number of occupied bands will not change along $k_\parallel$, and a convergent P will be obtained as usual on a finite grid made up of string parallel to the P direction. To cure the unavoidable occasional crossings (the bands are not perfectly flat), P is calculated as the 2D average of a renormalized phase subject to a charge conservation constraint.[333] Physically, this corresponds to Fermi surface sections that are quasi-1-D lines when projected on the $k_\perp$ plane (i.e., with zero measure in that plane, perpendicular to the integration direction) as is the case in BTO-5517, or to conduction charge that is strongly localized within the blocks and not very mobile. The latter view suggests to also estimate the polarization simply as the dipole of a single block. The modified Berry approach and the block-dipole approximation give similar values for the conduction band, around 5 μC/m^2; summing up the dominant valence and ionic contributions, a large total $P = 35$ μC/m^2 is obtained, in the same league as ferroelectrics such as $BaTiO_3$.

To complete point *iii*) and address point *iv*) in the checklist, it is here demonstrated that the material can support a depolarizing field (i.e., the polarization can be switched). To this end, a BTO-5517 layer is cladded with the insulator $Ba_2Zr_2O_7$; this configuration is an open circuit with no current flow, which will instead occur if BTO-5517 is contacted directly. In Figure 22, showing the electrostatic potential difference of the polar and non-polar superlat-

tice, the metallic layer screens only partially the polarization-induced depolarizing field. The polarization will thus switch, as in ferroelectrics, upon application of a field exceeding the depolarizing field (i.e., the finite screening ability of the layer). The free-charge response in the finite system is limited by the small amount and localization of the mobile charges, and the screening ends up being incomplete; the multilayer is in effect a dielectric medium with finite low-frequency, low-wavevector dielectric function in agreement with recent results on sub-nm metal-air multilayers.[343]

Single-domain BTO-5517, not only polarized but also sustaining a polarization-generated depolarizing field, contradicts the usual assumption that a large polarization cannot survive its own depolarization field in a thin film. In this respect, BTO-5517 is unlike other ferroelectrics precisely because of the self-screening mechanism that cancels in part the depolarizing field, while not destroying the chemically-driven polar distortion. In this context, BTO-5517 behaves as a limiting case of hyper-ferroelectric,[344] and might be dubbed a self-screened hyper-ferroelectric metal.

11.3 A three-order-parameter multiferroic metal

Thinking along the same lines as for BTO-5517, a natural extension is to look[334] for possible multiferroicity in $Bi_5Mn_5O_{17}$ (BMO henceforth), where magnetism is expected due to Mn ions and metallicity. The result is partially analogous to BTO-5517, in that Bi-O dipoles again cause ionic polarization; the symmetry is the same as in BTO-5517, but the polar axis is now c, the (110)-like axis orthogonal to the stacking axis. The total polarization, calculated in the same way as before, is about 5 μC/cm^2; the conduction contribution is minor, around 0.05 μC/cm^2; the Fermi surface is indeed flat and sheet-like, and closely parallel to the c axis.

As hinted above, due to the Mn ions interacting via double exchange, BMO is ferromagnet with average moments 3.2 μ_B. In fact, it is a half-metallic ferromagnet, with a metallic majority spin channel and insulating minority (with a gap of about 3 eV using self-interaction

corrections). Interestingly, the polarization is non-zero in both spin channels, and larger in the majority than the minority spin channel by roughly a 3 to 1 ratio.[345] A definite point of interest in the O-rich layered phase BMO is that, according to the calculations,[334] it is thermodynamically favored over the known $BiMnO_3$ normal perovskite phase in a sizable window of O chemical potential, favoring the synthesis of BMO unlike that of BTO-5517, which has not been achieved yet.

Demonstrating the existence of a depolarizing field in BMO is trickier than in BTO-5517, because there is no natural way of stacking BMO and an insulator along *c*. Eventually, cladding BMO with the n=5 compound $BaLa_4Zr_5O_{17}$ (with a gap of about 2 eV) ended up doing the trick. Again, as in the case of BTO-5517, there is a charge monopole at the metal-insulator interfaces, and a residual field inside both the metal and the insulator. The screened-field energy density is much lower than the stabilization energy of the polar distortion (which is a bit larger that of $BaTiO_3$, suggesting thermal stability up to at least 400 K), so the distortion is not affected by the depolarizing fields. Hence BMO checks all the boxes in the checklist and qualifies as a ferromagnetic ferroelectric metal.

Actually there is more to the story: BMO turns out to also have ferrotoroidic order, i.e. its magnetic symmetry allows for a non-zero toroidal moment $\mathbf{T}$, a polar vector that inverts under time reversal. The symmetry group is the only one such that $\mathbf{T}$, $\mathbf{P}$, and $\mathbf{M}$ are all mutually orthogonal, and since non-collinear magnetic calculations show that the magnetization $\mathbf{M}$ points along *a*, it eventually turns out that $\mathbf{T}\sim\mathbf{P}\times\mathbf{M}$ in this case. Both time reversal *and* inversion breaking are needed for a non-zero $\mathbf{T}$, which implies that $\mathbf{T}$ would be non-zero even if $\mathbf{P}$ were suppressed by electronic screening, as long as the symmetry remains polar. Finally, magnetoelectric coupling also occurs in BMO; it happens to be off-diagonal (i.e. cross-field) and its value seems rather large.

11.4 Outlook

The just discussed work on metalized ferroelectrics, especially layered perovskites, has revealed a wealth of unexpected effects. Among the open issues, the possible existence of energy-degenerate ferroelectric and antiferroelectric states, and the related (probably unusual, if not exotic) properties and dynamics of domain boundaries appear worth addressing, while waiting for experimental endeavor to prove predictions about metallic ferroelectricity in general.

12 Electric Magneto-Optical properties in multi-functional hybrid materials

Hybrid organic-inorganic perovskites (HOIPs) are similar to inorganic perovskites in terms of their ABX_3 topology, although the combination of organic and inorganic components provides for greater compositional flexibility.[346] In common perovskites,[347] A and B are cations, and X is an anion that is coordinated to B. The A atoms are normally larger than the B atoms, and the B cation is six-fold coordinated with the X atoms to form BX_6 octahedron (Figure 23). The resulting octahedra are corner-shared to form a three dimensional framework in which the A site cations are located inside the framework cavities. In addition to their physical properties, many of their functionalities are controllable with external stimuli — for instance, magnetic field, pressure, electric field, and light.

Hybrid organic-inorganic materials have emerging applications as multiferroics, photovoltaics, gas sensors, and transparent conductors.[346] HOIPs have a number of advantages compared to perovskite oxides. First and foremost, the A- and/or X-sites are occupied by organic cations and/or organic linkers, respectively (Figure 23).[348–350] At the same time, molecule-based HOIPs often have overall lower energy scales than their corresponding oxides. Quantum phase transitions — driven by magnetic field, pressure, and electric field, can thus occur at experimentally-realizable conditions and more easily controlled. These mate-

rials are also well-suited for the development of structure-property relations. For instance, the variations of the organic and inorganic components offer wide possibilities to create innovative and promising HOIPs in accordance with the generalized Goldschmidt tolerance factor.[351] This can serve as a guide for the rational design and synthesis of new HOIPs using compositions with desired functionalities and dimensionalities.[351,352] The *metal-organic frameworks* (MOFs) are a particularly interesting class of HOIPs (Figure 23). Here, the metal ions are linked together by organic bridging ligands, e.g. carboxylate ligand ($HCOO^-$).[353] As a result, they have complex hydrogen bonding networks that can be adjusted as a function of temperature. These materials display diverse properties including electrical, magnetic, catalytic, optical properties, multiferroic behavior, i.e., coexistence of electric and magnetic ordering[354–365] and magnetoelectric behavior,[354–365] i.e., the coupling between the two long-range orderings. Like many other quantum materials, the MOFs are tunable in magnetic and electric field.

Another emerging class of HOIPs are *hybrid halide perovskites* based on the semiconductive methyl-ammonium (MA) lead halide $MAPbX_3$, where X=Cl,Br,I.[15,366–372] The replacement of the inorganic cation (A) by an isoelectronic organic moiety such as MA^+ $(CH_3NH_3)^+$ provides a unique way of tuning the chemical bonding and consequently also the optical and electronic response.[373–380]

The hybrid perovskite is a very versatile family of compounds with a large catalog of chemical components for the A and B site.[352] For example, *i*) for the A site: $(NH_2)_2CH^+$, $CH_3NH_3^+$, $NH_2NH_3^+$, $(CH_3)_2NH_2^+$, $CH_3CH_2NH_3^+$, $C_3N_2H_5^+$, $C(NH_2)_3^+$, $(CH_2)_3NH_2^+$, $(CH_3)_3NH^+$, $(CH_3)_4N^+$;[351,352] *ii*) for the B site: Cr^{2+}, Cu^{2+}, Fe^{2+}, Mn^{2+}, Co^{2+}, Ni^{2+};[351,352] and *iii*) for X site: I^-,Br^-,Cl^-, CN^-, $HCOO^-$, N_3^-, $[N(CN)_2]^-$.

Moreover, the possibility to reduce the dimensionality by considering novel hybrid two-dimensional (2D) materials appears an interesting direction to explore. For example, very recently, a novel magnetic 2D hybrid compound has been synthesized based on chromium-chloride-pyrazine, i.e., $CrCl_2(pyrazine)_2$.[381–384] Organic molecules and magnetic metal ions

can be used as molecular building blocks for synthesizing novel types of 2D materials exhibiting both electrical and magnetic properties, possibly cross-coupled to magneto-optical properties. Magnetic hybrid 2D materials are now at their infancy, and there is certainly room for new interesting physics to explore.

12.1 Symmetry breaking and physical properties of materials

12.1.1 Multiferroicity and magnetoelectricity

Breaking of time-reversal (T) and inversion symmetry (I) leads to interesting changes in physical properties of crystals. If both symmetries are broken, the compound may have coexisting magnetic and ferroelectric order (multiferroicity).[385–387] It may happen that the two order parameters, i.e., magnetization (M) and electric polarization (P) are coupled (magnetoelectricity)[385–387] with the possibility to tune the electric polarization by an external magnetic field and, vice versa, to tune the magnetization by an external electric field.[385–387] It is interesting to explore the unique effects of cross-coupling of ferroelectric and magnetic orders, which leads to the aforementioned multifunctional properties, on magneto-optical properties.[388–391]

12.1.2 Magneto-optical Kerr effect: tunable and switching properties

The magneto-optical Kerr effect (MOKE) describes the change of linearly polarized light when reflected from the surface of a magnetic material. The change consists of two parts: a rotation of the polarization plane, the so-called *Kerr rotation* θ_K, and a phase difference between the electric field components perpendicular and parallel to the plane of the incident light, the so-called *Kerr ellipticity* η_K.[392] The Kerr rotation can be exploited to read suitably magnetic stored information by optical means in modern high-density data storage technology[393–396] or to probe the magnetic behavior of two-dimensional systems.[397]

The Kerr effect is described by the Kerr angle ϕ_K, a complex number defined as

$$\phi_K = \theta_k + i\eta_K = \frac{-\sigma_{xy}}{\sigma_{xx}\sqrt{1+\left(\frac{4\pi}{\omega}\right)\sigma_{xx}}} \tag{12}$$

where the complex numbers σ_{xx} and σ_{xy} are the diagonal and the off-diagonal elements of the conductivity tensor, respectively.[398,399] Equation 12 is widely used in literature and is valid only in the polar geometry, for compounds with higher than threefold rotational symmetry.[398,399] The conductivity tensor can be calculated from the electronic structure of the solid, and, therefore, Kerr effect can be evaluated based on density functional theory.[399] In a system possessing inversion symmetry I, linear magneto-optical activity (Kerr effect) arises from breaking time reversal (T), like in a ferromagnet. If the system is anti-ferromagnetically ordered, the material is expected to be magneto-optical inactive. Despite this expectation, a multiferroic MOF has been recently found,[391] with chemical formula $[C(NH_2)_3]M[(HCOO)_3$, where M=Cu^{2+} or Cr^{2+}, exhibiting magneto-optical activity even in its antiferro-magnetic state. This result suggests that a magnetic compound may become magneto-optically active when the combined TI symmetry is broken.

If the system is invariant under T and I symmetry,[400–402] it does not have neither magnetic nor ferroelectric ordering. Breaking of T (gray semicircle) gives rise to magnetic ordering while breaking of I (gray semicircle) is necessary for ferroelectricity. Breaking both T and I is necessary for a system to be multiferroic (MF) and/or magnetoelectric (ME). When breaking the TI symmetry, the compound may be magneto-optical active.[400–403]

Moreover, in MOFs the Kerr angle can be tuned not only by M, as a common belief, but also by the ferroelectric polarization (P).[391] This raises the exciting possibility that the Kerr rotation angle could be controlled by M, P, or both — depending on the circumstances. This is an under-explored avenue for achieving the combination of functional behavior needed for logic and information storage in magnetic materials and nanostructures.

12.1.3 Switching properties of Magneto-optic Kerr Effect

As a proof of principle, a series of Kerr spectra calculations on a MOF compound showing ferroelectric and magnetic ordering have been performed.[391]

Figure 24a shows the variation of the Kerr rotation θ_K as a function of the incident photon energy (E) for different values of the normalized amplitude of the polar atomic distortion (λ). $\lambda = 0$ represents the paraelectric state (centrosymmetric) while $\lambda = \pm 1$ represent two ferroelectric states with opposite electric polarization. The parameter λ smoothly changes from -1 to +1 through zero and it is codified by a color scheme from blue to red through white: by changing λ, θ_K changes continuously and the switching occurs when λ changes sign. Since λ is proportional to P in the material, this leads to the interesting conclusion that *Kerr angle can be tuned by P and switches its sign when switching P*. These results have been derived in the case of a magnetoelectric compound:[391] one would naively expect that this ultimately recovers the standard case of $\theta_K \propto M$ since $P \propto M$. However, as shown below, calculations can be generalized by considering M and P as independent variables:

$$\theta_k = \alpha P + \beta M. \tag{13}$$

θ_K can be expressed as linear function of both P and M as reported in Eq. 13. In Figure 24b, $\theta_K(P, M; E$ =3.8 eV) is shown as a color code. The coordinates have been normalized to P_{max} and M_{max}, respectively. The solid orange line represents the locus of points in (P,M) space having zero Kerr angle. For each point in (P,M) space, a color which corresponds to a well defined value of the Kerr angle is associated. Figure 24b represents the following property by a color code in (P,M) space: $\theta_K(P, M; E) = -\theta_K(-P, -M; E)$, i.e., θ_K can be switched only when both P and M change sign. This property is more general and can be extended to other ferroelectric and magnetic compounds — even in absence of a net magnetization.

In Figure 24c-f, simulations considering P and M as independent variables in the cal-

culations are shown. According to Equation 13, θ_K cannot be switched if only M or P is reversed when both M and P are different from zero. This is shown in Figure 24a-b: in (a) $+P$ (or $-P$) state is considered and $+M$ switched to $-M$; in (b) $+M$ (or $-M$) state is considered and $+P$ switched to $-P$. No switching occurs. On the other hand, when $M = 0$ (e.g. antiferromagnet), θ_K changes its sign when reversing P. This leads to the important result that θ_K can be tuned and reversed by P in ferroelectric antiferromagnets (see Figure 24c, upper panel). When $P = 0$ (e.g. non-polar compound), θ_K can be tuned and reversed by M.[391] This would correspond to the standard case of a centrosymmetric ferromagnet (Figure 24c, lower panel). In general, θ_K *can be switched only when reversing both* P *and* M as shown in Figure 24d. Results can be summarized in the (P,M) space. Each couple of states considered in the panels (a-d) are shown as black and white circles in this space. The black and white circles are connected by a green or red line representing the switchability or non-switchability of the Kerr angle between them. In summary, these results suggest that: *i*) the Kerr angle can be modified not only by M but also by P; *ii*) θ_K changes its sign only when switching both P and M; *iii*) it may be possible to tune and switch the Kerr angle in AFM HOIPs; *iv*) it could be possible to design novel memory devices where the information is stored by the direction of the local ferroelectric domain and the read-out is performed by exploiting the Kerr rotation depending on the direction of the dipole. Based on these predictions, it will certainly interesting to explore the emerging class of hybrid organic-inorganic quantum materials with the potential of cross-coupling magnetic and electric order to the magneto-optical properties for active tunable photonics.

12.2 Outlook

It is important to design general principles from which material properties can be rationalized and qualitatively predicted, by focusing on the dimensionality, composition, and functional groups — by assessing their effects on the relevant properties such as P and M which are expected to be cross-coupled to the MOKE in the materials outlined here. The Bilbao Crys-

tallographic Server (BCS, http://www.cryst.ehu.es/) is useful for analyzing the magneto-optically activity (MTENSOR tool in BCS). The multilinear relation $\theta_K = \alpha P + \beta M$ requires *i*) the evaluation of the two α, β parameters for a specific material, together with their dependence on the functional groups (A,B,X) of HOIPs[391] and *ii*) understanding the microscopic mechanism of the switching properties of θ_K in terms of the underlying electronic structure, symmetry and structural properties.[404] This will open new directions in magneto-optical Kerr engineering in complex functional materials in connection with AFM spintronics[404–410] and topological quantum materials.[411–415]

13 Tribology as a novel field for electricity generation

Tribology is defined as the study of interacting surfaces in relative motion.[416] It involves various and complex phenomena, such as friction, wear and corrosion, and has severe implications for energy saving. It has been estimated that approximately 23 % of the world's total energy consumption originates from tribological contacts;[417] fortunately, several progresses have been achieved in the last decades regarding the comprehension and control of microscopic mechanisms related to friction, partly due to the advances made in simulation techniques.[418]

Despite the fact that one of the main goals of tribology is energy saving, an emerging topic is the conversion of friction into usable work. The importance of the latter becomes clear when considering the increasing demand of energy production in sustainable ways and is therefore discussed below. More specifically, the focus will now be on the production of energy through a clever control of the triboelectric effect.

In the past years, with the quick growth of electronic miniaturization, a remarkable number of novel devices (*e.g.* sensors, actuators, wireless transmitters) have been invented and introduced in many different fields, among which health care, environmental and structural monitoring, the internet of things, wireless transmission, security and nanorobotics, among

others.[419,420] These devices generally require only small-scale power (μW to mW)[421] and traditional approaches (*i.e.*, batteries) present several drawbacks, including the problematic implementation of wireless sensor networks with a huge number of distributed sensor nodes[422] or issues related to recycling.[420,423] This directly calls for the development of sustainable, maintenance-free and self-sufficient power generators that can ideally harvest energy from the environment and be integrated into such devices.

Almost every environment has an abundancy of all sorts of energy: thermal, mechanical, solar, chemical, etc. Among these, mechanical vibrations may exist in most of the environments in which a power generator can be placed. Conventional power production is obtained through electromagnetic alternators based on Faraday's law of induction. However, these types of power generation technologies can only harvest high-frequency mechanical energies efficiently.[424] This means that a broad range of energy sources in the environment (*e.g.* water waves, human body motion, thermal vibrations) cannot be effectively exploited through conventional electromagnetic generators (EMGs).[421]

To effectively convert these different small-scale energies into an electrical output, Wang and Song proposed the first nanogenerator (NG) in 2006.[425] The idea behind this device was based on the piezoelectric effect (*i.e.*, the accumulation of electric charge in response to an applied mechanical stress) and it was made of a zinc oxide nanowire array. A few years later, Wang and coworkers presented the first NG based on the triboelectric effect.[419] The triboelectric effect (or triboelectric charging) is a phenomenon that leads to the formation of charge separation between certain materials after they come into frictional contact. This effect is very common in everyday life and has been known for a long time (almost everybody has felt a small electrical shock after walking across a carpet and then touching a metallic surface). In general, both in scientific and in technological applications, this effect is considered to be negative.

The operation of triboelectric nanogenerators (TENGs) is based on triboelectrification and electrostatic induction, described by Maxwell's displacement current and change in sur-

face polarization.[426] The power density of TENGs is related to the charge density produced in tribological conditions; this led researchers to investigate the role that bulk and surface structural composition and geometry have in the tribocharge formation, together with the related dynamic features. The distinct abilities for attracting electrons of the two triboelectric surfaces result in a transfer of electrostatic charges from one surface to the other. When one triboelectric layer is displaced, the movement of charges breaks the original electrostatic balance, resulting in a potential difference being built between the two electrodes. A current through an external load can then be driven by such potential difference in order to re-balance the electrostatic status. Therefore, under periodical mechanical triggering, an alternating current (AC) output can be obtained via the TENG, and its functionality is characterized by the voltage between the electrodes, the charge transferred between electrodes and the relative displacement between triboelectric layers.

13.1 Available setups for triboelectric nanogenerators

Up to now, four different working modes have been identified:[421,422] vertical contact separation (CS), lateral sliding (LS), single electrode (SE) and freestanding triboelectric-layer (FT). All modes are schematically represented in Figure 25. CS-mode TENGs are triggered by the process of contact and separation of two triboelectric layers,[419] whilst TENGs operating in LS mode exploit the relative sliding between layers.[427] They basically differ in the kind of tribological contact exploited (vertical vs sliding). Both modes suffer from the common disadvantage that the triboelectric layers must be interconnected with an external circuit. Such a configuration might limit the application of TENGs, when one aims to harvest energy from free-moving objects. To solve this issue, SE- and FT-mode TENGs have been proposed, in which a tribolayer is simply replaced by an electrode.[428] In particular, the FT mode has been used for various high-output TENGs with record both in the maximum power output and energy conversion efficiency.[429]

The intensity of the triboelectric effect is ruled by the nature of the materials that come

into contact. So far, polymers (which contain a naturally present dipole[421]) have been mostly used as tribolayers,[430] especially in implantable TENGs for bio-medical applications.[431] Common examples of polymer materials are polydimethylsiloxane (PDMS),[432] polytetrafluoroethylene,[427] polyvinylidene fluoride,[430] fluorinated ethylene propylene,[433] polyimide,[434] and lignin.[435] Typical values of output voltage and current density for such materials are in the order of 1-10 V and 10^{-3}-10^{-1} A·m^{-2}, respectively.[422] Recently, graphene has also been used as triboelectric material in TENGs, reporting values for output voltage and current of 5 V and $5 \cdot 10^{-3}$ A·m^{-2}, respectively.[436] In addition to this, two-dimensional materials have also gained attention as triboactive candidates for TENGs.[421,436,437]

Nowadays, the choice of materials for novel TENG setups is made easier thanks to the availability of empirical lists of materials ordered by their capability of becoming tribocharged (the so-called *triboelectric series*).[438] Unfortunately, the studies on triboelectric series are sparse and they do not provide an absolute assessment of the material performance. Making current triboelectric series both quantitative and more extended would be a welcomed progress. For achieving this aim, large-scale databases and computational resources (*e.g.* NOMAD,[439] AiiDA[440]) may be of crucial importance. Moreover, since the process of charge transfer in TENGs is an interfacial phenomenon, it is obvious that the characteristics of the surface are critical for the performance of the device. The effects on the signal output of the presence of impurities and/or oxides, the surface roughness, the geometry of the contact surfaces or even the type of pre-treatment during fabrication have already been highlighted.[441] This means that materials that are considered identical according to bulk analysis may display completely different microscopic surface properties. Attempts have already been made for enhancing the surface charge density by plasma[442] and laser treatment.[443]

By design, TENGs are meant to be used to harvest energy in various environments. It is therefore crucial to know the effect that the tribological conditions (*e.g.*, contact pressure, temperature, sliding speed) can have on the TENG performance. For example, SE and FT modes can operate in open air, and thus are subject to different pressures and atmosphere

compositions. It was found that, under the same mechanical excitation, the generated charge of a PDMS-based TENG increased more than 20 % when the relative humidity was decreased from 90 % to 10% at ambient pressure. However, the interpretation of such an effect is not trivial, since a worsening of the performance is observed when the air pressure decreases from atmospheric pressure to 50 Torr in dry conditions.[444] In other studies, the influence of the temperature on the output performance of TENGs was investigated experimentally and supported by atomistic simulations.[445]

13.2 Triboelectric nanogenerator upscale

Recently, efforts have also been devoted to upscaling triboelectric nanogenerators, mainly by integrating single TENG units into a network. This was done in order to harvest low-frequency wave energy in oceans (the so-called blue energy), as a rich resource for large scale clean energy generation.[421,423,446] However, as mentioned before, harsh environmental conditions, such as humidity, have shown to significantly affect the performance of NGs.[447] One method that has proven to be promising is a hybrid approach in which conventional principles (*i.e.*, EMGs) are combined with NGs, leading to the so-called *packaging*.[448] More specifically, in this approach the TENG is made water-proof by placing it within an isolating device, thus preventing any unwanted environmental interactions. Subsequently, an EMG is wrapped around, creating an indirect driving force on the mobile part of the TENG using its magnets. It has been shown that this approach can significantly improve the performance of TENGs.[446] First of all, this is due to the fact that EMG and TENG operate in different frequency ranges, and, by combining both, one can significantly enlarge the working range.[448] Secondly, both vibrations and rotational motions can now be exploited for the generation of electricity. This is especially relevant for harvesting blue energy, which is characterized by a high irregularity and broad ranges of both frequencies and amplitudes. This novel design principle allows one to up-scale and go beyond the current efficiency of energy harvesting of these multivariate types of energies.[446]

13.3 Back to nanoscale

A common issue of the above mentioned TENGs is that frictional energy is converted into an AC output, which is unsuitable for large-impact applications such as light-emitting diodes, electronic watches and mobile phones. Current rectification is achieved by a supplementary technological effort: switching circuits, combining TENGs with storage systems, rotating-disk configurations or double-wheel designs have to be used to convert alternating to direct current (DC).[423] Moreover, the current density is limited due to the high impedance, if polymer-based systems are used.[449]

Recently, it has been shown that a DC current can be generated by direct sliding of a platinum-coated silicon atomic force microscope (AFM) tip over a molybdenum disulfide thin film deposited on a substrate.[450] In addition, this setup also produced a maximum value of current density that is several orders of magnitude greater than the usually achievable range. In such system, carrier flow is attributed to the direct electronic excitation at the interface followed by diffusion-drift conduction;[437] such excitation produces electron-hole pairs, triboluminescence and exolectrons under tribological conditions.[451] However, no relation among the chemical composition of the frictional surfaces, the tribological conditions (*i.e.*, temperature, normal load and sliding velocity) and the current density and voltage have been clearly identified yet.

To conclude this section on TENGs, it is worth to mention the Kelvin probe force microscopy (KPFM),[452] an experimental technique which can provide unique information about the tribocharging of materials at the nanoscale. Only recently researchers started to use this technique in combination with AFM for studying phenomena and properties related to the triboelectric effect.[453] However, it is expected that, in the coming years, the impact of this combination of techniques will bring significant contributions to the field. Another benefit of the KPFM/AFM approach is that the accessible time and size scales match very well with those available in classical molecular dynamics simulations.[454] Such computational tools are in fact suitable for interpreting experimental data, and especially for characteriz-

ing the effect of the tribological conditions and/or the nanostructure of the tribosurfaces. Despite the fact that classical tools can successfully simulate system sizes up to hundreds of thousands of atoms on the microsecond time scale, they cannot provide direct information about the electronic structure. However, hybrid (also called multiscale) approaches can be employed. For example, one can perform classical molecular dynamics simulations in order to assess the tribological response of the material, and then use the configurations sampled in tribological conditions for a subsequent deeper analysis by means of *ab initio* techniques. Another promising tool is represented by the hybrid QM/MM scheme, where the two levels of description are actually accessible at the same time within a single simulation.

13.4 Outlook

From the brief review given above, one can understand that, even though the computational tools for deepening our understanding of the phenomena are already in place, there is still a huge amount of work to be done. In particular, studies so far mainly dealt with polymer materials and the employment of nanostructures such as nanowires (the latter mostly for piezoelectric-based devices).[455] Moreover, the effect of the normal load on the TENG output performance has not yet been extensively studied.[456] The analysis of the hysteretic behavior of the output showed that a low contact force applied before a high one can enhance the charge transfer and consequently the performance of the device. This result is due to a dependence of the charge generation on the history of the forces applied, and such a phenomenon might be exploited in order to improve the operational performance of TENGs. Yet, the influence of ambient parameters such as humidity, temperature, and pressure on the hysteresis behavior needs to be further analyzed, if one wants to find ways to customize TENGs in various environments.

Important questions related to these aspect are still open. For example, how do tribological conditions affect the surface charge density, considered as the golden standard for assessing the overall performance of any NG?[447] Or how can the choice for certain materials

improve durability but also reduce toxicity?

To sum up, we presented an emerging topic that directly links tribology and energy harvesting. It is expected that advances in this field will have a significant socio-economic impact. Thanks to simulation approaches we expect to see a vast enlargement of the list of materials used within the coming years. Due to their superior mechanical properties, inorganic materials are promising candidates for the selection of novel triboactive materials. This, in our opinion, is particularly likely to happen, considering the preliminary results already available in the literature.[436,437,450,457–462]

14 Summary

The fast advance of the contemporary technology requires the improvement of existing materials and the discovery of new ones. In this perspective, nanostructured materials are the promising future for the creation of the next generation technology. First-principle calculations are the basic starting point to obtain a good estimation of fundamental properties such as electronic configurations, magnetic orderings, structural characteristics, optical properties and eventual coupling among these. Massive automation of such simulations would help to build a high-quality materials database to be exploited in "smart" systems (e.g. machine learning, neural networks), capable to identify existing or new materials with selected properties. However, a common standard which ensures the reliability of the results without loss of accuracy is still missing. The main effort to determine maps of materials properties (i.e. databases) is the identification of multi-parameters descriptors. Despite SISSO is a valid engine to determine such descriptors, the approach is currently limited to scalar features and the next step is to develop a systematic strategy to build environment-dependent features to be used as candidates in the feature space. Open source projects which share materials data are the most effective means to obtain a rapid expansion of the databases. Machine-learning based tools have already become popular for the purpose of predicting materials properties,

thanks to the sharing paradigm. However, the quality of the database is crucial to obtain appropriate answers: unbalanced number of members in a family of materials could lead to systematic errors which must be accounted for. Data visualization techniques could help to identify such errors and guide the correction of the predicting model.

Besides high-throughput simulation machineries, massive ab-initio molecular dynamics and meta-dynamics techniques are an other efficient tool to explore and design material properties, especially when chemical reactions are to be taken into account. Nevertheless, the high cost of such kind of simulations is still a drawback, and statistical methods like Monte-Carlo-based ones represent a promising alternative to overcome such limitation. An other opportunity is the use of ad hoc descriptors, which can facilitate the characterization of specific processes, and go at the same pace with the extension of existing theoretical frameworks or the development of new ones. This is the case of the here discussed specific applications such as the dendrite growth in batteries, vapochromic responses to small-molecule analytes, photoactivated linkage isomerism, prevention of He embrittlement in containment materials in nuclear reactors, thermoelectric figure of merit, metalized ferroelectrics, magneto-optical Kerr effect, and tribocharge generation. In these cases, the descriptors have been proposed based on physical reasoning rather than from statistical observations of gathered data.

From our perspective, atomistic simulations, automated modeling and experimental techniques are rapidly developing and becoming more and more widely available. The mutual integration between theory and experiment turns out to be mandatory to significatively boost the advance of the scientific knowledge and to unveil new physical insights, which will ultimately lead to the design of novel functional materials with tunable properties meeting contemporary challenges.

Acknowledgement

A.C., P.N. and H.S.S. acknowledge support of this work by the Czech Science Foundation (projects 17-24164Y, 16-11516Y and 17-17921S), by Novel nanostructures for engineering applications No. CZ.02.1.01/0.0/0.0/16_026/0008396 and by The Ministry of Education, Youth and Sports from the Large Infrastructures for Research, Experimental Development and Innovations project "IT4Innovations National Supercomputing Center – LM2015070".

The work of A.G. contributes to the research performed at CELEST (Center for Electrochemical Energy Storage Ulm-Karlsruhe).

J.M.S. is grateful to the UK Engineering and Physical Sciences Research Council (EPSRC) for support (grant nos. EP/K004956/1 and EP/P007821/1) and to the University of Manchester for the award of a Presidential Fellowship.

C.F. would like to thank Peitao Liu, Jiangang He and Georg Kresse for the long standing collaboration on the topic discussed in this contribution. This work was supported by the Austrian Science Fund (FWF) within the SFB ViCoM (Grant No. F41), and by the joint DST (Indian Department of Science and Technology)-FWF project INDOX (I1490-N19).

T.D.S. and S.K.K. gratefully acknowledge support from National Science Foundation through CAREER Award 1651668.

The work of F.B. and V.E.P.C. has received funding from the European Union's Horizon2020 research and innovation programme under grant agreement No. 721642: SOLUTION.

L. G. acknowledges Matthias Scheffler, the main driving force behind all the works and activities presented in this contribution and all the people that contributed to the specific projects. For the SISSO development: Runhai Ouyang, Emre Ahmetcik, and Stefano Curtarolo. For the perovskite classification: Christopher J. Bartel, Christopher Sutton, Bryan R. Goldsmith, and Charles B. Musgrave. L. G. also acknowledges all the PIs that made the NOMAD Laboratory possible, besides Matthias Scheffler who is the coordinator of the Centre of Excellence: Angel Rubio, Risto Nieminen, Francesc Illas, Daan Frenkel, Claudia

Draxl, Alessandro De Vita, Kristian Thygesen, Kimmo Koski, Stefan Heinzel, Jose Maria Cela, Dieter Kranzlmüller, Ciaran Clissman. The project has received funding from the European Union's Horizon 2020 research and innovation program (#676580: The NOMAD Laboratory — an European Center of Excellence and #740233: TEC1p), and the Berlin Big-Data Center (BBDC, #01IS14013E).

B.G. and R.P. acknowledge funding by the German Research Foundation (Deutsche Forschungsgemeinschaft, DFG) within CRC/TRR 80, Project No. G8, and computing time at magnitUDE granted by the Center for Computational Sciences and Simulation of the University of Duisburg-Essen (DFG Grants No. INST 20876/209-1 FUGG and No. INST 20876/243-1 FUGG).

V.F. acknowledges support by Università di Cagliari, Fondazione di Sardegna, Regione Autonoma Sardegna via Progetto biennale di ateneo 2016 *Multiphysics approach to thermoelectricity*, and by CINECA via ISCRA grants.

T. P. acknowledges support by the project Novel nanostructures for engineering applications No. CZ.02.1.01/0.0/0.0/16_026/0008396.

A.S. thanks the High End Foreign Expert program and Shanghai Eastern Scholar Chair Professor program and Y. Qi for kind help in making the figures. P.V. acknowledges support from the Spanish Ministry of Economy, Industry and Competitiveness under the Maria de Maeztu Units of Excellence Programme - MDM-2016-0618.

Authors contribution

The present viewpoint was written thanks to the contribution of all authors. Here in the following, the name of each section together with the initials of the authors contributing to it are reported for reader's convenience:

- "Predicting the band gap of complex materials: computational methods and procedures": C. F.;

- "Data-driven materials science: building maps of materials properties": L. M. G.;
- "Identifying error in machine learning models": T. D. S., K. K.;
- "Accelerated ab initio molecular dynamics applied to the simulation of heterogeneous catalysis": L. F., A. C.-V.;
- "Predictive description of catalytic systems using microkinetic modeling": M. V.;
- "Atomic design principle for safer battery materials": A. G.;
- "Responsive molecular solids": J. M. S.;
- "Materials for nuclear reactors": T. P., H. S. S.;
- "Novel mechanisms for improved oxide thermoelectrics explored from first principles": B. G., R. P.;
- "Polar, ferroelectric and multiferroic metals: three case studies": V. F., A. F., A. U., H. J. Z., J. I.;
- "Electric Magneto-Optical properties in multi-functional hybrid materials": K. Y., F. F., S. H., W. R., F. R., P. V., J. M., N. D., H. W., A. S.;
- "Tribology as a novel field for electricity generation": P. N., A. C., F. B., V. E. P. C.

Finally, A. C., R. C., and D. P. conceptualized the work, composed the manuscript and supervised the merging of all the contributions.

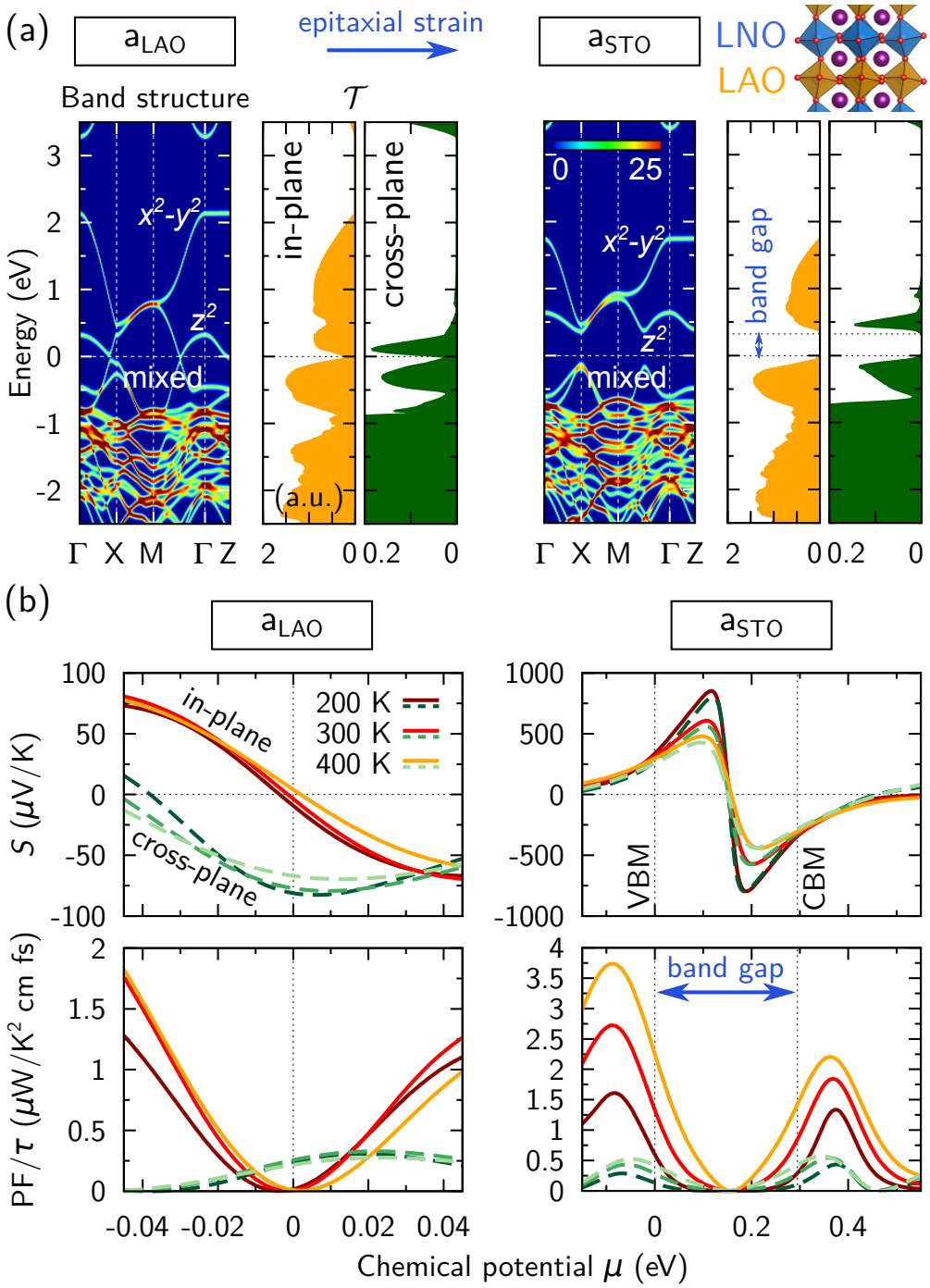

Figure 18: (a) In ultrathin $(LNO)_1/(LAO)_1(001)$ SLs, increasing the substrate lattice constant from a_{LAO} (compressive strain) to a_{STO} (tensile strain) drives a metal-to-insulator transition,[311] as one can see from the band structure diagrams and the corresponding transmission $\mathcal{T}$. (b) This is accompanied by a drastic enhancement of the thermoelectric response (Seebeck coefficient S and power factor PF), both in-plane and cross-plane. Further increase of strain was found to be counterproductive.[290] (Adapted from Ref. 290.)

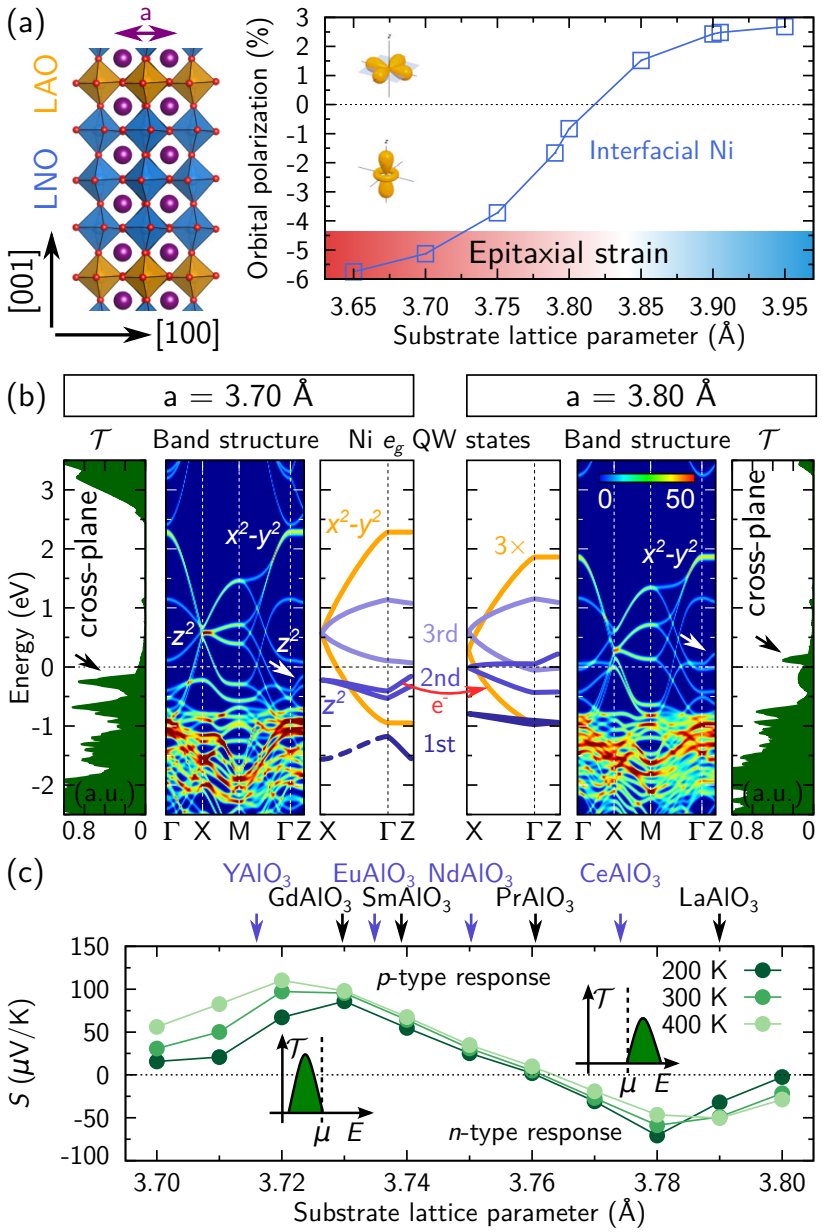

Figure 19: (a) Side view of the optimized geometry of a nonpolar $(LNO)_3/(LAO)_1(001)$ SL (a = 3.79 Å), together with the Ni e_g orbital polarization in the interfacial LNO layers as a function of the substrate lattice parameter a that varies from −6 % (compressive strain, red shaded) to ∼ +3 % (tensile strain, blue shaded). (b) Confining three layers of LNO separated by a single LAO spacer layer leads to the formation of distinct QW states with Ni e_g character. Their relative occupation (and thus the orbital polarization) can be precisely tuned by epitaxial strain. In particular, resonances emerge in the cross-plane transmission $\mathcal{T}$ (black arrows) that are associated with the $3d_{z^2}$-derived QW states (white arrows) and can be shifted with respect to the Fermi energy by moderately varying the degree of strain. (c) With this strain engineering of the orbital polarization, considerable n- and p-type thermoelectric response can be achieved in the system. Exemplarily, some (rare-earth) aluminate substrates are marked. (Adapted from Ref. 291.)

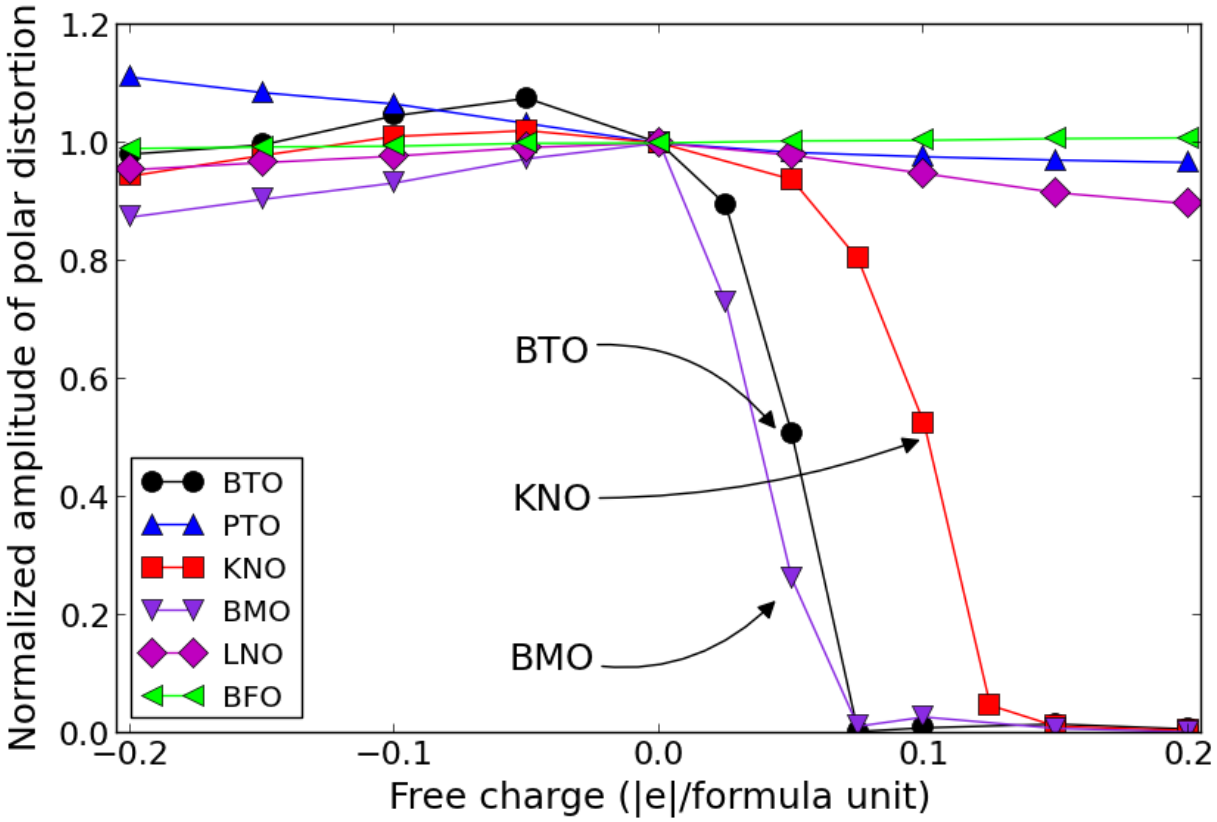

Figure 20: Normalized polar amplitude vs carrier density for a sample of metalized ferroelectrics. In the legend, $BaTiO_3$, $PbTiO_3$, $KNbO_3$, $BaMnO_3$, $LiNbO_3$ and $BaFeO_3$ compounds are represented by the elements' initials, respectively. For example, 0.1 $|e|$/formula unit are 1.5×10^{21} cm^{-3} in BTO. Figure adapted from Ref. 332.

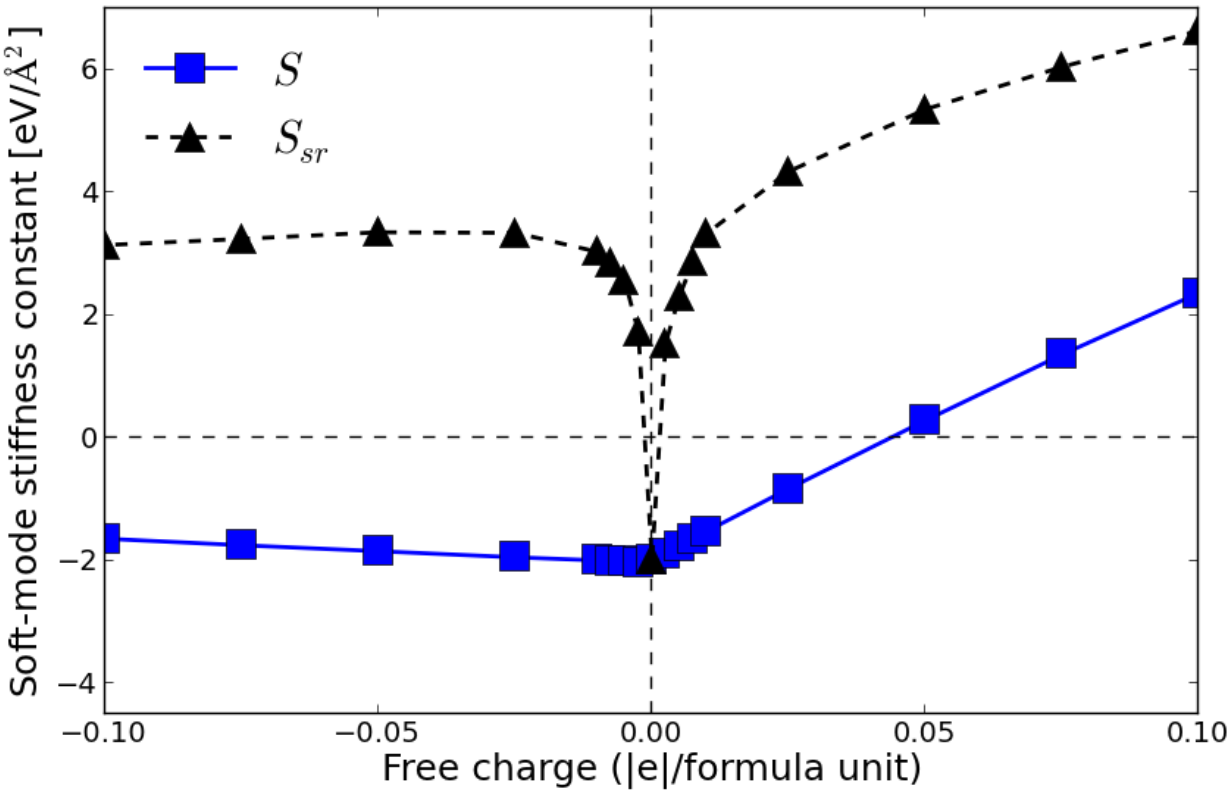

Figure 21: Force constants vs carrier density for a sample of metalized ferroelectrics. Negative values of the stiffness indicate the occurrence of a polar distortion, while positive values correspond to stability against polar distortion.

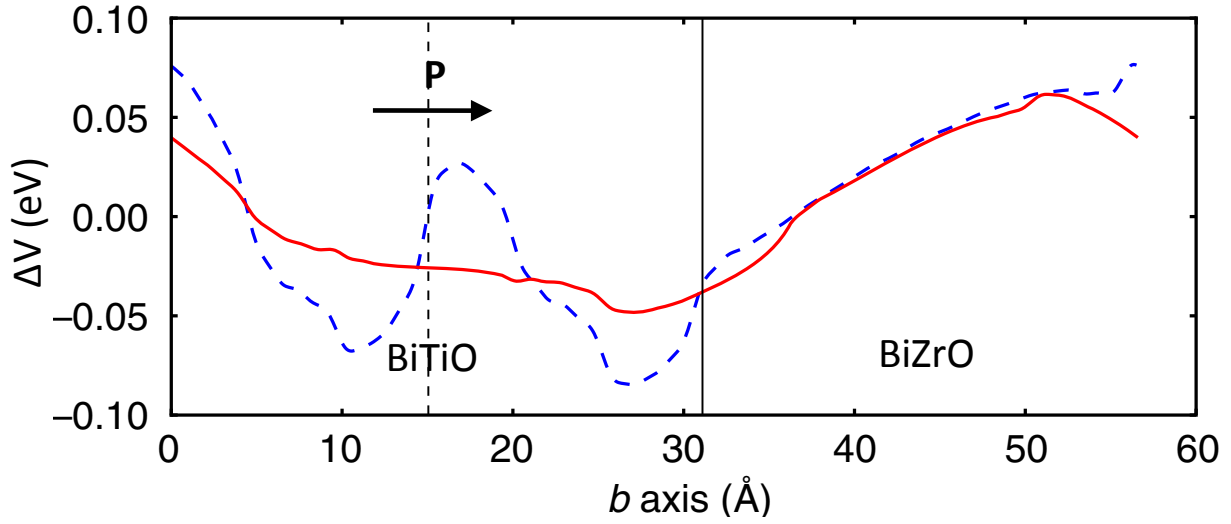

Figure 22: Potential difference of the polar and non-polar BiTiO-5517/BiZrO-227 superlattice, exhibiting the sawtooth shape due to interface polarization charge. The two lines correspond to two different running-average filters. Figure adapated from Ref. 333.

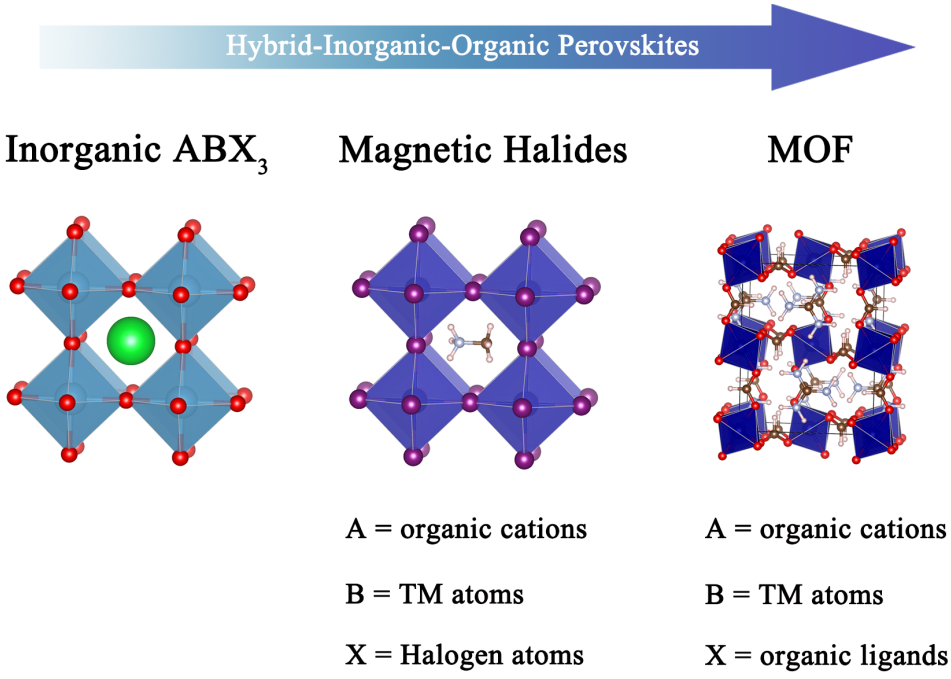

Figure 23: Starting from an inorganic ABX_3 perovskite: magnetic halides and metal-organic frameworks (TM: transition metal).

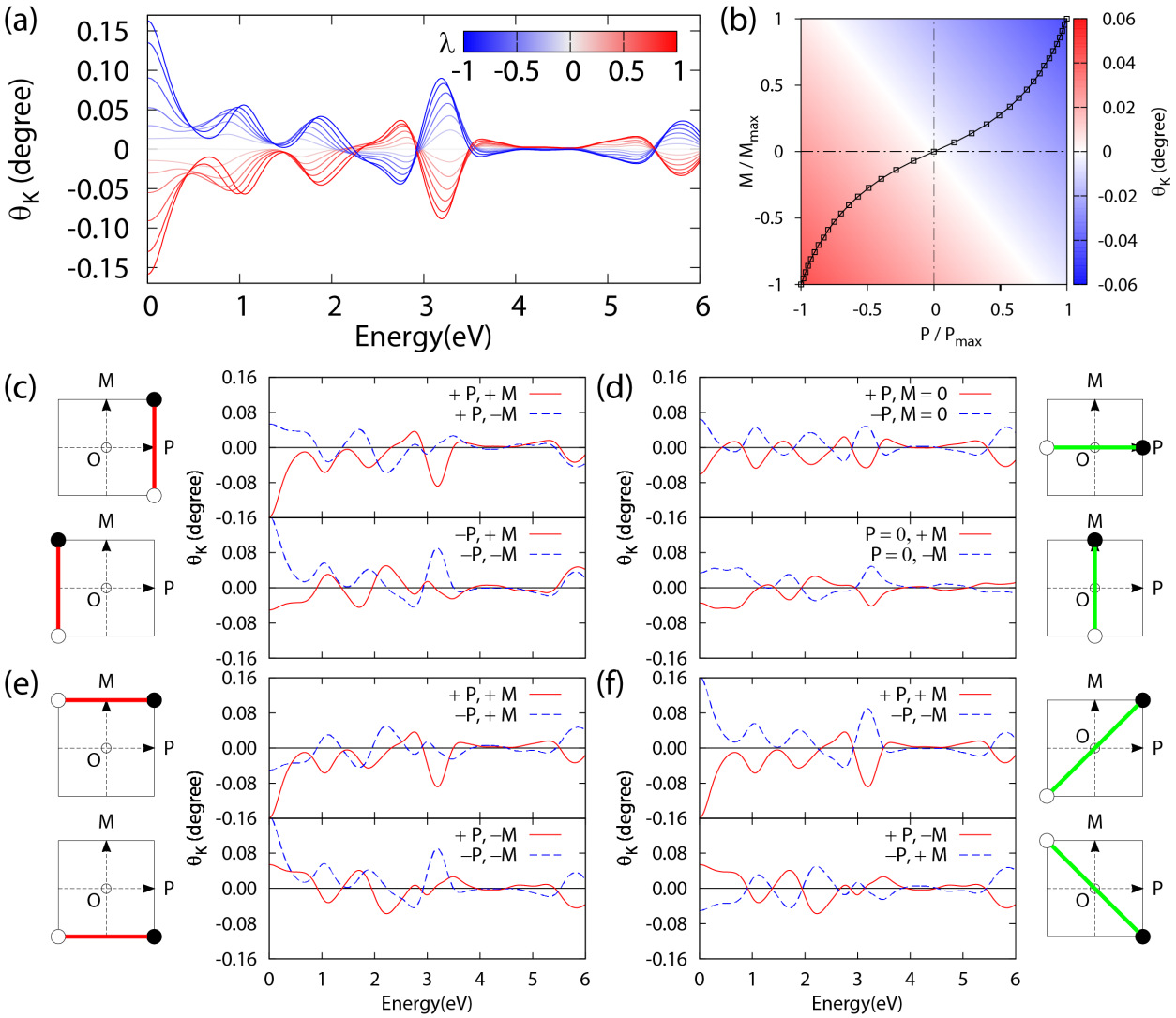

Figure 24: (a) θ_K as a function of the incident photon energy for different value of normalized amplitude of the polar distortion λ from -1 to +1. (b) Color scheme representation of different points in (P,M) space. Black curve represents the magneto-electric states, while the green line represent the locus of points with zero Kerr angle for the selected energy 3.8 eV. (c-f) Switching properties of the Kerr angle for different states in (P,M) space: green (red) lines connect states for which the Kerr angle does (not) switch.[391] The results are shown for the $[C(NH_2)_3]Cr(HCOO)_3$ MOF.

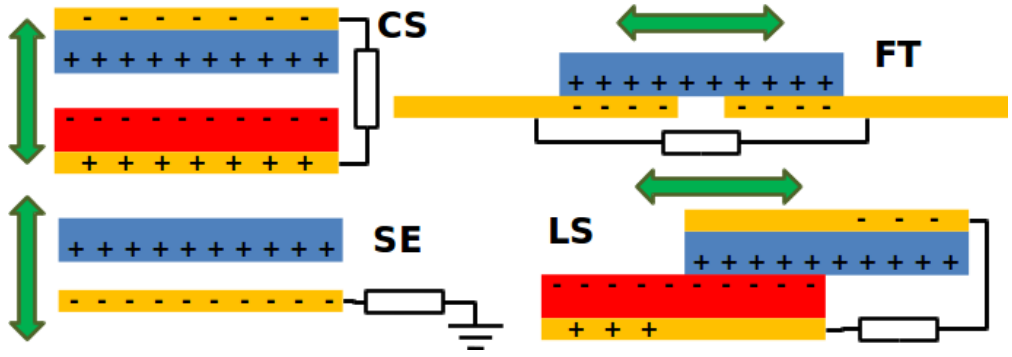

Figure 25: Four basic operation modes for TENGs: contact separation (CS), freestanding triboelectric-layer (FT), single electrode (SE) and lateral sliding (LS). Blue and red boxes represent the tribolayers, whilst electrodes are drawn in yellow.

References

(1) Rogers, C.; Barker, D.; Jaeger, C. Introduction to smart materials and structures. Structures & Mathematical Issues Workshop Proceedings. 2016.

(2) Hohenberg, P.; Kohn, W. *Phys. Rev.* **1964**, *136*, B864.

(3) Kohn, W.; Sham, L. J. *Phys. Rev.* **1965**, *140*, A1133.

(4) Hubbard, J.; Flowers, B. H. *Proceedings of the Royal Society of London. Series A. Mathematical and Physical Sciences* **1963**, *276*, 238.

(5) Heyd, J.; Scuseria, G. E.; Ernzerhof, M. *The Journal of Chemical Physics* **2003**, *118*, 8207–8215.

(6) Kim, K.; Jordan, K. D. *The Journal of Physical Chemistry* **1994**, *98*, 10089–10094.

(7) Stephens, P. J.; Devlin, F. J.; Chabalowski, C. F.; Frisch, M. J. *The Journal of Physical Chemistry* **1994**, *98*, 11623–11627.

(8) Aryasetiawan, F.; Gunnarsson, O. *Reports on Progress in Physics* **1998**, *61*, 237.

(9) Salpeter, E. E.; Bethe, H. A. *Phys. Rev.* **1951**, *84*, 1232.

(10) He, J.; Franchini, C. *Journal of Physics: Condensed Matter* **2017**, *29*, 454004.

(11) Nunes, R. W.; Gonze, X. *Phys. Rev. B* **2001**, *63*, 155107.

(12) Ergönenc, Z.; Kim, B.; Liu, P.; Kresse, G.; Franchini, C. *Phys. Rev. Materials* **2018**, *2*, 024601.

(13) Chen, W.; Miceli, G.; Rignanese, G.-M.; Pasquarello, A. *Phys. Rev. Materials* **2018**, *2*, 073803.

(14) Grüneis, A. In *Handbook of Materials Modeling*; Andreoni, W., Yip, S., Eds.; Springer International Publishing, 2018.

(15) Bokdam, M.; Sander, T.; Stroppa, A.; Picozzi, S.; Sarma, D.; Franchini, C.; Kresse, G. *Scientific reports* **2016**, *6*, 28618.

(16) Sander, T.; Maggio, E.; Kresse, G. *Phys. Rev. B* **2015**, *92*, 045209.

(17) Liu, P.; Kim, B.; Chen, X.-Q.; Sarma, D. D.; Kresse, G.; Franchini, C. *Phys. Rev. Materials* **2018**, *2*, 075003.

(18) Hirata, S.; Head-Gordon, M. *Chemical Physics Letters* **1999**, *314*, 291.

(19) *https://materials.springer.com*

(20) Jain, A.; Hautier, G.; Moore, C. J.; Ong, S. P.; Fischer, C. C.; Mueller, T.; Persson, K. A.; Ceder, G. *Comput. Mater. Sci.* **2011**, *50*, 2295–2310.

(21) Curtarolo, S.; Hart, G. L. W.; Setyawan, W.; Mehl, M. J.; Jahnátek, M.; Chepulskii, R. V.; Levy, O.; Morgan, D. *"AFLOW: software for high-throughput calculation of material properties",* http://materials.duke.edu/aflow.html **2010**,

(22) Saal, J. E.; Kirklin, S.; Aykol, M.; Meredig, B.; Wolverton, C. *JOM* **2013**, *65*, 1501–1509.

(23) Wilkinson, M. D. et al. *Scientific Data* **2016**, *3*, 160018 EP –, Comment.

(24) Ghiringhelli, L. M.; Carbogno, C.; Levchenko, S.; Mohamed, F.; Huhs, G.; Lüders, M.; Oliveira, M.; Scheffler, M. *npj Computational Materials* **2017**, *3*, 46.

(25) Draxl, C.; Scheffler, M. *MRS Bulletin* **2018**, *43*, 676–682.

(26) Bartók, A.; Albert, P.; Payne, M. C.; Kondor, R.; Csányi, G. *Phys. Rev. Lett.* **2010**, *104*, 136403.

(27) Behler, J. *The Journal of chemical physics* **2011**, *134*, 074106.

(28) Carrete, J.; Mingo, N.; Wang, S.; Curtarolo, S. *Adv. Func. Mater.* **2014**, *24*, 7427–7432.

(29) Rajan, K. *Annu. Rev. Mater. Res.* **2015**, *45*, 153–169.

(30) Mueller, T.; Kusne, A. G.; Ramprasad, R. *Reviews in Computational Chemistry*; John Wiley & Sons, Inc, 2016; pp 186–273.

(31) Kim, C.; Pilania, G.; Ramprasad, R. *Chem. Mater.* **2016**, *28*, 1304–1311.

(32) Faber, F. A.; Lindmaa, A.; von Lilienfeld, O. A.; Armiento, R. *Phys. Rev. Lett.* **2016**, *117*, 135502.

(33) Takahashi, K.; Tanaka, Y. *Dalton Trans.* **2016**, *45*, 10497–10499.

(34) Bartók, A.; De, S.; Poelking, C.; Bernstein, N.; Kermode, J.; Csányi, G.; Ceriotti, M. *Sci. Adv.* **2017**, *3*, 1701816.

(35) Goldsmith, B. R.; Boley, M.; Vreeken, J.; Scheffler, M.; Ghiringhelli, L. M. *New J. Phys.* **2017**, *19*, 013031.

(36) Pham, T. L.; Nguyen, N. D.; Nguyen, V. D.; Kino, H.; Miyake, T.; Dam, H. C. *J. Chem. Phys.* **2018**, *148*, 204106.

(37) Ziletti, A.; Kumar, D.; Scheffler, M.; Ghiringhelli, L. M. *Nature communications* **2018**, *9*, 2775.

(38) Sutton, C.; Ghiringhelli, L. M.; Yamamoto, T.; Lysogorskiy, Y.; Blumenthal, L.; Hammerschmidt, T.; Golebiowski, J.; Liu, X.; Ziletti, A.; Scheffler, M. *arXiv preprint arXiv:1812.00085* **2018**,

(39) Ghiringhelli, L. M.; Vybiral, J.; Levchenko, S. V.; Draxl, C.; Scheffler, M. *Phys. Rev. Lett.* **2015**, *114*, 105503.

(40) Candès, E. J.; Wakin, M. B. *IEEE Signal Proc. Mag.* **2008**, *25*, 21–30.

(41) Nelson, L. J.; Hart, G. L. W.; Zhou, F.; Ozoliņš, V. *Phys. Rev. B* **2013**, *87*, 035125.

(42) Ghiringhelli, L. M.; Vybiral, J.; Ahmetcik, E.; Ouyang, R.; Levchenko, S. V.; Draxl, C.; Scheffler, M. *New J. Phys.* **2017**, *19*, 023017.

(43) Guyon, I.; Elisseeff, A. *J. Mach. Learn. Res.* **2003**, *3*, 1157–1182.

(44) Ouyang, R.; Curtarolo, S.; Ahmetcik, E.; Scheffler, M.; Ghiringhelli, L. M. *Phys. Rev. Mater.* **2018**, *2*, 083802.

(45) Fan, J.; Lv, J. *J. R. Statist. Soc. B* **2008**, *70*, 849–911.

(46) Tibshirani, R. *J. R. Statist. Soc. B* **1996**, *58*, 267–288.

(47) Tropp, J. A.; Gilbert, A. C. *IEEE Trans. Inform. Theory* **2007**, *53*, 4655–4666.

(48) Pati, Y. C.; Rezaiifar, R.; Krishnaprasad, P. S. *The Twenty-Seventh Asilomar Conf.: Signals, Systems and Computers*; Nov. 1993; Vol. 1; pp 40–44.

(49) Bartel, C. J.; Sutton, C.; Goldsmith, B. R.; Ouyang, R.; Musgrave, C. B.; Ghiringhelli, L. M.; Scheffler, M. *Science Advances* **2019**, *5*, eaav0693.

(50) Ghiringhelli, L. `https://th.fhi-berlin.mpg.de/movies/?m=nomadbat`, 2017.

(51) Regler, B. `https://analytics-toolkit.nomad-coe.eu/tutorial-periodic-table`, 2017.

(52) Acosta, C. M.; Ouyang, R.; Fazzio, A.; Scheffler, M.; Ghiringhelli, L. M.; Carbogno, C. *arXiv:1805.10950* **2018**,

(53) Bartel, C. J.; Millican, S. L.; Deml, A. M.; Rumptz, J. R.; Tumas, W.; Weimer, A. W.; Lany, S.; Stevanović, V.; Musgrave, C. B.; Holder, A. M. *Nat. Commun.* **2018**, *9*, 4168.

(54) Hwang, J.; Rao, R. R.; Giordano, L.; Katayama, Y.; Yu, Y.; Shao-Horn, Y. *Science* **2017**, *358*, 751–756.

(55) Duan, C.; Tong, J.; Shang, M.; Nikodemski, S.; Sanders, M.; Ricote, S.; Almansoori, A.; O'Hayre, R. *Science* **2015**, *349*, 1321–1326.

(56) Cohen, R. E. *Nature* **1992**, *358*, 136–138.

(57) Yi, T.; Chen, W.; Cheng, L.; Bayliss, R. D.; Lin, F.; Plews, M. R.; Nordlund, D.; Doeff, M. M.; Persson, K. A.; Cabana, J. *Chemistry of Materials* **2017**, *29*, 1561–1568.

(58) Correa-Baena, J.-P.; Saliba, M.; Buonassisi, T.; Grätzel, M.; Abate, A.; Tress, W.; Hagfeldt, A. *Science* **2017**, *358*, 739–744.

(59) Kovalenko, M. V.; Protesescu, L.; Bodnarchuk, M. I. *Science* **2017**, *358*, 745–750.

(60) Kirkpatrick, S.; Gelatt, C. D.; Vecchi, M. P. *science* **1983**, *220*, 671–680.

(61) Doye, J. P.; Wales, D. J. *Physical review letters* **1998**, *80*, 1357.

(62) Goedecker, S. *The Journal of chemical physics* **2004**, *120*, 9911–9917.

(63) Oganov, A. R.; Lyakhov, A. O.; Valle, M. *Accounts of chemical research* **2011**, *44*, 227–237.

(64) Curtarolo, S.; Hart, G. L.; Nardelli, M. B.; Mingo, N.; Sanvito, S.; Levy, O. *Nature materials* **2013**, *12*, 191.

(65) Goldschmidt, V. M. *Naturwissenschaften* **1926**, *14*, 477–485.

(66) Li, W.; Wang, Z.; Deschler, F.; Gao, S.; Friend, R. H.; Cheetham, A. K. *Nature Reviews Materials* **2017**, *2*, 16099.

(67) Zhang, H.; Li, N.; Li, K.; Xue, D. *Acta Crystallographica Section B: Structural Science* **2007**, *63*, 812–818.

(68) Li, C.; Lu, X.; Ding, W.; Feng, L.; Gao, Y.; Guo, Z. *Acta Crystallographica Section B: Structural Science* **2008**, *64*, 702–707.

(69) Travis, W.; Glover, E.; Bronstein, H.; Scanlon, D.; Palgrave, R. *Chemical Science* **2016**, *7*, 4548–4556.

(70) Mansouri Tehrani, A.; Oliynyk, A.; Parry, M.; Rizvi, Z.; Couper, S.; Lin, F.; Miyagi, L.; Sparks, T.; Brgoch, J. *Journal of the American Chemical Society* **2018**, *140*, 9844–9853.

(71) Gaultois, M. W.; Oliynyk, A.; Mar, A.; Sparks, T.; Mulholland, G. J.; Meredig, B. *APL Materials* **2016**, *4*, 053213.

(72) Sparks, T.; Gaultois, M. W.; Oliynyk, A.; Brgoch, J.; Meredig, B. *Scripta Materialia* **2016**, *111*, 10–15.

(73) Kauwe, S.; Graser, J.; Vazquez, A.; Sparks, T. *Integrating Materials and Manufacturing Innovation* **2018**, *7*, 43–51.

(74) Graser, J.; Kauwe, S.; Sparks, T. *Chemistry of Materials* **2018**, *30*, 3601–3612.

(75) Lemonick, S. *Chemical & Engineering News* **2018**, *96*, 16–20.

(76) Seshadri, R.; Sparks, T. D. *APL Materials* **2016**, *4*, 053206.

(77) Michel, K.; Meredig, B. *Mrs Bulletin* **2016**, *41*, 617.

(78) Kauwe, S.; Yang, Y.; Sparks, T. *ChemRxiv* **2019**, https://chemrxiv.org/s/cea9ca4196730fae1677.

(79) Kauwe, S. K.; Welker, T.; Sparks, T. D. *ChemRXiv* **2018**,

(80) Maaten, L.; Hinton, G. *Journal of machine learning research* **2008**, *9*, 2579–2605.

(81) Meredig, B.; Antono, E.; Church, C.; Hutchinson, M.; Ling, J.; Paradiso, S.; Blaiszik, B.; Foster, I.; Gibbons, B.; Hattrick-Simpers, J.; Mehta, A.; Ward, L. *Mol. Syst. Des. Eng.* **2018**, *3*, 819–825.

(82) Nørskov, J. K.; Bligaard, T.; Rossmeisl, J.; Christensen, C. H. *Nature Chemistry* **2009**, *1*, 37 EP –.

(83) Nørskov, J. K.; Abild-Pedersen, F.; Studt, F.; Bligaard, T. *Proceedings of the National Academy of Sciences* **2011**, *108*, 937–943.

(84) Michaelides, A.; Scheffler, M. *Surface and Interface Science*; John Wiley & Sons, Ltd, 2014; Chapter 2, pp 13–72.

(85) Dumesic, J. *The Microkinetics of heterogeneous catalysis*; ACS professional reference book; American Chemical Society, 1993.

(86) Comas-Vives, A.; Furman, K.; Gajan, D.; Akatay, M. C.; Lesage, A.; Ribeiro, F. H.; Copéret, C. *Phys. Chem. Chem. Phys.* **2016**, *18*, 1969–1979.

(87) Piccini, G.; Sauer, J. *Journal of Chemical Theory and Computation* **2014**, *10*, 2479–2487.

(88) Piccini, G.; Alessio, M.; Sauer, J. *Angewandte Chemie International Edition* **2016**, *55*, 5235–5237.

(89) Alessio, M.; Bischoff, F. A.; Sauer, J. *Phys. Chem. Chem. Phys.* **2018**, *20*, 9760–9769.

(90) Li, H.; Paolucci, C.; Schneider, W. F. *Journal of Chemical Theory and Computation* **2018**, *14*, 929–938.

(91) Sprowl, L. H.; Campbell, C. T.; ÃĄrnadÃşttir, L. *The Journal of Physical Chemistry C* **2016**, *120*, 9719–9731.

(92) Campbell, C. T.; Sprowl, L. H.; ÃĄrnadÃşttir, L. *The Journal of Physical Chemistry C* **2016**, *120*, 10283–10297.

(93) Bajpai, A.; Mehta, P.; Frey, K.; Lehmer, A. M.; Schneider, W. F. *ACS Catalysis* **2018**, *8*, 1945–1954.

(94) JÃÿrgensen, M.; GrÃűnbeck, H. *The Journal of Physical Chemistry C* **2017**, *121*, 7199–7207.

(95) Sun, G.; Jiang, H. *The Journal of Chemical Physics* **2015**, *143*, 234706.

(96) Cammarata, A.; Polcar, T. *Physical Review B* **2017**, *96*, 085406.

(97) Foppa, L.; Iannuzzi, M.; Copéret, C.; Comas-Vives, A. *ACS Catalysis* **2018**, *8*, 6983–6992.

(98) Foppa, L.; Iannuzzi, M.; Copéret, C.; Comas-Vives, A. *J. Catal.* **2019**, *371*, 270 – 275.

(99) Marx, D.; Hutter, J. *Ab Initio Molecular Dynamics: Basic Theory and Advanced Methods*; Cambridge University Press, 2009.

(100) *Modern Methods and Algorithms of Quantum Chemistry: Proceedings. ...*; NIC series; John-von-Neumann-Inst. for Computing, 2000.

(101) Laio, A.; Parrinello, M. *Proceedings of the National Academy of Sciences* **2002**, *99*, 12562–12566.

(102) Laio, A.; Rodriguez-Fortea, A.; Gervasio, F. L.; Ceccarelli, M.; Parrinello, M. *The Journal of Physical Chemistry B* **2005**, *109*, 6714–6721.

(103) Barducci, A.; Bonomi, M.; Parrinello, M. *Wiley Interdisciplinary Reviews: Computational Molecular Science* **2011**, *1*, 826–843.

(104) Iannuzzi, M.; Laio, A.; Parrinello, M. *Phys. Rev. Lett.* **2003**, *90*, 238302.

(105) Ensing, B.; De Vivo, M.; Liu, Z.; Moore, P.; Klein, M. L. *Accounts of Chemical Research* **2006**, *39*, 73–81.

(106) Comas-Vives, A.; Stirling, A.; Lledós, A.; Ujaque, G. *Chemistry — A European Journal* **2010**, *16*, 8738–8747.

(107) Martínez-Suárez, L.; Siemer, N.; Frenzel, J.; Marx, D. *ACS Catalysis* **2015**, *5*, 4201–4218.

(108) Cheng, T.; Xiao, H.; Goddard, W. A. *Proceedings of the National Academy of Sciences* **2017**, *114*, 1795–1800.

(109) Gurdal, Y.; Hutter, J.; Iannuzzi, M. *The Journal of Physical Chemistry C* **2017**, *121*, 11416–11427.

(110) Loveless, B. T.; Buda, C.; Neurock, M.; Iglesia, E. *Journal of the American Chemical Society* **2013**, *135*, 6107–6121.

(111) Ciobica, I. M.; van Santen, R. A. *The Journal of Physical Chemistry B* **2003**, *107*, 3808–3812.

(112) Reuter, K.; Scheffler, M. *Phys. Rev. B* **2001**, *65*, 035406.

(113) Micheletti, C.; Laio, A.; Parrinello, M. *Phys. Rev. Lett.* **2004**, *92*, 170601.

(114) Behler, J. *The Journal of Chemical Physics* **2016**, *145*, 170901.

(115) James, A. D. *The Microkinetics of heterogeneous catalysis*; Washington, DC : American Chemical Society, 1993., 1993.

(116) Broadbelt, L. J.; Snurr, R. Q. *Applied Catalysis A: General* **2000**, *200*, 23 – 46.

(117) Stoltze, P. *Progress in Surface Science* **2000**, *65*, 65–150.

(118) Raimondeau, S.; Vlachos, D. G. *Chemical Engineering Journal* **2002**, *90*, 3–23.

(119) Salciccioli, M.; Stamatakis, M.; Caratzoulas, S.; Vlachos, D. G. *Chemical Engineering Science* **2011**, *66*, 4319–4355.

(120) Vlachos, D. G. *AIChE Journal* **2012**, *58*, 1314–1325.

(121) Stamatakis, M.; Vlachos, D. G. *ACS Catalysis* **2012**, *2*, 2648–2663.

(122) Vandichel, M.; Moscu, A.; Gronbeck, H. *Acs Catalysis* **2017**, *7*, 7431–7441.

(123) Jorgensen, M.; Gronbeck, H. *ACS Catalysis* **2016**, *6*, 6730–6738.

(124) Heard, C. J.; Siahrostami, S.; Gronbeck, H. *Journal of Physical Chemistry C* **2016**, *120*, 995–1003.

(125) Van den Bossche, M.; Gronbeck, H. *Journal of the American Chemical Society* **2015**, *137*, 12035–12044.

(126) Choksi, T.; Greeley, J. *Acs Catalysis* **2016**, *6*, 7260–7277.

(127) Hus, M.; Kopac, D.; Stefancic, N. S.; Jurkovic, D. L.; Dasireddy, V. D. B. C.; Likozar, B. *Catal. Sci. Technol.* **2017**, *7*, 5900–5913.

(128) Foppa, L.; Silaghi, M.-C.; Larmier, K.; Comas-Vives, A. *Journal of Catalysis* **2016**, *343*, 196–207.

(129) Foppa, L.; Margossian, T.; Kim, S. M.; MÃijller, C.; CopÃľret, C.; Larmier, K.; Comas-Vives, A. *Journal of the American Chemical Society* **2017**, *139*, 17128–17139.

(130) Van der Borght, K.; Toch, K.; Galvita, V. V.; Thybaut, J. W.; Marin, G. B. *Catalysts* **2015**, *5*, 1948–1968.

(131) Jorgensen, M.; Gronbeck, H. *Angewandte Chemie-International Edition* **2018**, *57*, 5086–5089.

(132) Bell, R. P. *Proceedings of the Royal Society of London A: Mathematical, Physical and Engineering Sciences* **1936**, *154*, 414–429.

(133) Evans, M. G.; Polanyi, M. *Transactions of the Faraday Society* **1936**, *32*, 1333–1360.

(134) Hammett, L. P.; Paul, M. A. *Journal of the American Chemical Society* **1934**, *56*, 830–832.

(135) Hammer, B.; Norskov, J. K. *Nature* **1995**, *376*, 238.

(136) Liu, P.; Norskov, J. K. *Physical Chemistry Chemical Physics* **2001**, *3*, 3814–3818.

(137) Jacobsen, C. J. H.; Dahl, S.; Clausen, B. S.; Bahn, S.; Logadottir, A.; NÃÿrskov, J. K. *Journal of the American Chemical Society* **2001**, *123*, 8404–8405.

(138) Norskov, J. K.; Bligaard, T.; Rossmeisl, J.; Christensen, C. H. *Nature Chemistry* **2009**, *1*, 37–46.

(139) Medford, A. J.; Shi, C.; Hoffmann, M. J.; Lausche, A. C.; Fitzgibbon, S. R.; Bligaard, T.; Norskov, J. K. *Catalysis Letters* **2015**, *145*, 794–807.

(140) Stroppa, A.; Mittendorfer, F.; Andersen, J. N.; Parteder, G.; Allegretti, F.; Surnev, S.; Netzer, F. P. *The Journal of Physical Chemistry C* **2009**, *113*, 942–949.

(141) Schimka, L.; Harl, J.; Stroppa, A.; GrÃijneis, A.; Marsman, M.; Mittendorfer, F.; Kresse, G. *Nature Materials* **2010**, *9*, 741.

(142) Hammer, B.; Norskov, J. K. *Surface Science* **1995**, *343*, 211–220.

(143) Greeley, J.; Norskov, J. K. *Surface Science* **2005**, *592*, 104–111.

(144) Stroppa, A.; Kresse, G. *New Journal of Physics* **2008**, *10*, 063020.

(145) Stroppa, A.; Mittendorfer, F. *The Journal of Physical Chemistry C* **2011**, *115*, 21320–21323.

(146) Medford, A. J.; Vojvodic, A.; HummelshÃÿj, J. S.; Voss, J.; Abild-Pedersen, F.; Studt, F.; Bligaard, T.; Nilsson, A.; NÃÿrskov, J. K. *Journal of Catalysis* **2015**, *328*, 36–42.

(147) Filot, I. A. W.; vanâĂĚSanten, R. A.; Hensen, E. J. M. *Angewandte Chemie International Edition* **2014**, *53*, 12746–12750.

(148) Busch, M.; Wodrich, M. D.; Corminboeuf, C. *Chemical Science* **2015**, *6*, 6754–6761.

(149) Rodriguez, J.; Graciani, J.; Evans, J.; Park, J.; Yang, F.; Stacchiola, D.; Senanayake, S.; Ma, S.; PÃľrez, M.; Liu, P.; Sanz, J.; Hrbek, J. *Angewandte Chemie International Edition* **2009**, *48*, 8047–8050.

(150) Yang, F.; Graciani, J.; Evans, J.; Liu, P.; Hrbek, J.; Sanz, J. F.; Rodriguez, J. A. *Journal of the American Chemical Society* **2011**, *133*, 3444–3451.

(151) Schott, V.; Oberhofer, H.; Birkner, A.; Xu, M.; Wang, Y.; Muhler, M.; Reuter, K.; WÃűll, C. *Angewandte Chemie International Edition* **2013**, *52*, 11925–11929.

(152) Kattel, S.; Yan, B.; Yang, Y.; Chen, J. G.; Liu, P. *Journal of the American Chemical Society* **2016**, *138*, 12440–12450.

(153) Reichenbach, T.; Mondal, K.; Jager, M.; Vent-Schmidt, T.; Himmel, D.; Dybbert, V.; Bruix, A.; Krossing, I.; Walter, M.; Moseler, M. *Journal of Catalysis* **2018**, *360*, 168–174.

(154) Huber, B.; Koskinen, P.; Hakkinen, H.; Moseler, M. *Nature Materials* **2006**, *5*, 44–47.

(155) Song, W. Y.; Su, Y. Q.; Hensen, E. J. M. *Journal of Physical Chemistry C* **2015**, *119*, 27505–27511.

(156) Vayssilov, G. N.; Lykhach, Y.; Migani, A.; Staudt, T.; Petrova, G. P.; Tsud, N.; Skala, T.; Bruix, A.; Illas, F.; Prince, K. C.; Matolin, V.; Neyman, K. M.; Libuda, J. *Nature Materials* **2011**, *10*, 310–315.

(157) Kozlov, S. M.; Neyman, K. M. *Journal of catalysis* **2016**, *344*, 507–514.

(158) Sun, D.; Gu, X.-K.; Ouyang, R.; Su, H.-Y.; Fu, Q.; Bao, X.; Li, W.-X. *The Journal of Physical Chemistry C* **2012**, *116*, 7491–7498.

(159) Pan, Q.; Weng, X.; Chen, M.; Giordano, L.; Pacchioni, G.; Noguera, C.; Goniakowski, J.; Shaikhutdinov, S.; Freund, H.-J. *ChemCatChem* **2015**, *7*, 2620–2627.

(160) Vandichel, M.; Gronbeck, H. *Topics in Catalysis* **2018**, *61*, 1458–1464.

(161) Vandichel, M.; Gronbeck, H. *Catal. Sci. Technol.* **2019**, *published online, DOI:10.1039/c8cy01989d*.

(162) Michalak, W. D.; Krier, J. M.; Alayoglu, S.; Shin, J. Y.; An, K.; Komvopoulos, K.; Liu, Z.; Somorjai, G. A. *Journal of Catalysis* **2014**, *312*, 17–25.

(163) Campbell, C. T. *ACS Catalysis* **2017**, *7*, 2770–2779.

(164) Stegelmann, C.; Andreasen, A.; Campbell, C. T. *Journal of the American Chemical Society* **2009**, *131*, 8077–8082.

(165) Campbell, C. T. *Topics in Catalysis* **1994**, *1*, 353–366.

(166) Jorgensen, M.; Gronbeck, H. *Catal. Sci. Technol.* **2017**, *7*, 4034–4040.

(167) Dietze, E. M.; Abild-Pedersen, F.; Plessow, P. N. *The Journal of Physical Chemistry C* **2018**, *122*, 26563–26569.

(168) Groß, A. *Top. Curr. Chem.* **2018**, *376*, 17.

(169) Xu, W.; Wang, J.; Ding, F.; Chen, X.; Nasybulin, E.; Zhang, Y.; Zhang, J.-G. *Energy Environ. Sci.* **2014**, *7*, 513–537.

(170) Wu, F.; Yuan, Y.-X.; Cheng, X.-B.; Bai, Y.; Li, Y.; Wu, C.; Zhang, Q. *Energy Storage Mater.* **2018**, *15*, 148 – 170.

(171) Medenbach, L.; Bender, C. L.; Haas, R.; Mogwitz, B.; Pompe, C.; Adelhelm, P.; Schröder, D.; Janek, J. *Energy Technol.* **2017**, *5*, 2265–2274.

(172) Aurbach, D.; Cohen, Y.; Moshkovich, M. *Electrochem. Solid-State Lett.* **2001**, *4*, A113.

(173) Jäckle, M.; Groß, A. *J. Chem. Phys.* **2014**, *141*, 174710.

(174) Steiger, J.; Richter, G.; Wenk, M.; Kramer, D.; Mönig, R. *Electrochem. Comm.* **2015**, *50*, 11 – 14.

(175) Ehrlich, G.; Hudda, F. G. *J. Chem. Phys.* **1966**, *44*, 1039.

(176) Schwoebel, R. L.; Shipsey, E. J. *J. Appl. Phys.* **1966**, *37*, 3682.

(177) Jäckle, M.; Helmbrecht, K.; Smits, M.; Stottmeister, D.; Groß, A. *Energy Environ. Sci.* **2018**, *11*, 3400–3407.

(178) Elia, G. A.; Marquardt, K.; Hoeppner, K.; Fantini, S.; Lin, R.; Knipping, E.; Peters, W.; Drillet, J.-F.; Passerini, S.; Hahn, R. *Adv. Mater.* **2016**, *28*, 7564–7579.

(179) Parker, J. F.; Chervin, C. N.; Nelson, E. S.; Rolison, D. R.; Long, J. W. *Energy Environ. Sci.* **2014**, *7*, 1117–1124.

(180) Parker, J. F.; Chervin, C. N.; Pala, I. R.; Machler, M.; Burz, M. F.; Long, J. W.; Rolison, D. R. *Science* **2017**, *356*, 415–418.

(181) Lin, X.; Dasgupta, A.; Xie, F.; Schimmel, T.; Evers, F.; Groß, A. *Electrochim. Acta* **2014**, *140*, 505–510.

(182) Wang, K.; Pei, P.; Ma, Z.; Chen, H.; Xu, H.; Chen, D.; Wang, X. *J. Mater. Chem. A* **2015**, *3*, 22648 – 22655.

(183) Davidson, R.; Verma, A.; Santos, D.; Hao, F.; Fincher, C.; Xiang, S.; Van Buskirk, J.; Xie, K.; Pharr, M.; Mukherjee, P.; Banerjee, S. *ACS Energy Lett.* **2019**, *4*, 375–376.

(184) Gaissmaier, D.; Fantauzzi, D.; Jacob, T. *J. Chem. Phys.* **2019**, *150*, 041723.

(185) Magnussen, O. M.; Groß, A. *J. Am. Chem. Soc.* **2019**, *141*, 4777–4790.

(186) *Coordination Chemistry Reviews* **2018**, *373*, 233 – 257, Coordination Chemistry for Energy.

(187) *Coordination Chemistry Reviews* **2006**, *250*, 2093 – 2126.

(188) *Bull. Chem. Soc. Jpn.* **2007**, *80*, 287 – 294.

(189) Jain, A.; Ong, S. P.; Hautier, G.; Chen, W.; Richards, W. D.; Dacek, S.; Cholia, S.; Gunter, D.; Skinner, D.; Ceder, G.; Persson, K. A. *APL Materials* **2013**, *1*, 011002.

(190) Williams, J. A. G.; Beeby, A.; Davies, E. S.; Weinstein, J. A.; Wilson, C. *Inorganic Chemistry* **2003**, *42*, 8609–8611.

(191) Williams, J. A. G. *Chem. Soc. Rev.* **2009**, *38*, 1783–1801.

(192) Fuertes, S.; Brayshaw, S. K.; Raithby, P. R.; Schiffers, S.; Warren, M. R. *Organometallics* **2012**, *31*, 105–119.

(193) Botchway, S. W.; Charnley, M.; Haycock, J. W.; Parker, A. W.; Rochester, D. L.; Weinstein, J. A.; Williams, J. A. G. *Proceedings of the National Academy of Sciences* **2008**, *105*, 16071–16076.

(194) Grove, L. J.; Rennekamp, J. M.; Jude, H.; Connick, W. B. *Journal of the American Chemical Society* **2004**, *126*, 1594–1595.

(195) Bryant, M. J. et al. *Nature Communications* **2017**, *8*, 1800.

(196) Wadas, T. J.; Wang, Q.-M.; Kim, Y.-j.; Flaschenreim, C.; Blanton, T. N.; Eisenberg, R. *Journal of the American Chemical Society* **2004**, *126*, 16841–16849.

(197) Kui, S. C. F.; Chui, S. S.-Y.; Che, C.-M.; Zhu, N. *Journal of the American Chemical Society* **2006**, *128*, 8297–8309.

(198) Albrecht, M.; Lutz, M.; Spek, A. L.; van Koten, G. *Nature* **2000**, *406*, 970 EP –.

(199) Grove, L. J.; Oliver, A. G.; Krause, J. A.; Connick, W. B. *Inorganic Chemistry* **2008**, *47*, 1408–1410.

(200) Murmann, R. K.; Taube, H. *Journal of the American Chemical Society* **1956**, *78*, 4886–4890.

(201) Penland, R. B.; Lane, T. J.; Quagliano, J. V. *Journal of the American Chemical Society* **1956**, *78*, 887–889.

(202) Grove, L. J.; Oliver, A. G.; Krause, J. A.; Connick, W. B. *Zeitschrift für anorganische und allgemeine Chemie 279*, 219–224.

(203) Svendsen, H.; Overgaard, J.; Chevallier, M.; Collet, E.; Iversen, B. *Angewandte Chemie 121*, 2818–2821.

(204) Zhang, J.; Zou, Q.; Tian, H. *Advanced Materials 25*, 378–399.

(205) Sylvester, S. O.; Cole, J. M. *Advanced Materials 25*, 3324–3328.

(206) Carducci, M. D.; Pressprich, M. R.; Coppens, P. *Journal of the American Chemical Society* **1997**, *119*, 2669–2678.

(207) *Coordination Chemistry Reviews* **2014**, *277-278*, 69 – 79, Following Chemical Structures using Synchrotron Radiation.

(208) Hatcher, L. E.; Christensen, J.; Hamilton, M. L.; Trincao, J.; Allan, D. R.; Warren, M. R.; Clarke, I. P.; Towrie, M.; Fuertes, D. S.; Wilson, C. C.; Woodall, C. H.; Raithby, P. R. *Chemistry âĂŞ A European Journal 20*, 3128–3134.

(209) Warren, M. R.; Easun, T. L.; Brayshaw, S. K.; Deeth, R. J.; George, M. W.; Johnson, A. L.; Schiffers, S.; Teat, S. J.; Warren, A. J.; Warren, J. E.; Wilson, C. C.; Woodall, C. H.; Raithby, P. R. *Chemistry âĂŞ A European Journal 20*, 5468–5477.

(210) Hatcher, L. E.; Bigos, E. J.; Bryant, M. J.; MacCready, E. M.; Robinson, T. P.; Saunders, L. K.; Thomas, L. H.; Beavers, C. M.; Teat, S. J.; Christensen, J.; Raithby, P. R. *CrystEngComm* **2014**, *16*, 8263–8271.

(211) Bowes, K. F.; Cole, J. M.; Husheer, S. L. G.; Raithby, P. R.; Savarese, T. L.; Sparkes, H. A.; Teat, S. J.; Warren, J. E. *Chem. Commun.* **2006**, 2448–2450.

(212) Sylvester, S. O.; Cole, J. M. *The Journal of Physical Chemistry Letters* **2013**, *4*, 3221–3226.

(213) *Tetrahedron* **2000**, *56*, 6813 – 6820.

(214) Warren, M.; Brayshaw, S.; Johnson, A.; Schiffers, S.; Raithby, P.; Easun, T.; George, M.; Warren, J.; Teat, S. *Angewandte Chemie 121*, 5821–5824.

(215) Hatcher, L. E. *CrystEngComm* **2016**, *18*, 4180–4187.

(216) Skelton, J. M.; Crespo-Otero, R.; Hatcher, L. E.; Parker, S. C.; Raithby, P. R.; Walsh, A. *CrystEngComm* **2015**, *17*, 383–394.

(217) Skelton, J. M.; Lora da Silva, E.; Crespo-Otero, R.; Hatcher, L. E.; Raithby, P. R.; Parker, S. C.; Walsh, A. *Faraday Discuss.* **2015**, *177*, 181–202.

(218) Hatcher, L. E.; Skelton, J. M.; Warren, M. R.; Stubbs, C.; da Silva, E. L.; Raithby, P. R. *Phys. Chem. Chem. Phys.* **2018**, *20*, 5874–5886.

(219) Casaretto, N.; Schaniel, D.; Alle, P.; Wenger, E.; Parois, P.; Fournier, B.; Bendeif, E.-E.; Palin, C.; Pillet, S. *Acta Crystallographica Section B* **2017**, *73*, 696–707.

(220) Chater, J. **2004**, A history of nuclear power.

(221) IEA, *World Energy Outlook 2018*; IEA, Paris, 2018, DOI: https://doi.org/10.1787/weo-2018-en.

(222) Goldberg, S. M.; Rosner, R. *Nuclear Reactors: Generation to Generation*; American Academy of Arts and Sciences, 2011.

(223) *GIF R&D Outlook for Generation IV Nuclear Energy Systems*; GIF, 21 August 2009.

(224) Carpenter, G. J. C.; Watters, J. F. *Acta Metallurgica* **1973**, *21*, 1207 – 1214.

(225) Griffiths, M. *J NUCL MATER* **1988**, *159*, 190 – 218.

(226) Onimus, F.; Béchade, J. L. In *Comprehensive Nuclear Materials*; Konings, R. J., Ed.; Elsevier: Oxford, 2012; pp 1 – 31.

(227) Becquart, C. S.; Domain, C. *Phys. Rev. Lett.* **2006**, *97*, 196402.

(228) Zinkle, S. In *Structural Materials for Generation IV Nuclear Reactors*; Yvon, P., Ed.; Woodhead Publishing, 2017; pp 569 – 594.

(229) Beyerlein, I. J.; Demkowicz, M. J.; Misra, A.; Uberuaga, B. P. *Progress in Materials Science* **2015**, *74*, 125 – 210.

(230) Demkowicz, M. J.; Misra, A.; Caro, A. *Current Opinion in Solid State and Materials Science* **2012**, *16*, 101 – 108.

(231) Bai, X.-M.; Voter, A. F.; Hoagland, R. G.; Nastasi, M.; Uberuaga, B. P. *Science* **2010**, *327*, 1631–1634.

(232) Demkowicz, M. J.; Hoagland, R. G.; Hirth, J. *Phys. Rev. Lett.* **2008**, *100*, 136102.

(233) Saikia, U.; Sahariah, M. B.; González, C.; Pandey, R. *Scientific Reports* **2018**, *8*, 3884.

(234) Kolluri, K.; Demkowicz, M. J. *Phys. Rev. B* **2012**, *85*.

(235) Kolluri, K.; Liu, X.-Y.; G. Hoagland, R.; J. Demkowicz, M. *JOM* **2013**, *65*.

(236) González, C.; Iglesias, R.; J. Demkowicz, M. *Phys. Rev. B* **2015**, *91*, 064103.

(237) Metsanurk, E.; Caro, A.; Tamm, A.; Aabloo, A.; Klintenberg, M. *Scientific reports* **2014**, *4*.

(238) Metsanurk, E.; Tamm, A.; Aabloo, A.; Klintenberg, M.; Caro, A. *Modelling and Simulation in Materials Science and Engineering* **2017**, *25*, 025012.

(239) Demkowicz, M.; Thilly, L. *Acta Materialia* **2011**, *59*, 7744 – 7756.

(240) Liu, X.-Y.; Uberuaga, B.; J. Demkowicz, M.; Germann, T.; Misra, A.; Nastasi, M. *Physical Review B* **2012**, *85*, 012103.

(241) Snel, J.; Monclús, M. A.; Castillo-Rodríguez, M.; Mara, N.; Beyerlein, I. J.; Llorca, J.; Molina-Aldareguía, J. M. *JOM* **2017**, *69*, 2214–2226.

(242) Economy, D. R.; Schultz, B. M.; Kennedy, M. S. *Journal of Materials Science* **2012**, *47*, 6986–6991.

(243) Zhang, J.; Zhang, P.; Zhang, X.; Wang, R.; Liu, G.; Zhang, G.; Sun, J. *Materials Science and Engineering: A* **2012**, *545*, 118 – 122.

(244) Sen, H. S.; Polcar, T. *Journal of Nuclear Materials under review*.

(245) Demkowicz, M. J.; Hoagland, R. G.; Uberuaga, B. P.; Misra, A. *Phys. Rev. B* **2011**, *84*, 104102.

(246) Li, N.; J. Demkowicz, M.; A. Mara, N. *JOM* **2017**, *69*.

(247) Demkowicz, M. J.; Wang, Y. Q.; Hoagland, R. G.; Anderoglu, O. *Nuclear Instruments and Methods in Physics Research Section B: Beam Interactions with Materials and Atoms* **2007**, *261*, 524 – 528.

(248) Zhang, X.; Li, N.; Anderoglu, O.; Wang, H.; Swadener, G.; HÃűchbauer, T.; Misra, A.; G. Hoagland, R. *Nuclear Instruments and Methods in Physics Research Section B: Beam Interactions with Materials and Atoms* **2007**, *261*, 1129–1132.

(249) Dunn, A.; McPhie, M.; Capolungo, L.; Martinez, E.; Cherkaoui, M. *Journal of Nuclear Materials* **2013**, *435*, 141 – 152.

(250) Chen, D.; Li, N.; Yuryev, D.; Kevin Baldwin, J.; Wang, Y.; J. Demkowicz, M. *Science Advances* **2017**, *3*, eaao2710.

(251) Bhattacharyya, D.; Demkowicz, M.; Wang, Y.-Q.; Baumer, R.; Nastasi, M.; Misra, A. *Microscopy and Microanalysis* **2012**, *18*, 152âĂŞ161.

(252) Hattar, K.; Demkowicz, M.; Misra, A.; Robertson, I.; Hoagland, R. *Scripta Materialia - SCRIPTA MATER* **2008**, *58*, 541–544.

(253) González, C.; Iglesias, R. *Materials & Design* **2016**, *91*, 171–179.

(254) Callisti, M.; Karlik, M.; Polcar, T. *Journal of Nuclear Materials* **2016**, *473*, 18 – 27.

(255) Chen, S.; Liu, B.; Lin, L.; Jiao, G. *Nuclear Instruments and Methods in Physics Research Section B: Beam Interactions with Materials and Atoms* **2015**, *354*, 244 – 248, 26th International Conference on Atomic Collisions in Solids.

(256) Pacaud, J.; Jaouen, C.; Gladyszewski, G. *Journal of Applied Physics* **1999**, *86*, 4847–4854.

(257) Nelasov, I. V.; Lipnitskii, A. G. *St. Petersburg Polytechnical University Journal: Physics and Mathematics* **2016**, *2*, 91 – 95.

(258) Woldt, E.; Jensen, D. J. *Metallurgical and Materials Transactions A* **1995**, *26*, 1717–1724.

(259) Benchabane, G.; Boumerzoug, Z.; Thibon, I.; Gloriant, T. *Materials Characterization* **2008**, *59*, 1425 – 1428.

(260) Monclús, M. A.; Zheng, S. J.; Mayeur, J. R.; Beyerlein, I. J.; Mara, N. A.; Polcar, T.; Llorca, J.; Molina-Aldareguía, J. M. *APL Materials* **2013**, *1*, 052103.

(261) Primorac, M.-M.; Abad, M. D.; Hosemann, P.; Kreuzeder, M.; Maier, V.; Kiener, D. *Materials Science and Engineering: A* **2015**, *625*, 296 – 302.

(262) Monclús, M. A.; Karlik, M.; Callisti, M.; Frutos, E.; LLorca, J.; Polcar, T.; Molina-Aldareguía, J. M. *Thin Solid Films* **2014**, *571*, 275 – 282, Multilayers 2013.

(263) Monclús, M. A.; Callisti, M.; Polcar, T.; Yang, L. W.; Molina-Aldareguía, J. M.; LLorca, J. *Journal of Materials Science* **2018**, *53*, 5860–5878.

(264) Callisti, M.; Polcar, T. *Acta Materialia* **2017**, *124*, 247 – 260.

(265) Callisti, M.; Lozano-Perez, S.; Polcar, T. *Materials Letters* **2016**, *163*, 138 – 141.

(266) Callisti, M.; Karlik, M.; Polcar, T. *Scripta Materialia* **2018**, *152*, 31 – 35.

(267) Rodgers, D.; Griffiths, M.; Bickel, G.; Buyers, A.; Coleman, C.; Nordin, H.; Lawrence, S. *CNL Nuclear Review* **2016**, *5*, 1–15.

(268) Lu, Y.; Kotoka, R.; Ligda, J.; Cao, B.; Yarmolenko, S.; Schuster, B.; Wei, Q. *Acta Materialia* **2014**, *63*, 216 – 231.

(269) Lu, Y.; Kotoka, R.; Ligda, J.; Cao, B.; Yarmolenko, S.; Schuster, B.; Wei, Q. *Acta Materialia* **2014**, *63*, 216 – 231.

(270) He, J.; Liu, Y.; Funahashi, R. *J. Mater. Res.* **2011**, *26*, 1762–1772.

(271) Hébert, S.; Maignan, A. In *Functional Oxides*; Bruce, D. W., O'Hare, D., Walton, R. I., Eds.; John Wiley & Sons, Ltd., Chichester, UK, 2010.

(272) Puggioni, D.; Rondinelli, J. M. *Nat. Commun.* **2014**, *5*, 3432.

(273) Gorai, P.; Stevanovic, V.; Toberer, E. *Nat. Rev. Mater.* **2017**, *2*, 17053.

(274) Xing, G.; Sun, J.; Ong, K. P.; Fan, X.; Zheng, W.; Singh, D. J. *APL Mater.* **2016**, *4*, 053201.

(275) Garrity, K. F. *Phys. Rev. B* **2016**, *94*, 045122.

(276) Lamontagne, L. K.; Laurita, G.; Gaultois, M. W.; Knight, M.; Ghadbeigi, L.; Sparks, T. D.; Gruner, M. E.; Pentcheva, R.; Brown, C. M.; Seshadri, R. *Chem. Mat.* **2016**, *28*, 3367–3373.

(277) Okuda, T.; Nakanishi, K.; Miyasaka, S.; Tokura, Y. *Phys. Rev. B* **2001**, *63*, 113104.

(278) Jalan, B.; Stemmer, S. *Appl. Phys. Lett.* **2010**, *97*, 042106.

(279) Cain, T. A.; Kajdos, A. P.; Stemmer, S. *Appl. Phys. Lett.* **2013**, *102*, 182101.

(280) Gruner, M. E.; Eckern, U.; Pentcheva, R. *Phys. Rev. B* **2015**, *92*, 235140.

(281) Hicks, L. D.; Dresselhaus, M. S. *Phys. Rev. B* **1993**, *47*, 12727–12731.

(282) Mao, J.; Liu, Z.; Ren, Z. *npj Quantum Mater.* **2016**, *1*, 16028.

(283) Ohta, H.; Kim, S.; Mune, Y.; Mizoguchi, T.; Nomura, K.; Ohta, S.; Nomura, T.; Nakanishi, Y.; Ikuhara, Y.; Hirano, M.; Hosono, H.; Koumoto, K. *Nat. Mater.* **2007**, *6*, 129.

(284) Filippetti, A.; Delugas, P.; Verstraete, M. J.; Pallecchi, I.; Gadaleta, A.; Marré, D.; Li, D. F.; Gariglio, S.; Fiorentini, V. *Phys. Rev. B* **2012**, *86*, 195301.

(285) García-Fernández, P.; Verissimo-Alves, M.; Bilc, D. I.; Ghosez, P.; Junquera, J. *Phys. Rev. B* **2012**, *86*, 085305.

(286) Delugas, P.; Filippetti, A.; Verstraete, M. J.; Pallecchi, I.; Marré, D.; Fiorentini, V. *Phys. Rev. B* **2013**, *88*, 045310.

(287) Pallecchi, I.; Telesio, F.; Li, D.; Fête, A.; Gariglio, S.; Triscone, J.-M.; Filippetti, A.; Delugas, P.; Fiorentini, V.; Marré, D. *Nat. Commun.* **2015**, *6*, 6678.

(288) Bilc, D. I.; Floare, C. G.; Zârbo, L. P.; Garabagiu, S.; Lemal, S.; Ghosez, P. *J. Phys. Chem. C* **2016**, *120*, 25678–25688.

(289) Geisler, B.; Blanca-Romero, A.; Pentcheva, R. *Phys. Rev. B* **2017**, *95*, 125301.

(290) Geisler, B.; Pentcheva, R. *Phys. Rev. Materials* **2018**, *2*, 055403.

(291) Geisler, B.; Pentcheva, R. *Phys. Rev. Applied* **2019**, *11*, 044047.

(292) Geisler, B.; Kratzer, P. *Phys. Rev. B* **2015**, *92*, 144418.

(293) Geisler, B.; Kratzer, P.; Popescu, V. *Phys. Rev. B* **2014**, *89*, 184422.

(294) Comtesse, D.; Geisler, B.; Entel, P.; Kratzer, P.; Szunyogh, L. *Phys. Rev. B* **2014**, *89*, 094410.

(295) Popescu, V. et al. *J. Phys. D: Appl. Phys.* **2018**,

(296) Middey, S.; Chakhalian, J.; Mahadevan, P.; Freeland, J.; Millis, A.; Sarma, D. *Annu. Rev. Mater. Res.* **2016**, *46*, 305–334.

(297) Lorenz, M. et al. *J. Phys. D: Appl. Phys.* **2016**, *49*, 433001.

(298) Wrobel, F.; Geisler, B.; Wang, Y.; Christiani, G.; Logvenov, G.; Bluschke, M.; Schierle, E.; van Aken, P. A.; Keimer, B.; Pentcheva, R.; Benckiser, E. *Phys. Rev. Materials* **2018**, *2*, 035001.

(299) Liu, J.; Okamoto, S.; van Veenendaal, M.; Kareev, M.; Gray, B.; Ryan, P.; Freeland, J. W.; Chakhalian, J. *Phys. Rev. B* **2011**, *83*, 161102.

(300) Son, J.; LeBeau, J. M.; Allen, S. J.; Stemmer, S. *Appl. Phys. Lett.* **2010**, *97*, 202109.

(301) Kaiser, A. M.; Gray, A. X.; Conti, G.; Son, J.; Greer, A.; Perona, A.; Rattanachata, A.; Saw, A. Y.; Bostwick, A.; Yang, S.; Yang, S.-H.; Gullikson, E. M.; Kortright, J. B.; Stemmer, S.; Fadley, C. S. *Phys. Rev. Lett.* **2011**, *107*, 116402.

(302) Hwang, J.; Son, J.; Zhang, J. Y.; Janotti, A.; Van de Walle, C. G.; Stemmer, S. *Phys. Rev. B* **2013**, *87*, 060101.

(303) Wrobel, F.; Mark, A. F.; Christiani, G.; Sigle, W.; Habermeier, H.-U.; van Aken, P. A.; Logvenov, G.; Keimer, B.; Benckiser, E. *Appl. Phys. Lett.* **2017**, *110*, 041606.

(304) Kaya, P.; Gregori, G.; Baiutti, F.; Yordanov, P.; Suyolcu, Y. E.; Cristiani, G.; Wrobel, F.; Benckiser, E.; Keimer, B.; van Aken, P. A.; Habermeier, H.-U.; Logvenov, G.; Maier, J. *ACS Appl. Mater. Interfaces* **2018**, *10*, 22786–22792.

(305) Pardo, V.; Botana, A. S.; Baldomir, D. *Phys. Rev. B* **2012**, *86*, 165114.

(306) Noguera, C. *J. Phys.: Condens. Matter* **2000**, *12*, R367.

(307) Nakagawa, N.; Hwang, H. Y.; Muller, D. A. *Nat. Mater.* **2006**, *5*, 204.

(308) Pentcheva, R.; Pickett, W. E. *Phys. Rev. B* **2006**, *74*, 035112.

(309) Botana, A. S.; Pardo, V.; Pickett, W. E. *Phys. Rev. Applied* **2017**, *7*, 024002.

(310) Harrison, W. A.; Kraut, E. A.; Waldrop, J. R.; Grant, R. W. *Phys. Rev. B* **1978**, *18*, 4402–4410.

(311) Blanca-Romero, A.; Pentcheva, R. *Phys. Rev. B* **2011**, *84*, 195450.

(312) Freeland, J. W.; Liu, J.; Kareev, M.; Gray, B.; Kim, J. W.; Ryan, P.; Pentcheva, R.; Chakhalian, J. *Europhys. Lett.* **2011**, *96*, 57004.

(313) Yordanov, P.; Wochner, P.; Ibrahimkutty, S.; Dietl, C.; Wrobel, F.; Felici, R.; Gregori, G.; Maier, J.; Keimer, B.; Habermeier, H.-U. *Appl. Phys. Lett.* **2017**, *110*, 253101.

(314) Sivan, U.; Imry, Y. *Phys. Rev. B* **1986**, *33*, 551–558.

(315) Mahan, G. D.; Sofo, J. O. *Proc. Natl. Acad. Sci. USA* **1996**, *93*, 7436–7439.

(316) Nakpathomkun, N.; Xu, H. Q.; Linke, H. *Phys. Rev. B* **2010**, *82*, 235428.

(317) Jordan, A. N.; Sothmann, B.; Sánchez, R.; Büttiker, M. *Phys. Rev. B* **2013**, *87*, 075312.

(318) Han, M. J.; Marianetti, C. A.; Millis, A. J. *Phys. Rev. B* **2010**, *82*, 134408.

(319) Wu, M. et al. *Phys. Rev. B* **2013**, *88*, 125124.

(320) Doennig, D.; Pickett, W. E.; Pentcheva, R. *Phys. Rev. B* **2014**, *89*, 121110.

(321) Disa, A. S.; Kumah, D. P.; Malashevich, A.; Chen, H.; Arena, D. A.; Specht, E. D.; Ismail-Beigi, S.; Walker, F. J.; Ahn, C. H. *Phys. Rev. Lett.* **2015**, *114*, 026801.

(322) Bernardi, M.; Vigil-Fowler, D.; Lischner, J.; Neaton, J. B.; Louie, S. G. *Phys. Rev. Lett.* **2014**, *112*, 257402.

(323) Mustafa, J. I.; Bernardi, M.; Neaton, J. B.; Louie, S. G. *Phys. Rev. B* **2016**, *94*, 155105.

(324) Dekura, H.; Tsuchiya, T. *Phys. Rev. B* **2017**, *95*, 184303.

(325) Zhang, J.; Bachman, M.; Czerner, M.; Heiliger, C. *Phys. Rev. Lett.* **2015**, *115*, 037203.

(326) Mizuno, H.; Mossa, S.; Barrat, J.-L. *Sci. Rep.* **2015**, *5*, 14116.

(327) O'Dwyer, C.; Chen, R.; He, J.-H.; Lee, J.; Razeeb, K. M. *ECS J. Solid State Sci. Technol.* **2017**, *6*, N3058.

(328) Katsufuji, T.; Saiki, T.; Okubo, S.; Katayama, Y.; Ueno, K. *Phys. Rev. Materials* **2018**, *2*, 051002.

(329) Ravichandran, J. et al. *Nat. Mater.* **2013**, *13*, 168.

(330) Luckyanova, M. N.; Garg, J.; Esfarjani, K.; Jandl, A.; Bulsara, M. T.; Schmidt, A. J.; Minnich, A. J.; Chen, S.; Dresselhaus, M. S.; Ren, Z.; Fitzgerald, E. A.; Chen, G. *Science* **2012**, *338*, 936–939.

(331) Garg, J.; Bonini, N.; Marzari, N. *Nano Lett.* **2011**, *11*, 5135–5141.

(332) Zhao, H. J.; Filippetti, A.; Escorihuela-Sayalero, C.; Delugas, P.; Canadell, E.; Bellaiche, L.; Fiorentini, V.; Íñiguez, J. *Phys. Rev. B* **2018**, *97*, 054107.

(333) Filippetti, A.; Fiorentini, V.; Ricci, F.; Delugas, P.; Íñiguez, J. *Nature Communications* **2016**, *7*, 11211 EP –.

(334) Urru, A.; Filippetti, A.; Ricci, F.; Íñiguez, J.; Fiorentini, V. *to be published.*

(335) Anderson, P. W.; Blount, E. I. *Phys. Rev. Lett.* **1965**, *14*, 217–219.

(336) Padmanabhan, H.; Park, Y.; Puggioni, D.; Yuan, Y.; Cao, Y.; Gasparov, L.; Shi, Y.; Chakhalian, J.; Rondinelli, J. M.; Gopalan, V. *Applied Physics Letters* **2018**, *113*, 122906.

(337) Puggioni, D.; Giovannetti, G.; Capone, M.; Rondinelli, J. M. *Phys. Rev. Lett.* **2015**, *115*, 087202.

(338) Puggioni, D.; Rondinelli, J. M. *Nature Communications* **2014**, *5*, 3432 EP –.

(339) Benedek, N. A.; Birol, T. *J. Mater. Chem. C* **2016**, *4*, 4000–4015.

(340) Scarrozza, M.; Filippetti, A.; Fiorentini, V. *Phys. Rev. Lett.* **2012**, *109*, 217202.

(341) López-Pérez, J.; Íñiguez, J. *Phys. Rev. B* **2011**, *84*, 075121.

(342) Vanderbilt, D. *Berry Phases in Electronic Structure Theory*; Cambridge University Press, 2018.

(343) Park, S. J.; Kim, T. Y.; Park, C.-H.; Kim, D.-S. *Scientific Reports* **2016**, *6*, 22981 EP –.

(344) Garrity, K. F.; Rabe, K. M.; Vanderbilt, D. *Phys. Rev. Lett.* **2014**, *112*, 127601.

(345) Puggioni, D.; Stroppa, A.; Rondinelli, J. M. *Phys. Rev. Materials* **2018**, *2*, 114403.

(346) Rao, C.; Cheetham, A.; Thirumurugan, A. *Journal of Physics: Condensed Matter* **2008**, *20*, 083202.

(347) Wenk, H.-R.; Bulakh, A. *Minerals: their constitution and origin*; Cambridge University Press, 2016.

(348) Jain, P.; Ramachandran, V.; Clark, R. J.; Zhou, H. D.; Toby, B. H.; Dalal, N. S.; Kroto, H. W.; Cheetham, A. K. *Journal of the American Chemical Society* **2009**, *131*, 13625–13627.

(349) Besara, T.; Jain, P.; Dalal, N. S.; Kuhns, P. L.; Reyes, A. P.; Kroto, H. W.; Cheetham, A. K. *Proceedings of the National Academy of Sciences* **2011**,

(350) Ramesh, R. *Nature* **2009**, *461*, 1218.

(351) Kieslich, G.; Sun, S.; Cheetham, A. K. *Chemical science* **2015**, *6*, 3430–3433.

(352) Kieslich, G.; Sun, S.; Cheetham, A. K. *Chemical Science* **2014**, *5*, 4712–4715.

(353) Hu, K.-L.; Kurmoo, M.; Wang, Z.; Gao, S. *Chemistry–A European Journal* **2009**, *15*, 12050–12064.

(354) Stroppa, A.; Jain, P.; Barone, P.; Marsman, M.; Perez-Mato, J. M.; Cheetham, A. K.; Kroto, H. W.; Picozzi, S. *Angewandte Chemie International Edition* **2011**, *50*, 5847–5850.

(355) Ghosh, S.; Di Sante, D.; Stroppa, A. *The journal of physical chemistry letters* **2015**, *6*, 4553–4559.

(356) Stroppa, A.; Barone, P.; Jain, P.; Perez-Mato, J. M.; Picozzi, S. *Advanced Materials* **2013**, *25*, 2284–2290.

(357) Tian, Y.; Stroppa, A.; Chai, Y.; Yan, L.; Wang, S.; Barone, P.; Picozzi, S.; Sun, Y. *Scientific reports* **2014**, *4*, 6062.

(358) Stroppa, A.; Di Sante, D.; Barone, P.; Bokdam, M.; Kresse, G.; Franchini, C.; Whangbo, M.-H.; Picozzi, S. *Nature communications* **2014**, *5*, 5900.

(359) Di Sante, D.; Stroppa, A.; Jain, P.; Picozzi, S. *Journal of the American Chemical Society* **2013**, *135*, 18126–18130.

(360) Mazzuca, L.; CanÌČadillas-Delgado, L.; Rodríguez-VelamazaÌĄn, J. A.; Fabelo, O.; Scarrozza, M.; Stroppa, A.; Picozzi, S.; Zhao, J.-P.; Bu, X.-H.; Rodríguez-Carvajal, J. *Inorganic chemistry* **2016**, *56*, 197–207.

(361) Kamminga, M. E.; Stroppa, A.; Picozzi, S.; Chislov, M.; Zvereva, I. A.; Baas, J.; Meetsma, A.; Blake, G. R.; Palstra, T. T. *Inorganic chemistry* **2016**, *56*, 33–41.

(362) Gómez-Aguirre, L.; Pato-Doldán, B.; Stroppa, A.; Yang, L.; Frauenheim, T.; Mira, J.; Yáñez-Vilar, S.; Artiaga, R.; Castro-García, S.; Sánchez-Andújar, M.; Señaris Rodríguez, M. *Chemistry — A European Journal* **2016**, *22*, 7863–7870.

(363) Ptak, M.; Mączka, M.; Gągor, A.; Sieradzki, A.; Stroppa, A.; Di Sante, D.; Perez-Mato, J. M.; Macalik, L. *Dalton transactions* **2016**, *45*, 2574–2583.

(364) Zhao, W.-P.; Shi, C.; Stroppa, A.; Di Sante, D.; Cimpoesu, F.; Zhang, W. *Inorganic chemistry* **2016**, *55*, 10337–10342.

(365) Gómez-Aguirre, L.; Pato-Doldán, B.; Stroppa, A.; Yáñez-Vilar, S.; Bayarjargal, L.; Winkler, B.; Castro-García, S.; Mira, J.; Sánchez-Andújar, M.; Señarís-Rodríguez, M. *Inorganic chemistry* **2015**, *54*, 2109–2116.

(366) Stroppa, A.; Quarti, C.; De Angelis, F.; Picozzi, S. *The journal of physical chemistry letters* **2015**, *6*, 2223–2231.

(367) Tian, Y.; Stroppa, A.; Chai, Y.-S.; Barone, P.; Perez-Mato, M.; Picozzi, S.; Sun, Y. *physica status solidi (RRL)–Rapid Research Letters* **2015**, *9*, 62–67.

(368) Lee, C.; Hong, J.; Stroppa, A.; Whangbo, M.-H.; Shim, J. H. *RSC Advances* **2015**, *5*, 78701–78707.

(369) Lee, M. M.; Teuscher, J.; Miyasaka, T.; Murakami, T. N.; Snaith, H. J. *Science* **2012**, 1228604.

(370) Kim, H.-S.; Lee, C.-R.; Im, J.-H.; Lee, K.-B.; Moehl, T.; Marchioro, A.; Moon, S.-J.; Humphry-Baker, R.; Yum, J.-H.; Moser, J. E.; Grätzel, M.; Park, N.-G. *Scientific Reports* **2012**, *2*, 591 EP –.

(371) Docampo, P.; Ball, J. M.; Darwich, M.; Eperon, G. E.; Snaith, H. J. *Nature communications* **2013**, *4*, 2761.

(372) Burschka, J.; Pellet, N.; Moon, S.-J.; Humphry-Baker, R.; Gao, P.; Nazeeruddin, M. K.; Grätzel, M. *Nature* **2013**, *499*, 316.

(373) Liu, M.; Johnston, M. B.; Snaith, H. J. *Nature* **2013**, *501*, 395.

(374) Liu, D.; Kelly, T. L. *Nature photonics* **2014**, *8*, 133.

(375) Malinkiewicz, O.; Yella, A.; Lee, Y. H.; Espallargas, G. M.; Graetzel, M.; Nazeeruddin, M. K.; Bolink, H. J. *Nature Photonics* **2014**, *8*, 128.

(376) Mei, A.; Li, X.; Liu, L.; Ku, Z.; Liu, T.; Rong, Y.; Xu, M.; Hu, M.; Chen, J.; Yang, Y.; Grätzel, M.; Han, H. *Science* **2014**, *345*, 295–298.

(377) Green, M. A.; Ho-Baillie, A.; Snaith, H. J. *Nature photonics* **2014**, *8*, 506.

(378) Bellitto, C.; Bauer, E. M.; Righini, G. *Coordination Chemistry Reviews* **2015**, *289*, 123–136.

(379) Náfrádi, B.; Szirmai, P.; Spina, M.; Lee, H.; Yazyev, O.; Arakcheeva, A.; Chernyshov, D.; Gibert, M.; Forró, L.; Horváth, E. *Nature communications* **2016**, *7*, 13406.

(380) Ping, Y.; Zhang, J. Z. *The journal of physical chemistry letters* **2018**, *9*, 6103–6111.

(381) Gong, C.; Li, L.; Li, Z.; Ji, H.; Stern, A.; Xia, Y.; Cao, T.; Bao, W.; Wang, C.; Wang, Y.; Qiu, Z. Q.; Cava, R. J.; Louie, S. G.; Xia, J.; Zhang, X. *Nature* **2017**, *546*, 265 EP –.

(382) Huang, B.; Clark, G.; Navarro-Moratalla, E.; Klein, D. R.; Cheng, R.; Seyler, K. L.; Zhong, D.; Schmidgall, E.; McGuire, M. A.; Cobden, D. H.; Yao, W.; Xiao, D.; Jarillo-Herrero, P.; Xu, X. *Nature* **2017**, *546*, 270 EP –.

(383) Huang, B.; Zhang, J.-Y.; Huang, R.-K.; Chen, M.-K.; Xue, W.; Zhang, W.-X.; Zeng, M.-H.; Chen, X.-M. *Chemical Science* **2018**, *9*, 7413–7418.

(384) Pedersen, K. S. et al. *Nature Chemistry* **2018**, *10*, 1056–1061.

(385) Fiebig, M.; Lottermoser, T.; Meier, D.; Trassin, M. *Nature Reviews Materials* **2016**, *1*, 16046.

(386) Dong, S.; Liu, J.-M.; Cheong, S.-W.; Ren, Z. *Advances in Physics* **2015**, *64*, 519–626.

(387) Eerenstein, W.; Mathur, N.; Scott, J. F. *nature* **2006**, *442*, 759.

(388) Dadoenkova, Y. S.; Lyubchanskii, I. L.; Lee, Y.; Rasing, T. *IEEE Transactions on Magnetics* **2011**, *47*, 1623–1626.

(389) Prati, E. *Journal of Electromagnetic Waves and Applications* **2003**, *17*, 1177–1196.

(390) Brown Jr, W.; Shtrikman, S.; Treves, D. *Journal of Applied Physics* **1963**, *34*, 1233–1234.

(391) Fan, F.-R.; Wu, H.; Nabok, D.; Hu, S.; Ren, W.; Draxl, C.; Stroppa, A. *Journal of the American Chemical Society* **2017**, *139*, 12883–12886.

(392) Kerr, J. *The London, Edinburgh, and Dublin Philosophical Magazine and Journal of Science* **1877**, *3*, 321–343.

(393) Buschow, K. v.; Van Engen, P.; Jongebreur, R. *Journal of magnetism and magnetic materials* **1983**, *38*, 1–22.

(394) Mansuripur, M. *The physical principles of magneto-optical recording*; Cambridge University Press, 1998.

(395) Mee, C. D.; Daniel, E. D. *Technology, McGraw-Hill, New York* **1987**, 323–324.

(396) Waser, R.; Keller, H.; Erb, U. *MRS BULLETIN* **2004**,

(397) Schmidt, F.; Rave, W.; Hubert, A. *IEEE Transactions on Magnetics* **1985**, *21*, 1596–1598.

(398) Stroppa, A.; Picozzi, S.; Continenza, A.; Kim, M.; Freeman, A. J. *Physical Review B* **2008**, *77*, 035208.

(399) Feng, W.; Guo, G.-Y.; Zhou, J.; Yao, Y.; Niu, Q. *Physical Review B* **2015**, *92*, 144426.

(400) Sivadas, N.; Okamoto, S.; Xiao, D. *Physical review letters* **2016**, *117*, 267203.

(401) Sangalli, D.; Marini, A.; Debernardi, A. *Physical Review B* **2012**, *86*, 125139.

(402) Eremenko, V. V.; Kharchenko, N.; Litvinenko, Y. G.; Naumenko, V. *Magneto-optics and Spectroscopy of Antiferromagnets*; Springer Science & Business Media, 2012.

(403) Jungwirth, T.; Marti, X.; Wadley, P.; Wunderlich, J. *Nature nanotechnology* **2016**, *11*, 231.

(404) Baltz, V.; Manchon, A.; Tsoi, M.; Moriyama, T.; Ono, T.; Tserkovnyak, Y. *Reviews of Modern Physics* **2018**, *90*, 015005.

(405) Jungwirth, T.; Sinova, J.; Manchon, A.; Marti, X.; Wunderlich, J.; Felser, C. *Nature Physics* **2018**, *14*, 200.

(406) Šmejkal, L.; Mokrousov, Y.; Yan, B.; MacDonald, A. H. *Nature Physics* **2018**, 1.

(407) Bodnar, S. Y.; Šmejkal, L.; Turek, I.; Jungwirth, T.; Gomonay, O.; Sinova, J.; Sapozhnik, A.; Elmers, H.-J.; Kläui, M.; Jourdan, M. *Nature Communications* **2018**, *9*, 348.

(408) Němec, P.; Fiebig, M.; Kampfrath, T.; Kimel, A. V. *Nature Physics* **2018**, 1.

(409) Wadley, P. et al. *Science* **2016**, *351*, 587–590.

(410) Godinho, J.; Reichlova, H.; Kriegner, D.; Novak, V.; Olejnik, K.; Kaspar, Z.; Soban, Z.; Wadley, P.; Campion, R. P.; Otxoa, R. M.; Roy, P. E.; Zelezny, J.; Jungwirth, T.; Wunderlich, J. *NATURE COMMUNICATIONS* **2018**, *9*.

(411) Haldane, F. D. M. *Reviews of Modern Physics* **2017**, *89*, 040502.

(412) DC, M.; Grassi, R.; Chen, J.-Y.; Jamali, M.; Reifsnyder Hickey, D.; Zhang, D.; Zhao, Z.; Li, H.; Quarterman, P.; Lv, Y.; Li, M.; Manchon, A.; Mkhoyan, K. A.; Low, T.; Wang, J.-P. *Nature Materials* **2018**, *17*, 800–807.

(413) Li, P.; Wu, W.; Wen, Y.; Zhang, C.; Zhang, J.; Zhang, S.; Yu, Z.; Yang, S. A.; Manchon, A.; Zhang, X.-x. *Nature communications* **2018**, *9*, 3990.

(414) Xing, W.; Chen, Y.; Odenthal, P. M.; Zhang, X.; Yuan, W.; Su, T.; Song, Q.; Wang, T.; Zhong, J.; Jia, S.; Xie, X. C.; Li, Y.; Han, W. *2D Materials* **2017**, *4*, 024009.

(415) Higo, T. et al. *Nature Photonics* **2018**, *12*, 73–78.

(416) Hutchings, I.; Shipway, P. *Tribology*, 2nd ed.; Butterworth-Heinemann, 2017.

(417) Holmberg, K.; Erdemir, A. *Friction* **2017**, *5*, 263–284.

(418) Vakis, A. et al. *Tribol. Int.* **2018**, *125*, 169–199.

(419) Wang, Z. *Adv. Mater.* **2012**, *24*, 280.

(420) Hinchet, R.; Seung, W.; Kim, S.-W. *ChemSusChem* **2015**, *8*, 2327.

(421) Zi, Y.; Wang, Z. *APL Mater.* **2017**, *5*, 074103.

(422) Khan, U.; Hinchet, R.; Ryu, H.; Kim, S.-W. *APL Mater.* **2017**, *5*, 073803.

(423) Wang, Z. *ACS Nano* **2013**, *7*, 9533.

(424) Zi, Y.; Guo, H.; Wen, Z.; Yeh, M.-H.; Hu, C.; Wang, Z. *ACS Nano* **2016**, *10*, 4797.

(425) Wang, Z.; Song, J. *Science* **2006**, *312*, 242.

(426) Wang, Z. *Mater. Today* **2017**, *20*, 74.

(427) Wang, S.; Lin, L.; Xie, Y.; Jing, Q.; Niu, S.; Wang, Z. *Nano Lett.* **2013**, *13*, 2226.

(428) Yang, Y.; Zhang, H.; Chen, J.; Jing, Q.; Zhou, Y.; Wen, X.; Wang, Z. *ACS Nano* **2013**, *7*, 7342.

(429) Xie, Y.; Wang, S.; Niu, S.; Lin, L.; Jing, Q.; Yang, J.; Wu, Z.; Wang, Z. *Adv. Mater.* **2014**, *26*, 6599.

(430) Lee, J.; Ye, B.; Baik, J. *APL Mater.* **2017**, *5*, 073802.

(431) Li, J.; Wang, X. *APL Mater.* **2017**, *5*, 073801.

(432) Fan, F.-R.; Lin, L.; Zhu, G.; Wu, W.; Zhang, R.; Wang, Z. *Nano Lett.* **2012**, *12*, 3109.

(433) Bai, P.; Zhu, G.; Jing, Q.; Yang, J.; Chen, J.; Su, Y.; Ma, J.; Zhang, G.; Wang, Z. *Adv. Funct. Mater.* **2014**, *24*, 5807.

(434) Lin, L.; Wang, S.; Xie, Y.; Jing, Q.; Niu, S.; Hu, Y.; Wang, Z. *Nano Lett.* **2013**, *13*, 2916.

(435) Bao, Y.; Wang, R.; Lu, Y.; Wu, W. *APL Mater.* **2017**, *5*, 074109.

(436) Kim, S.; Gupta, M.; Lee, K.; Sohn, A.; Kim, T.; Shin, K.-S.; Kim, D.; Kim, S.; Lee, K.; Shin, H.-J.; Kim, D.-W.; Kim, S.-W. *Adv. Mater.* **2014**, *26*, 3918.

(437) Liu, J.; Goswami, A.; Jiang, K.; Khan, F.; Kim, S.; McGee, R.; Li, Z.; Hu, Z.; Lee, J.; Thundat, T. *Nature Nanotechnol.* **2018**, *13*, 112.

(438) Diaz, A. F.; Felix-Navarro, R. M. *J. Electrostat.* **2004**, *62*, 277.

(439) The NOMAD Laboratory – A European Centre of Excellence. https://nomad-repository.eu/ [Online; accessed 27-August-2019]".

(440) Pizzi, G.; Cepellotti, A.; Sabatini, R.; Marzari, N.; Kozinsky, B. *Comput. Mater. Sci.* **2016**, *111*, 218–230.

(441) Castle, G. *Journal of Electrostatics* **1997**, *40-41*, 13 – 20.

(442) Cheng, G.-G.; Jiang, S.-Y.; Li, K.; Zhang, Z.-Q.; Wang, Y.; Yuan, N.-Y.; Ding, J.-N.; Zhang, W. *Appl. Surf. Sci.* **2017**, *412*, 350–356.

(443) Kim, D.; Tcho, I.-W.; Jin, I.; Park, S.-J.; Jeon, S.-B.; Kim, W.-G.; Cho, H.-S.; Lee, H.-S.; Jeoung, S.; Choi, Y.-K. *Nano Energy* **2017**, *35*, 379–386.

(444) Nguyen, V.; Yang, R. *Nano Energy* **2013**, *2*, 604–608.

(445) Lu, C.; Han, C.; Gu, G.; Chen, J.; Yang, Z.; Jiang, T.; He, C.; Wang, Z. *Adv. Eng. Mater.* **2017**, *19*, 1700275.

(446) Wen, Z.; Guo, H.; Zi, Y.; Yeh, M.-H.; Wang, X.; Deng, J.; Wang, J.; Li, S.; Hu, C.; Zhu, L.; Wang, Z. L. *ACS Nano* **2016**, *10*, 6526.

(447) Wang, Z. *Faraday Discuss.* **2014**, *176*, 447–458.

(448) Guo, H.; Wen, Z.; Zi, Y.; Yeh, M.-H.; Wang, J.; Zhu, L.; Hu, C.; Wang, Z. *Adv. Energy Mater.* **2015**, *6*, 1501593.

(449) Zhu, G.; Lin, Z.-H.; Jing, Q.; Bai, P.; Pan, C.; Yang, Y.; Zhou, Y.; Wang, Z. *Nano Lett.* **2013**, *13*, 847.

(450) Goswami, A.; Dhandaria, P.; Pal, S.; McGee, R.; Khan, F.; Antić, Ž.; Gaikwad, R.; Prashanthi, K.; Thundat, T. *Nano Res.* **2017**, *10*, 3571.

(451) Park, J.; Salmeron, M. *Chem. Rev.* **2014**, *114*, 677–711.

(452) Nonnenmacher, M.; O'Boyle, M.; Wickramasinghe, H. *Appl. Phys. Lett.* **1991**, *58*, 2921–2923.

(453) Wang, H.; Huang, C.-C.; Polcar, T. *Sci. Rep.* **2019**, *9*, 334.

(454) Drolle, E.; Bennett, W.; Hammond, K.; Lyman, E.; Karttunen, M.; Leonenko, Z. *Soft Matter.* **2017**, *13*, 355–362.

(455) Korir, K.; Cicero, G.; Catellani, A. *Nanotechnology* **2013**, *24*, 475401–475406.

(456) Seol, M.-L.; Han, J.-W.; Moon, D.-I.; Meyyappan, M. *Nano Energy* **2017**, *32*, 408–413.

(457) Cammarata, A.; Polcar, T. *RSC Adv.* **2015**, *5*, 106809.

(458) Cammarata, A.; Polcar, T. *Inorg. Chem.* **2015**, *54*, 5739.

(459) Cammarata, A.; Polcar, T. *Phys. Chem. Chem. Phys.* **2016**, *18*, 4807.

(460) Cammarata, A.; Polcar, T. *Nanoscale* **2017**, *9*, 11488.

(461) Irving, B.; Nicolini, P.; Polcar, T. *Nanoscale* **2017**, *9*, 5597.

(462) Cammarata, A.; Nicolini, P.; Simonovic, K.; Ukraintsev, E.; Polcar, T. *Phys. Rev. B* **2019**, *99*, 094309.

Authors' short bio and photo

Remedios Cortese

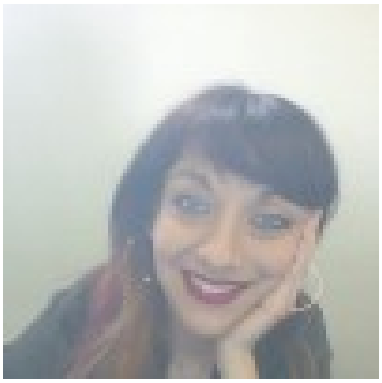

Figure 26: Remedios Cortese

Remedios Cortese collaborates with the University of Palermo and is part of the Group of Computational Chemistry of Palermo. She got degree in Chemistry and a PhD in Chemical Science, both at the University of Palermo. Her scientific research is focused on the modellization, with DFT based methods, of catalyzed reaction mechanisms concerning industrially relevant substrates.

Danilo Puggioni

Danilo Puggioni is an Assistant Research Professor in the Materials Science and Engineering Department at the Northwestern University. He holds a Laurea in Physics and a PhD in Condensed Matter Physics, both from Università di Cagliari, Italy. Danilo joined the Northwestern University after completing postdoctoral work at Drexel University. Danilo uses first-principles theoretical techniques to understand the structural, electronic, magnetic, and optical properties of complex oxides.

Figure 27: Danilo Puggioni

Figure 28: Antonio Cammarata

Antonio Cammarata

After his PhD in Physics obtained at the Università degli Studi di Palermo (Italy), Antonio Cammarata moved to Philadelphia (USA) to work as a post-doctoral researcher at the Drexel University. He then joined the Advanced Materials Group at the Department of Control Engineering of Czech Technical University in Prague (Czech Republic), where he is currently appointed as an Assistant Professor. His research interests include energy production in fuel cells, charge-ordering in Perovskites, hybrid-improper ferroelectricity, nonlinear optically active materials, nanotribology, electron-phonon and phonon-phonon coupling among others.